



Atmospheric pressure Radio Frequency discharges, diagnostic and numerical modeling

Nicolas Balcon

► To cite this version:

Nicolas Balcon. Atmospheric pressure Radio Frequency discharges, diagnostic and numerical modeling. Atomic Physics [physics.atom-ph]. Université Paul Sabatier - Toulouse III; Australian National University, 2007. English. NNT: . tel-00211176

HAL Id: tel-00211176

<https://theses.hal.science/tel-00211176>

Submitted on 21 Jan 2008

HAL is a multi-disciplinary open access archive for the deposit and dissemination of scientific research documents, whether they are published or not. The documents may come from teaching and research institutions in France or abroad, or from public or private research centers.

L'archive ouverte pluridisciplinaire **HAL**, est destinée au dépôt et à la diffusion de documents scientifiques de niveau recherche, publiés ou non, émanant des établissements d'enseignement et de recherche français ou étrangers, des laboratoires publics ou privés.

Atmospheric pressure Radio Frequency discharges, diagnostic and numerical modeling

A thesis submitted for the degree of
Doctor of Philosophy of the Australian National University
and
Docteur de l'Université de Toulouse
délicré par l'Université Toulouse III - Paul Sabatier
by
Nicolas Balcon

defended on the 28th of November 2007
in front of the jury composed of

President :	Jean-Pascal Cambronne	<i>LAPLACE</i> , Toulouse
Examiners :	Françoise Massines	<i>PROMES</i> , Perpignan
	Laiifa Boufendi	<i>GREMI</i> , Orléans
Reviewers :	Rod Boswell	<i>SP₃</i> , Canberra
	Jean-Pierre Boeuf	<i>LAPLACE</i> , Toulouse
	Éric Moreau	<i>LEA</i> , Poitiers
	Antoine Rousseau	<i>LPTP</i> , Palaiseau
	Gerjan Hagelaar	<i>LAPLACE</i> , Toulouse
Invited members:	Leanne Pitchford	<i>LAPLACE</i> , Toulouse
	Ane Aanesland	<i>LPTP</i> , Palaiseau

LABoratoire PLAsma et Conversion d'Energie (*LAPLACE*),
Université Paul Sabatier, Toulouse III,
118 route de Narbonne, Toulouse Cedex 31062, France

Space Plasma Power and Propulsion (*SP₃*),
Research School of Physical Sciences and Engineering,
the Australian National University,
Canberra, ACT, 0200, Australia

This thesis contains no material which has been accepted for the award of any other degree or diploma in any university. To the best of the author's knowledge and belief, it contains no material previously published or written by another person, except where due reference is made in the text.

Nicolas Balcon
November 30, 2007

Acknowledgements

Although there is only one author name on this manuscript, it is a collective work which would not have been possible without a number of people to whom I owe a lot. First of all I would like to thank my two supervisors Rod Boswell and Jean-Pierre Boeuf for believing in me and for giving me the great opportunity to do this PhD. Thank you Rod as much for what you have done as for what you have not. I really enjoyed all the fruitful and memorable conversations we had about plasma, life, the universe and everything. Thank you Jean-Pierre for trusting me, for your precious support that started long before I went to Australia and for your general help in plasma physics.

I want to thank Christine Charles whose dynamism and happiness are so important in the lab. I felt very secure when I saw a Breton flag the first day I arrived at SP_3 . I also want to thank Leanne Pitchford for all her wise advice and for lending me some of her most valuable science books.

I express my gratitude to Jean Pascal Cambronne, Eric Moreau and Antoine Rousseau who kindly accepted to be members of the jury and also to Françoise Massines and Laïfa Boufendi for being my examiners.

Thank you Ane for sharing your experience of radio frequency plasma experiments and for showing me all the very useful lab tricks. Thank you Gerjan for all your explanations concerning numerical modelling and plasma physics. I am also very thankful for the piano lessons you gave me.

Building a new experimental set-up is always extremely time consuming and requires the efforts of many people. Peter and Steve did an amazing job in the workshop and they brought new ideas each time I was confronted with technical issues. Among all my colleagues in Australia, Dave Pretty deserves my thanks for solving happily and rapidly all my computer problems ; Devin for giving me the keys of his very clean and very coveted tool box and for showing me the contact angle room ; Orson for his cross cultural jokes in a perfect franglais when we were lab-mates ; Pete for sharing his deep understanding of the expansive vector network analyser. I thank Ian Falconer, John Pigott and Benjamin Powell for their help with streak cameras and also Cormac, Boris, Weitang and Michael for contributing to the lab's good mood. A general thanks is addressed to Thomas, Youssef, Nicolas, Jaime, Thierry, Laurent, Benoît, Frédéric, Pierre, Kremena and Freddy for their warm welcome in Toulouse.

Thank you Albert for helping me with your experience of cotutelle, for showing me the good places and good people in Canberra, for answering accurately all my Matlab related questions and for having never shared any orange juice with me. Thank you Amaël for being the perfect house-mate and for the memories of morning bike rides in winter. A very special thanks goes to H  l  ne. Without her I could never have started this PhD, her support has always been wonderful.

I also want to mention all the teachers I have learnt from, especially Fran  ois Brunou who will probably never read this. He was my mathematics teacher in pr  pa and he has a great talent in communicating his passion for science. I am very grateful to all my family and especially my parents for their immutable support throughout all my studies.

Finally, thank you Carla for your generosity, your crucial and constant help, your smile and your trust in me.

Abstract

The aim of this thesis is to investigate the properties of a Radio Frequency capacitive discharge at atmospheric pressure in argon. In these conditions where the pressure-distance product is around 150 Torr.cm , the discharge usually consists of several locally hot filaments. By pulsing the RF generator with an appropriate width and period, it was found possible to control the filament to glow transition in order to obtain a diffused and stable plasma.

The 2 mm gap between the electrodes is open to the ambient air and fed with argon via one hundred submillimetric holes regularly spread on the surface of the top electrode. This configuration allows “on-line” surface treatment of polymer films without having to turn the discharge off between successive samples. An important and lasting improvement of the polymer wettability is quickly obtained without risk of damage.

The plasma diagnostic methods are emission spectroscopy and electric measurements. The Stark broadening of the Balmer β transition line of atomic hydrogen is measured to determine a plasma density of 10^{15} cm^{-3} in the filamentary mode. The glow mode density estimation was based on power balance yielding a density of $5 \times 10^{11} \text{ cm}^{-3}$. Emission line ratios between neutrals and Ar^+ ions are used in the Saha equation to calculate the electron temperature. It results in an approximation of 1.3 eV for the glow mode and 1.7 eV for the filaments.

A unidimensional self-consistent fluid model is developed to gain insight into the homogeneous discharge behaviour. Poisson’s equation for the electric field is coupled to the first moments of the Boltzmann equation (continuity equation, drift-diffusion equation and energy equation). Transport and reaction coefficients are obtained from the mean energy of the electrons .

The model is applied to a reduced argon kinetic with the main ionization and excitation processes. Simulation results are in agreement with experimental measurements. The atmospheric pressure RF discharge is similar to a lower pressure RF discharge for which the ionization occurs mainly inside the oscillating sheaths where electrons are the most energetic.

Résumé

Le thème principal de cette thèse est l'étude des propriétés d'une décharge capacitive Radio Fréquence à pression atmosphérique dans l'argon. Dans ces conditions où le produit pression-distance est de l'ordre de 150 Torr.cm , la décharge a tendance à former une multitude de filaments localement chauds. En pulsant le générateur RF avec une période et une durée adéquates, il est possible de contrôler la transition du mode filament au mode homogène afin d'obtenir un plasma diffus et stable.

L'espace inter-électrode de 2 mm est ouvert sur l'air ambiant et alimenté en argon par une centaine d'orifices submillimétriques répartis régulièrement sur l'électrode supérieure. Cette configuration permet d'effectuer un traitement de la surface de films polymères en ligne, sans éteindre la décharge entre les échantillons successifs. Une augmentation importante et durable du caractère hydrophile est rapidement obtenue sans risque d'endommager le polymère.

Le diagnostic du plasma est effectué par spectroscopie d'émission et par mesures électriques. L'élargissement de Stark de la raie d'hydrogène Balmer β permet d'estimer la densité électronique dans les filaments à 10^{15} cm^{-3} . Pour le mode homogène, une approximation basée sur l'équilibre entre la puissance RF transmise et dissipée par le plasma conduit à une densité de $5 \times 10^{11} \text{ cm}^{-3}$. Les rapports d'intensité des lignes spectrales d'argon neutre et d'ion Ar^+ sont introduits dans l'équation de Saha pour calculer la température électronique. Dans le mode homogène la température estimée à 1.3 eV est légèrement plus faible que dans les filaments à 1.7 eV .

Un modèle fluide auto-cohérent unidimensionnel est également développé pour étudier plus précisément le comportement de la décharge dans son mode homogène. L'équation de Poisson pour le champ électrique est couplée aux premiers moments de l'équation de Boltzmann (équation de continuité, équation de dérive-diffusion et équation d'énergie). Les coefficients de transport et de réaction sont obtenus à partir de l'énergie moyenne des électrons.

Le modèle est appliqué à une cinétique chimique réduite de l'argon contenant les principaux processus d'ionisation et d'excitation. Les résultats de simulations sont en bon accord avec les mesures expérimentales. La décharge RF atmosphérique est comparable aux décharges RF classiques basse pression dans lesquelles l'ionisation a majoritairement lieu dans les gaines oscillantes, là où les électrons ont le plus d'énergie.

Contents

Acknowledgements	5
Abstract	7
Résumé	9
Contents	12
1 Introduction	17
1.1 Atmospheric pressure discharges	17
1.1.1 Dielectric Barrier Discharges	18
1.1.2 Radio Frequency excitation	20
1.2 Scope of this thesis	21
2 Experimental configuration	23
2.1 Experimental set-up	23
2.1.1 Discharge configuration	23
2.1.2 Matching network	25
2.1.3 Optical set-up	26
2.1.4 gas composition	30
2.2 Existence of the discharge in two different modes	32
2.2.1 Breakdown	32
2.2.2 Filamentary mode and Glow mode	32
2.2.3 Pulsing the RF power supply	39
2.2.4 Fast imaging	41
2.2.5 Filament \rightleftharpoons glow transition controlled by pulse	44
3 Plasma diagnostic and application to surface treatment	49
3.1 Electric measurements	49
3.2 Electron density	53
3.2.1 Filamentary mode - Stark Broadening	53
3.2.2 Glow mode - Power Balance	55
3.3 Electron temperature	57
3.3.1 Optically thin plasma	57

3.3.2	Boltzmann plot	59
3.3.3	Saha equation	61
3.4	Surface treatment	66
3.4.1	Contact angle measurement	67
3.4.2	Scanning Electron Microscope	67
4	Numerical model	71
4.1	Motivation	71
4.2	Governing equations	72
4.2.1	Moments of Boltzmann's equation	72
4.2.2	Poisson's equation	78
4.2.3	Boundary conditions	78
4.2.4	System of equations	79
4.3	Numerical solutions	80
4.3.1	Solving the continuity equation and the particle flux	80
4.3.2	Solving Poisson's equation	83
4.3.3	Poisson's equation coupled with the continuity equation	85
4.3.4	Solving the electron energy equation	87
4.4	Applied Voltage, external circuit	88
4.4.1	Dielectric layer	89
4.4.2	Serial resistor	90
4.5	Argon kinetics	92
5	Simulation results	95
5.1	RF breakdown	95
5.1.1	Breakdown voltage - Sustain voltage	96
5.1.2	Ion trapping	97
5.2	Particle density	98
5.2.1	Initial density	98
5.2.2	Spatial distribution	99
5.3	Electron temperature	103
5.4	Conduction current and displacement current	104
5.5	Contribution of reactions	108
5.6	Effects of the applied voltage	110
5.6.1	Conclusion	114
6	Conclusion	115
A	Boltzmann equation	119
B	Exponential Scheme	123
	Bibliography	130

List of Figures

1.1	Paschen curve	19
1.2	Memory effect in DBDs	19
1.3	Pattern formation in DBDs	20
2.1	Experimental configuration	24
2.2	Picture of the discharge in the glow mode	24
2.3	Π matching network	26
2.4	DBD set-up for axial optical access	27
2.5	Optical set-up with transparent dielectric: Pyrex + fine copper mesh	28
2.6	Plasma spectrum	29
2.7	The two different plasma modes	33
2.8	Burn marks made by filaments on a sheet of paper	34
2.9	Spectrum in each mode of the plasma	36
2.10	Axial view of the glow mode	37
2.11	Axial view of plasma fingering	38
2.12	Axial view of plasma penetrating the “shower head” holes	38
2.13	Axial view of plasma filaments	39
2.14	Filaments forming a circle	39
2.15	Oscillation in the PMT signal due to the impact of a single photon	40
2.16	Evolution of an ArI line during a pulse	40
2.17	Axial pictures taken every $16 \mu s$ in the filamentary mode	42
2.18	Radial pictures taken every $2 \mu s$ in the filamentary mode	43
2.19	Axial pictures taken every $8 \mu s$ in the glow mode	44
2.20	Pulse width limit of $5 \mu s$	45
2.21	Pulse parameters	46
2.22	Filament \rightleftharpoons Glow transitions	47
3.1	Gas voltage	50
3.2	DBD equivalent circuit	51
3.3	Conduction current in the discharge	52
3.4	Comparison of the luminous regions position	53
3.5	Spectrum with and without the H_β line	55
3.6	Voigt fit of the H_β line	56

3.7	Absorption coefficient	59
3.8	Grotrian diagram	60
3.9	ICP source	61
3.10	Boltzmann plots for the ICP source	62
3.11	Example of $ArI/ArII$ ratio as a function of T_e	64
3.12	Electron temperature evolution	65
3.13	Contact angle measurements	68
3.14	SEM images of polymer samples	69
3.15	Evolution of the wettability	70
4.1	Mesh 1D	81
4.2	Dielectric layer in the external circuit	89
4.3	Resistor in the external circuit	91
5.1	Current and voltage evolution	96
5.2	Potential in the gap after the breakdown	97
5.3	Breakdown for two values of the secondary emission coefficient	98
5.4	Breakdown for different values of the initial densities	99
5.5	Densities averaged over one RF period	100
5.6	Evolution of the electron density	101
5.7	Evolution of molecular ions Ar_2^+ density	101
5.8	Evolution of metastable atoms Ar^* density	102
5.9	Evolution of atomic ions Ar^+ density	102
5.10	Evolution of the electron temperature	103
5.11	Heating and energy loss averaged over one RF period	104
5.12	Heating and energy loss averaged over the gap	105
5.13	Evolution of the current densities averaged over the gap	105
5.14	Distribution of the current averaged over one RF period	106
5.15	Evolution of the current densities averaged over the gap	107
5.16	Charged particle flux averaged over one RF period	107
5.17	Relative contribution to electron creation averaged over one RF period	108
5.18	Total source of electrons	109
5.19	I-V characteristic and electron density	110
5.20	Electron source	112
5.21	Density and potential profiles	112
5.22	I-V characteristic for different value of the secondary emission coefficient	113
5.23	Electron density in the γ mode	114
A.1	Phase space	120

List of Tables

3.1	FWHM for different broadening mechanisms	54
3.2	Spectral data from NIST	63
4.1	Governing equations for the model	80
4.2	Rate coefficients of reactions	93
5.1	Relative contributions of reactions	109

Chapter 1

Introduction

1.1 Atmospheric pressure discharges

In the past few years, atmospheric pressure gas discharges have received an increasing amount of attention both from academic groups and companies. Low pressure plasma reactors are widely utilized for surface treatment of polymers and functionalization of semiconductors. The possibility to use plasma sources at a much higher pressure is of great interest. Despite their tendency to turn into hot filaments and to be more difficult to control than low pressure discharges, atmospheric pressure plasmas present many advantages for industrial applications:

- absence of expensive and power consuming vacuum systems
- absence of pumping down time
- absence of vacuum compatibility issues

These three factors drastically reduce all the operational costs of manufacturers. Some atmospheric pressure reactors are open to the ambient air for “on-line” surface treatment. The plasma is not turned off between each sample making the treatment process even faster and cheaper. This process has been optimized for industrial purposes as reported by [Moon et al. \(2003\)](#).

Of course not only surface treatment time efficiency is improved, there are many applications that benefit from the possibility of stable atmospheric pressure plasmas. For instance depollution, sterilization, medical interventions, and more recently, flow control or combustion control ([Boeuf et al., 2007](#); [Moreau, 2007](#)).

Different geometrical configurations and excitation schemes can be utilized to obtain an atmospheric pressure discharge in various gases. Many studies have been made about Dielectric Barrier Discharges (DBD), corona discharges, plasma Jets, arcs in circuit breakers and micro discharge. In the DBD configuration, homogeneous glow mode have already been observed. This phenomenon has been classified as the “one atmosphere uniform glow discharge plasma”, OAUGDP ([Roth et al., 2005](#); [Massines et al., 1998](#)).

In the present work the DBD set-up is studied. It is a capacitively coupled discharge where the voltage is applied between two circular electrodes separated by a small gap. To limit the current and avoid the transition to arc, a dielectric layer is added on one or both electrodes.

The DBD arrangement is well adapted for the majority of surface treatment applications. Historically DBD were first applied in air in order to generate ozone (Kogelschatz, 2003) but today they are often used for the production of UV radiations for lamps (Mildren and Carman, 2001) or plasma display panels (Boeuf, 2003).

For capacitively coupled plasma, the breakdown voltage for a given gas and an electrode material is a function of the $p \cdot d$ (pressure-distance) (Raizer, 2001).

Paschen curve

The breakdown voltage is the minimum voltage that sustains the discharge and it corresponds to its ignition potential. When this potential is reached, the creation of secondary electrons at the cathode (every ion hitting the anode releases γ electrons) replaces the electron that ignited the avalanche. In these conditions the following relation is satisfied:

$$\gamma \left(e^{\alpha d} - 1 \right) \geq 1$$

Where α is the Townsend coefficient and γ is the secondary emission coefficient. This breakdown mechanism known as “Townsend breakdown” takes place when the $p \cdot d$ product is sufficiently small (typically less than a few 100 *Torr.cm*). For higher $p \cdot d$ products, streamer breakdown can occur. As shown on figure 1.1 from Schütze 1998, in argon the voltage needed to sustain the discharge for a gap of 2 *mm* ($p.d = 150$ *Torr.cm*) between metallic electrodes is approximately 1.5 *KV*.

In this condition of high electric field the radius of an electron avalanche is generally much smaller than the electrode radius, thus the discharge is made of several filaments and without the dielectric layer an arc would be created. In classic lower pressure homogeneous CCP the radius of an electron avalanche is of the same order as the reactor size and this problem does not appear. Hence low pressure (around 1 *mT*) CCP discharges can run with bare electrodes.

1.1.1 Dielectric Barrier Discharges

As dielectric is an insulator, DBDs can only run with an alternative or pulsed voltage. They often run in the kHz range with a typical gap of 2 *mm* between the electrodes. After the breakdown of the gas, the dielectric surface is charged and the field across the electrodes is reduced. The discharge is stopped before its thermalization. However this does not prevent the formation of filaments which are not as destructive as arcs but can still create damage in surface treatment applications.

Memory effect in Dielectric barrier Discharge

The lifetime of charges on dielectric surface in dry air at atmospheric pressure is much longer than the repetition period of the RF power supply or the pulse generator. There-

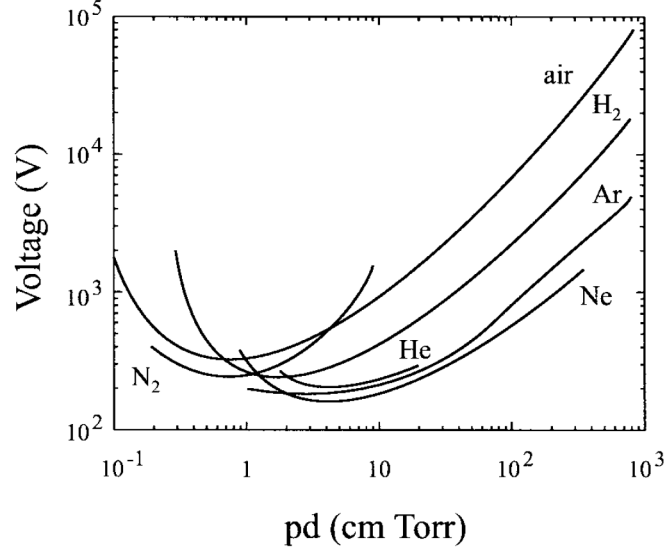


Figure 1.1: Paschen Curve from [Schütze 1998](#)

fore, the charges deposited on the surface of the dielectric remain on it between two cycles.

This phenomenon known as the memory effect for DBD affects the electric field and is responsible of the stationary behaviour of filaments in DBDs ([Chirokov, 2005](#); [Fridman, 2005](#)). When a filament reaches the dielectric, the axial electric field is reduced where the filament touched the insulated electrode and a radial electric field is created between the filaments and the filament-free regions.

When the polarity is reversed the electric field is greater and the breakdown is easier at this exact position as shown on figure 1.2.

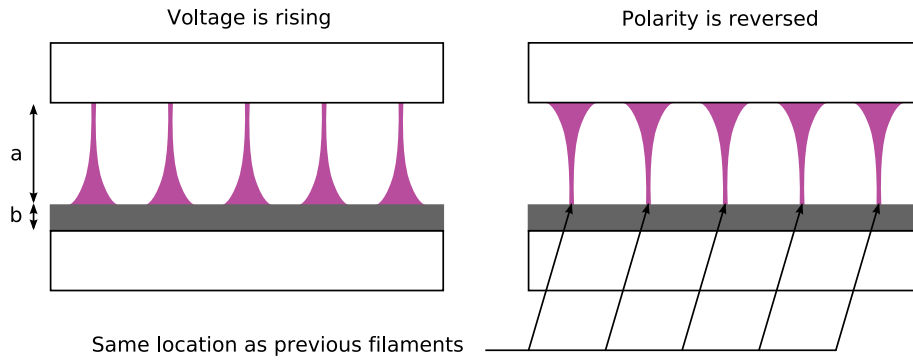


Figure 1.2: Memory effect in DBDs

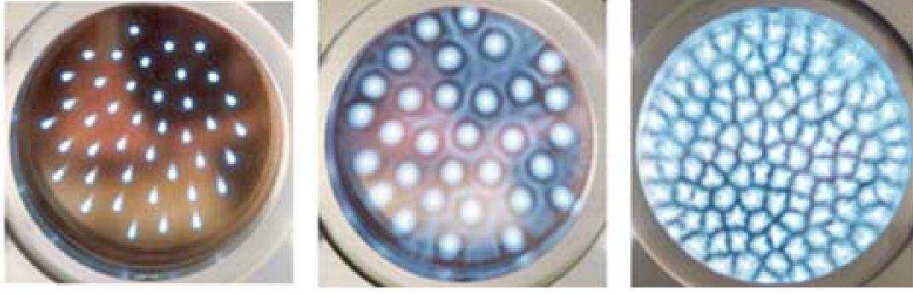


Figure 1.3: Pattern formation in DBD from [Kogelschatz 2000](#)

Hence, the discharge tends to stay stationary in the filament mode. These filaments often form interesting patterns as illustrated on figure 1.3 which are widely analysed as reported by [Muller \(1999\)](#).

1.1.2 Radio Frequency excitation

Most atmospheric pressure DBDs are excited at 10 kHz . In the present experiment the plasma is excited at 13.56 MHz . Atmospheric pressure RF discharges with and without dielectric layer have already been studied by experimental groups ([Park et al., 2000](#); [Moon et al., 2003](#); [Moravej, 2006](#)) and in simulations at low pressure by [Boeuf \(1987\)](#), and high pressure by [Oda et al. \(2005\)](#).

They show properties comparable with lower pressure RF discharges. Unlike 10 kHz DBD, the use of frequencies higher than 10 MHz requires a matching network to couple the power to the capacitive discharge. It is also more complicated to perform current measurement with serial resistors that disturb the impedance matching.

However, the use of RF is still interesting. 13.56 MHz generators are very common and their cost is reasonable. 13.56 MHz is a frequency allotted by international communications authorities at which it is possible to radiate energy without interfering with communication systems.

Also the RF breakdown voltage is lower in the MHz region as reported by [Kunhardt \(2000\)](#) and [Smith et al. \(2003\)](#). In a typical 10 kHz CCP discharge at atmospheric pressure the gas breakdown occurs at every cycle of the applied voltage. Short current peaks of (around 10 ns) have been observed by [Massines et al. \(2005\)](#) and the plasma charge density rapidly falls between each of them.

In the atmospheric pressure RF capacitive discharge the breakdown voltage is reached only once and then a sustain voltage which is two times lower keeps the plasma running. The mobility of the ions is too small to follow the variations of the 13.56 MHz electric field so they are trapped in the gap and the ionization mechanisms are different from 10 kHz DBDs. The numerical modelling results show that a breakdown is possible without secondary emission which would not be possible for a DBD running at 10 kHz .

1.2 Scope of this thesis

The aim of this thesis is to study the properties of a novel kind of atmospheric pressure plasma reactor for fast “on-line” surface treatment based on a pulsed RF discharge at 13.56 MHz . The use of pulsed RF voltage is still not very common at such high pressure.

In this work, the versatility of this reactor is demonstrated. Experimental results show that it is possible to operate an homogeneous RF atmospheric pressure discharge with argon going through a “shower head” electrode in open air.

The plasma mode can be selected and controlled by pulse in order to optimize surface treatment of polymers. Further understanding of the discharge mechanism is gained from a self-consistent fluid model.

The experimental set-up was built and studied at the Space Plasma Power and Propulsion (SP_3) laboratories of the Australian National University in Canberra. Plasma diagnostic and surface treatments were done over one and a half year under the supervision of Rod Boswell, Christine Charles and Ane Aanesland.

The 1D fluid model was written at Laboratoire PLAsma et Conversion d’Energie (*LAPLACE*) of the Université Paul Sabatier in Toulouse during the second half of the thesis. The simulation work was supervised by Jean-Pierre Boeuf, Leanne Pitchford and Gerjan Hagelaar.

This thesis is divided into 5 chapters. Chapter 2 describes the experimental apparatus and the different regimes under which the plasma can exist. The methods of plasma diagnostics are explained and the results are analysed in chapter 3. In chapter 4 the model that describes the discharge is presented. The approximations made to obtain the system of equations and the numerical solving are also explained.

The simulation results are discussed and compared with plasma measurements in chapter 5.

Chapter 2

Experimental configuration

2.1 Experimental set-up

2.1.1 Discharge configuration

The experimental set-up shown on figure 2.1 aims to test a new method for improving high pressure surface treatment versatility without risk of damage to the polymer specimens. It consists of two disk parallel electrodes of 10 *cm* in diameter (78.5 cm^2), the distance between them being adjustable up to 4 *mm*.

The top electrode is grounded and feeds the gap with argon via a “shower head” having an array of one hundred holes, each 0.5 *mm* in diameter. The discharge gap is not enclosed in any vessel so it is not isolated from the room’s air. This configuration choice of not controlled atmosphere is made to optimize surface treatment time efficiency. It is possible to add or remove a sample from the discharge without having to turn it off or access any closed vessel. This makes fast “on-line” surface treatment possible.

The argon flux is equally distributed over all the surface of the top electrode so that the gas flux is centrifugal and the interaction with ambient air is limited as explained in section 2.1.4.

It is also possible to add water vapour to the discharge via a bubbler filled with water. This is used to calculate the electron density by measuring the Stark broadening of the Balmer β transition line of the hydrogen atom (see section 3.2.1).

As high frequencies are used, an impedance matching is required to transfer the power into the plasma. The RF power supply *ENI 600W-13.56 MHz* couples the power to the bottom electrode via the Π -matching network described in section 2.1.2 and the voltage applied to this electrode is measured with a Tektronix Passive High voltage probe (*P6015A ratio 1:1000*) and (*HP Mega Zoom 1 M Ω*) oscilloscope.

On the top of the bottom electrode lies a 4 *mm* thick alumina dielectric layer. This ceramic material Al_2O_3 can resist temperature up to 400°C. A picture of the electrodes arrangement with a glow mode plasma is shown on figure 2.2.

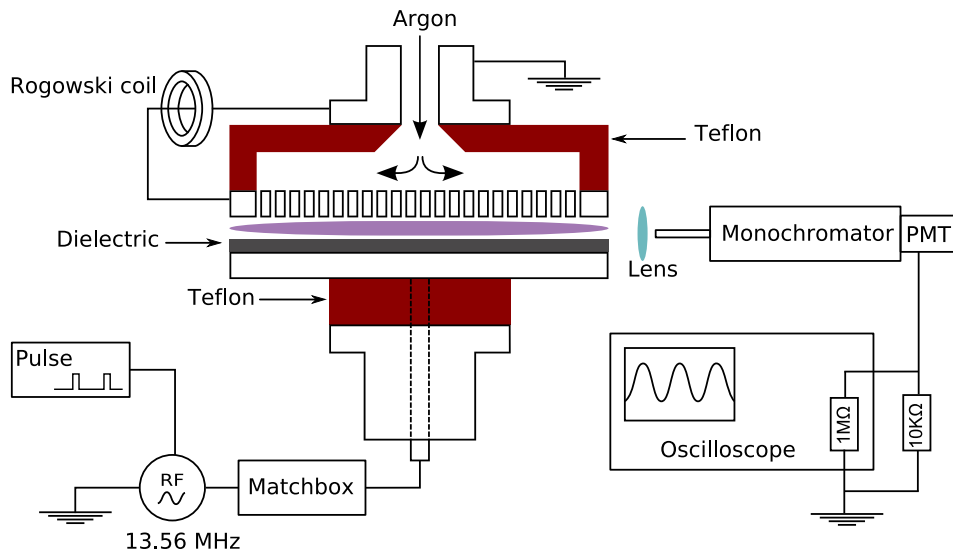


Figure 2.1: Experimental configuration

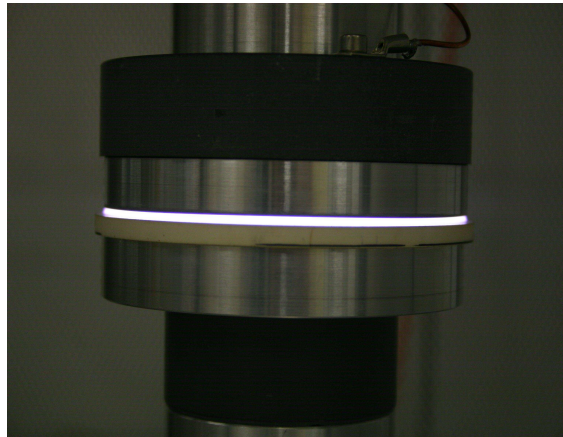


Figure 2.2: Picture of the discharge in the glow mode

In order to have an optical access in the axis of the discharge, transparent dielectric materials and transparent conductors have also been tested. Indium tin oxide commercially available (ITO of approximately $200 \Omega/m$) is deposited on glass up to 2 mm in thickness which was not resistant enough when filaments appear. The used of Pyrex combined with a copper fine mesh was necessary as sketched on figure 2.4.

Under certain conditions a filament-free discharge can be obtained without the dielectric layer. However, without the dielectric barrier this mode is unstable and does not cover the whole electrode area. Without dielectric, the discharge turns into a single intense filament most of the time. The use of the dielectric allows the plasma homogeneity to be dramatically improved.

The RF power supply is controlled by a pulse generator (*PM 5715 1Hz-50MHz Philips*) which sets the RF power ON for a minimum time of 40 RF cycles ($\simeq 5 \mu s$)¹. Pulsed DBDs have already been used to make atmospheric pressure discharges more homogeneous as reported by Carman et al. (2005) and Mildren and Carman (2001). Pulsing the discharges also prevents the dielectric and the polymer samples from reaching high temperatures.

2.1.2 Matching network

In order to avoid reflected power the total load on the generator should be equal to the 50Ω output impedance of the RF generator. The total impedance of the DBD depends on the gap size, the dielectric layer thickness and its permittivity and whether the plasma is ON or OFF. The alumina disk of this experiment has a dielectric relative permittivity of 7 and its thickness is 4 mm . The Pyrex as a dielectric relative permittivity of 4 and is 3 mm thick. The electrodes are 10 cm diameter (surface area $A \simeq 78.5 \text{ cm}^2$). The DBD total impedance when the plasma is off with all the electrode set-up varies from 100 pF to 200 pF depending on the gap size and on the chosen dielectric. Therefore, it is not possible to plug the electrodes directly to the 13.56 MHz power supply, a matching network is required.

The impedance matching is achieved with passive components in a Π network configuration as shown on figure 2.3. Two high voltage tunable vacuum capacitors are added in parallel to the DBD and a serial inductor is added between the capacitors. This creates a resonant circuit with a 17 dB gain as described by Bowick (1997, Chapter 4: Impedance Matching).

$$\left[\frac{V_2}{V_1} \right]_{dB} = 10 \log \left(\frac{V_2}{V_1} \right)^2$$

which yields $V_2 = 7 V_1$. Where V_1 is the voltage at the output of the capacitor and V_2 is the voltage across the DBD gap. The breakdown voltage of 1.4 KV is reached with only 200 V out of the RF generator.

Such a matching set-up prevents the use of a serial resistor to the ground which is often utilized in 10 kHz DBDs to measure the discharge current via Ohm's law. These components are not sufficient to achieve a 50Ω load impedance ; the natural resistive

¹ This minimum is due to the time response of matchbox.

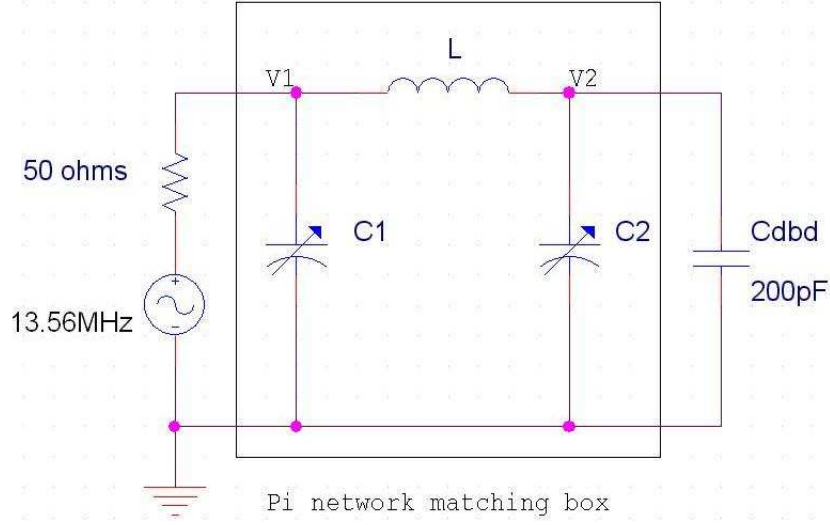


Figure 2.3: Π matching network

part of the total circuit impedance is necessary. A vector network analyser *Rohde and Schwarz ZVRE (3GHz)* helps tuning the matchbox once the set-up is complete. A Rogowski coil (*Clamp-on Current Probe, 9323-1 20Hz-300MHz*) collects the discharge current that goes to the ground.

Once the breakdown has occurred, the total impedance of the DBD is no longer purely capacitive because of the presence of the plasma. The matchbox has to be tuned again. This constant matching necessity can be challenging in the case of a pulsed plasma where the discharge is constantly turned ON and OFF. It is impossible to tune the matchbox at the pulse frequency so a compromise had to be found between the pre-breakdown matching and the post-breakdown matching.

2.1.3 Optical set-up

The common method for plasma diagnostics of electron density and temperature at low pressure is the Langmuir probe. At atmospheric pressure, such a system is not practical. The gap where the discharge occurs is far too small to introduce any probe. In addition probes are not adapted to the measurements of hot localized filaments.

As an alternative, optical emission from the plasma is collected with a converging lens focussing on an optical fibre and detected by a monochromator and photomultiplier tube (SPEX-500M, Hamamatsu PMT R777). This method is non disruptive and well adapted to the analysis of fast phenomena of the breakdown.

The optical measurements are made in the radial axis when the set-up is in the configuration of figure 2.1 and in the symmetrical axis when the set-up is in the configuration of figure 2.4. A picture of the experiment is represented on figure 2.5.

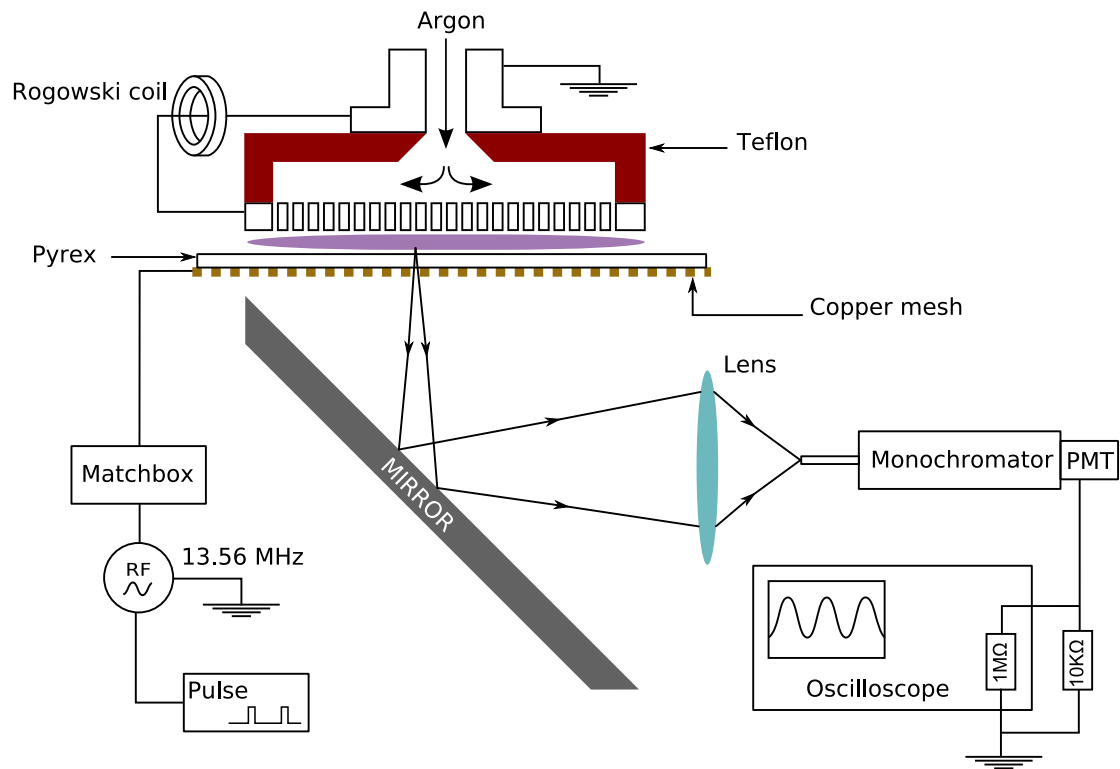


Figure 2.4: DBD set-up for axial optical access



Figure 2.5: Optical set-up with transparent dielectric: Pyrex + fine copper mesh

In the axial view configuration with the transparent electrode, more light is collected (even if the use of a mirror is necessary) and radial resolution is possible. Another advantage of this configuration is the smaller effect of the radiation trapping. The plasma is thinner in this axis. This will be discussed in section 3.3.

Monochromator-Photomultiplier

The light emission from the discharge is acquired with a *Jobin Yvon SPEX 500 M* monochromator. The opening of the input and the output slits is tunable with micrometric screws. The Hamamatsu Photomultiplier Tube (PMT) is composed of 10 dynodes and powered by a 1 kV DC generator. Its output is connected to the oscilloscope via a short BNC cable in order to have the best time response.

The PMT gives a constant output current which is proportional to the light intensity received at a certain wavelength. The internal impedance of the oscilloscope is 1 M Ω which yields the large RC rise time of a low pass filter. This is not adapted to short pulse measurements. With a 10 k Ω resistor added in parallel to the input channel of the oscilloscope a much better rise time of 1 μ s is obtained. A lower parallel resistor would result in a shorter rise time but the PMT signal would be too small to be detected.

The oscilloscope signal is recorded in a computer via a GPIB interface module controlled by a Labview program. For the acquisition of the plasma spectrum, the program is constantly recording the PMT signal as the monochromator is sweeping the wave-

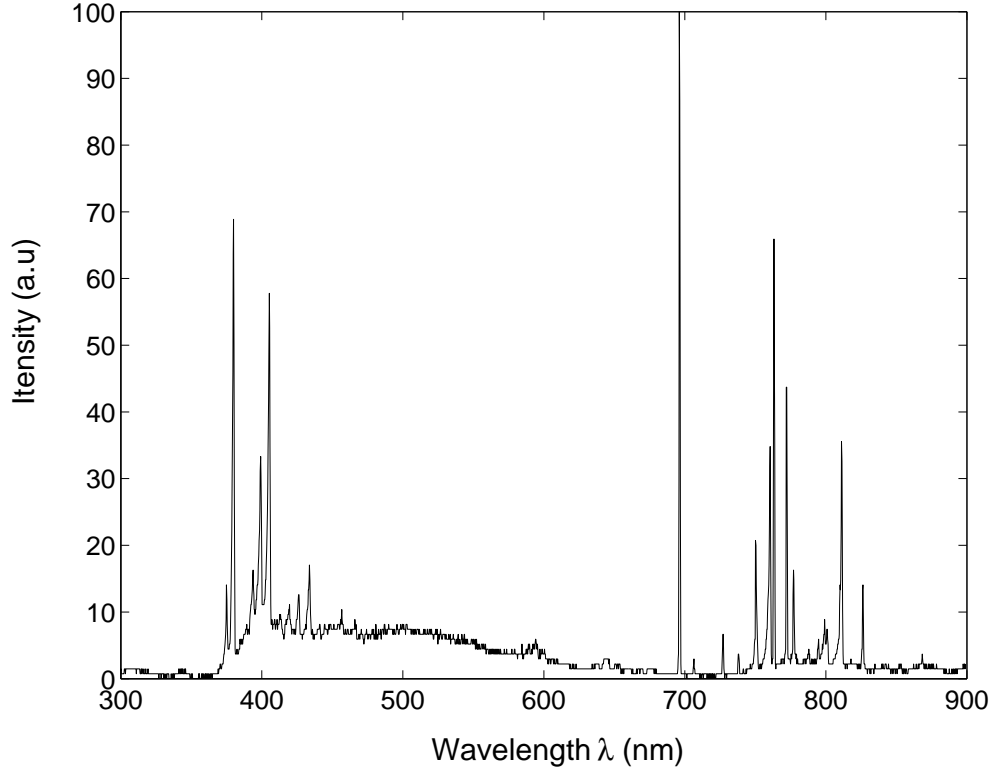


Figure 2.6: Plasma spectrum

lengths from 300 *nm* to 900 *nm* which takes approximately 15 minutes for a reasonable resolution. The spectrum of figure 2.6 shows many argon lines. *ArII* lines are detected between 300 and 650 *nm*, *ArI* lines are detected between 650 and 900 *nm*.

For the spectral measurements of section 3.3, the variation of light intensity is measured for 5 lines:

- *ArI*: 696.55431 *nm*, 750.3869 *nm*, 772.3761 *nm*
- *ArII*: 413.1724 *nm*, 427.7528 *nm*

Optical resolution

In order to maximize the monochromator resolution, an optimum should be found in the opening of the two slits. The input of the monochromator and input of the PMT are set to 60 μm . With a narrower opening, the signal from an atomic line would not be intense enough to be detected and with a wider opening the resulting spectral output would be the sum of several atomic lines.

A calibration test is performed on a mercury lamp line in order to evaluate the instrumental broadening. The FWHM of the broadening due to the total optical set-up is 0.2 nm . This value will be used for the deconvolution of the hydrogen Balmer β atomic line in section 3.2.1

2.1.4 gas composition

DBDs in air give very unsatisfying results for surface treatment purposes. Without argon, no plasma could be obtained even setting the voltage on its maximum of 2.5 kV . Argon is affordable, inoffensive to breath in reasonable quantities and its low ionization level makes the breakdown voltage relatively low.

The gap is fed with argon via a “shower head” so the gas escapes radially at the edges of the discharge. The more intense lines of the plasma spectrum (figure 2.6) are due to argon, however, some air might penetrate the discharge.

It is possible to evaluate the amount of air that mixes with argon: The perimeter of the discharge is 31.4 cm , so when the distance between the electrodes is at its maximum of 4 mm the total surface of the edge of the plasma is 12.56 cm^2 . The argon flow value is adjustable up to 1 standard L/min with a needle valve (*Swagelok low pressure M series*). Most often it is used at its maximum. In these conditions the outgoing velocity at the discharge edge is

$$v = \frac{1000 \text{ cm}^3}{12.56 \text{ cm}^2} \frac{1}{60 \text{ sec}} \simeq 1.3 \text{ cm.s}^{-1}$$

This value seems relatively small to prevent external air to soak in. In order to estimate the relative amount of air going through the discharge gap, the following simplified Navier-Stokes equation is considered for the stationary regime. The argon flux is imposed so the viscous force is neglected. The gas does not reach a speed that significantly disturbs the total pressure.

$$\mathbf{F}_d = \nabla p \quad (2.1)$$

Let n_2 be the air density

n_1 the argon density

n_0 the total gas density which is constant.

$n = n_2/n_0$ to simplify the writing. P is the relative pressure of air and F_d is the drag force of the argon on the air which is directly related to the argon flux:

$$\mathbf{F}_d = nQ \mathbf{\Gamma}_1 \quad (2.2)$$

with

$$Q = \frac{m_1 m_2}{m_1 + m_2} (\nu_{12} \sigma_{12})$$

where $\frac{m_1 m_2}{m_1 + m_2}$ is the reduced mass, ν_{12} is the collision frequency and σ_{12} is the cross section of the collision. Q is deduced from the diffusion coefficient of argon in air.

Equations 2.2 and 2.1 lead to

$$nQ\mathbf{\Gamma}_1 = kT \nabla n \quad (2.3)$$

For symmetry reasons, in cylindrical coordinates only the derivative along the radial axis is taken into account in the expression ∇n . Then $\frac{\partial}{\partial r}n$ is replaced by $n \frac{\partial}{\partial r}\ln(n)$. So equation 2.3 becomes:

$$nQ\mathbf{\Gamma}_1 = kT n \frac{\partial}{\partial r}\ln(n)$$

$$\frac{Q}{kT}\mathbf{\Gamma}_1 = \frac{\partial}{\partial r}\ln(n) \quad (2.4)$$

In the stationary case the argon flux only depends on the source S that is imposed:

$$\nabla \cdot \mathbf{\Gamma}_1 = S$$

Then equation 2.4 can be written as follows

$$\frac{Q}{kT} \nabla \cdot \mathbf{\Gamma}_1 = \nabla \cdot \left(\frac{\partial}{\partial r}\ln(n) \mathbf{i}_r \right)$$

$$\frac{QS}{kT} = \frac{1}{r} \frac{\partial}{\partial r} \left(r \frac{\partial}{\partial r}\ln(n) \right) \quad (2.5)$$

Equation 2.5 can be solved by successive integrations with A and B being two constants accounting for the boundary conditions:

$$A + \frac{QSr^2}{2kT} = r \frac{\partial}{\partial r}\ln(n)$$

$$\frac{A}{r} + \frac{QSr}{2kT} = \frac{\partial}{\partial r}\ln(n)$$

$$A \ln\left(\frac{r}{R}\right) + \frac{QSr^2}{4kT} + B = \ln(n) \quad (2.6)$$

As the air concentration in the middle of the electrode can not diverge $A = 0$ and from the boundary condition $n_2 = n_0$ at the edge of the gap $B = -\frac{QS}{4kT}R^2$. So equation 2.6 becomes:

$$\frac{n_2(r)}{n_0} = \exp \left[\frac{QS}{4kT}(r^2 - R^2) \right] \quad (2.7)$$

The source term expression is

$$S = \frac{d}{\pi R^2 a}$$

where d is the debit (1 L/min corresponds to $\sim 10^{20}/s$), R the electrodes radius and a the gap size ($\pi R^2 a$ is the surface area of the plasma edge). Equation 2.7 can now be written

$$\frac{n_2(r)}{n_0} = \exp \left[\frac{Qd}{4\pi R^2 a kT}(r^2 - R^2) \right]$$

Q is deduced from the diffusion coefficient D of air in argon given in Grigoriev et al. 1997 $0.165 \text{ cm}^2/\text{s}$.

$$Q = \frac{kT}{Dn_0}$$

$$\left. \frac{n_2}{n_0} \right|_{r=0} = \exp \left[-\frac{Qd}{4\pi akT} \right]$$

$$\left. \frac{n_2}{n_0} \right|_{r=0} = \exp \left[-\frac{d}{4\pi an_0 D} \right] \simeq 5 \times 10^{-5}$$

Therefore the relative amount of air in the middle of the discharge is negligible. The external factors which have the largest influence on the plasma properties are the room pressure, temperature ($\sim 25^\circ\text{C}$) and humidity but not the composition of the surrounding air.

2.2 Existence of the discharge in two different modes

2.2.1 Breakdown

When the RF breakdown voltage is reached, the discharge occurs in the gas gap. The presence of the plasma changes the impedance of the gap mainly because a conduction current passes through the gas which is now partially conductor. A new impedance matching is required and the minimum voltage to keep the discharge running is much lower.

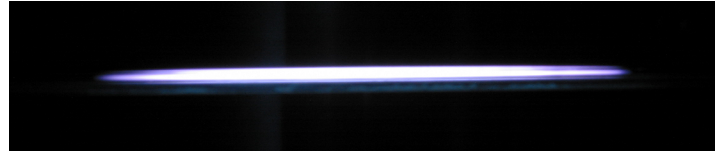
After excited atoms appear in the discharge, as seen on the spectrum of figure 2.6, the stepwise ionization process is possible. Metastable atoms are easier to ionize than the initial gas neutral atoms. Hence electrons of a lower energy can create ions by collisions with excited species and the sustain of the discharge requires a lower voltage

Another reason for this phenomenon is the modification of the electric field distribution. When the space charges are dense enough to affect the electric field in the gap, most of the potential drop is no longer across a (the whole gas gap length) but across a' (the sheath length). With $a > a'$ the ionization takes place within a smaller distance. However, the field across the sheath is much stronger and the ionization due to the ionization coefficient α' in the sheath is more efficient. In other words: $\alpha'a' > \alpha a$. For a 2 mm gap, the breakdown voltage is around 1.4 kV, and the minimum voltage that sustains the plasma is 600 V.

The discharge usually starts with a filamentary mode unless the RF voltage is correctly pulsed.

2.2.2 Filamentary mode and Glow mode

Unlike low pressure plasmas, most of atmospheric pressure discharges in a parallel plate configuration are not homogeneously spread over the whole electrode area. They are



(a) Glow mode



(b) Filamentary mode

Figure 2.7: The two different plasma modes

often composed of many filaments of strong light intensity. The two different modes are represented on figure 2.7 (the light spreading horizontally on the filament picture 2.7 (b) is due to the reflection on the surface of the electrodes).

When the voltage is reduced, the filaments are less numerous and their intensity is weaker. In the continuous RF regime, under certain conditions of gas flow, gap size, ambient room conditions, dielectric temperature and electrode temperature a glow mode was observed. Unfortunately this was not found reproducible even when the voltage is reduced to the minimum value for the plasma sustain. All the external parameters which are not controllable have too much influence on the discharge mode.

The filaments tend to arrange themselves in complex patterns in which they seem to repeal each other. When a sheet of paper with a triangular hole is inserted into the filamentary discharge, the plasma does not covers the paper. It only occurs where the dielectric is bare and it consists of a particular filaments arrangement delimited by the triangle. The filaments burn the edges and the summits of the triangle as shown on figure 2.8. The spacing between the burn marks is regular.

When the discharge is in the filamentary mode, it is irreversible unless we apply a pulse to the RF power supply. The stability of the filamentary mode and their tendency to remain at the same spot makes the continuous RF discharge inappropriate for surface treatment.

It should be emphasized that the filamentary mode witnessed in this discharge is not composed of streamers. In a streamer, the initial electron avalanche reaches a sufficiently important size to create a plasma before the polarity is reversed and before it reaches the anode. The condition for a streamer formation is given in [Fridman and Kennedy 2004](#), Chapter 4.4.7 Criterion of Streamer Formation: Meek breakdown condition – page 219. The electron multiplication in the gap αa has to be greater than 20 so the electric

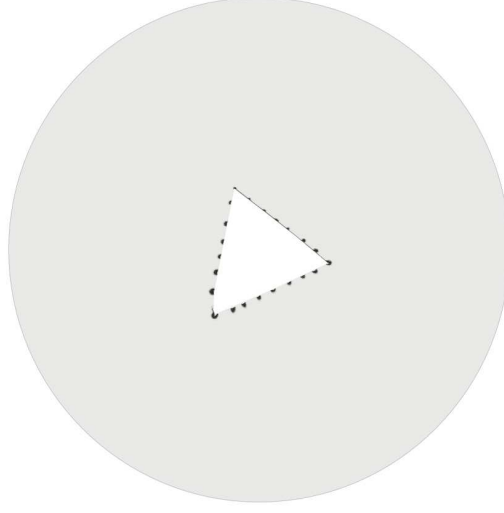


Figure 2.8: Burn marks made by filaments on a sheet of paper

field created at the front of the electronic avalanche by the space charges is strong enough to create the plasma (amplification parameter of $e^{\alpha a}$). With a breakdown field of approximately $7 \times 10^5 \text{ V/m}$, the ionization coefficient α is approximately 1000 m^{-1} . The electronic multiplication is around 2 for a 2 mm gap so this experiment is far from streamer conditions.

Let us consider an electron avalanche in the parallel plate configuration. The repulsion between electrons is negligible for multiplications under 20 (which corresponds to streamers) and the electric field does not force the electrons to move radially. Hence the avalanche radial extension is due only to the diffusion. r is the radial size of an electron avalanche that would start from the cathode and finish at the anode. The electron diffusion coefficient D_e present in the continuity equation:

$$\mathbf{\Gamma}_e = -D_e \nabla n_e + \mu_e n_e \mathbf{E}$$

gives the avalanche radius r according to the following equation:

$$\frac{\partial \langle r^2 \rangle}{\partial t} = 4D_e$$

So the radius value after the time t (time taken by the avalanche to cross the whole gap of length a) is:

$$r = \sqrt{4D_e t} \quad (2.8)$$

Knowing that the drift velocity of the electrons in the direction of the electric field is given by

$$\mathbf{v}_e = \mu_e \mathbf{E}$$

and that $t = \frac{a}{\mu_e E}$. Equation 2.8 becomes:

$$r = \sqrt{4 \frac{D_e}{\mu_e} \frac{a}{E}}$$

The Einstein relation gives the ratio:

$$\frac{D_e}{\mu_e} = T_e$$

In our conditions $1.5 \leq T_e \leq 1.8 \text{ eV}$ (from Park 2001 and from experimental measurement described in section 3.3), $a = 2 \text{ mm}$ and $E = 7 \times 10^5 \text{ V/m}$ so the diffusion radius is $r \simeq 0.14 \text{ mm}$.

This is the approximation of the maximum radius an electron avalanche can reach in the discharge. It is very narrow compared to the radius of the electrodes (5 cm) and thus it is unlikely that electron avalanches would overlap each other.

The discharge is usually composed of around one hundred filaments. However, under certain atmospheric conditions or by pulsing the plasma, it was found possible to obtain a stable glow discharge even without dielectric layer. This is discussed in section 2.2.5.

Plasma spectrum in different mode

To investigate the differences between each plasma regime the spectra from 300 nm to 900 nm are measured. The glow mode and the filamentary mode have the same spectral atomic lines as seen on figure 2.9.

Increasing the power dissipated in the DBD favours the filamentary mode. The spectrum for the filamentary mode is obtained with more power (200 W) than the spectrum for the glow mode (50 W). The light intensity of the glow discharge is lower than the light from the filamentary discharge hence the ordinate scales are different. This explain the apparent difference between the two spectra. The same atomic lines were observed but with different intensity ratios leading to different electron temperatures as explained in section 3.3.

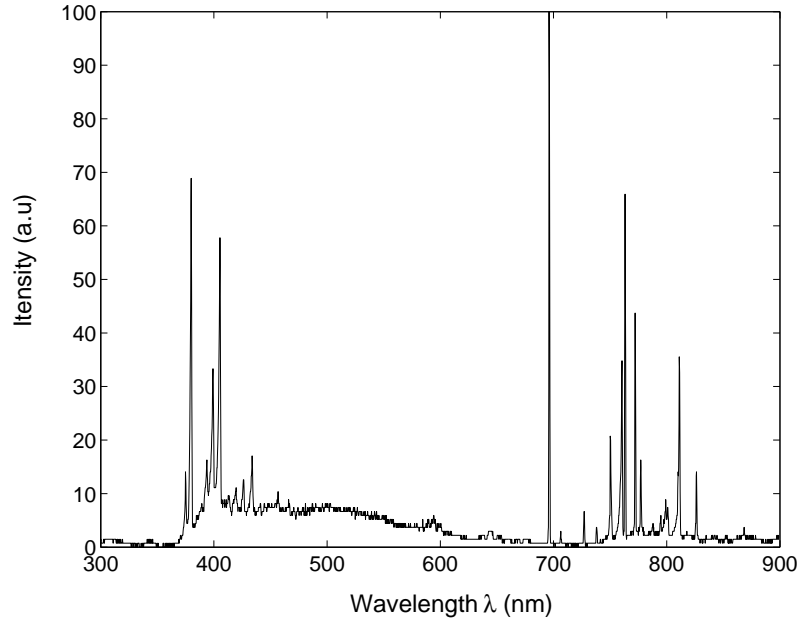
In the filaments the electrons are more energetic than in the glow mode² so one can expect to observe excited species of higher energy in the filament spectrum. This was not visible in the spectrum presented here. The only difference is the relative intensity of each line. This suggests that the glow mode and the filamentary mode are mostly composed of the same excited species. Nonetheless their density, their temperature and their creation mechanisms are different.

Axial view

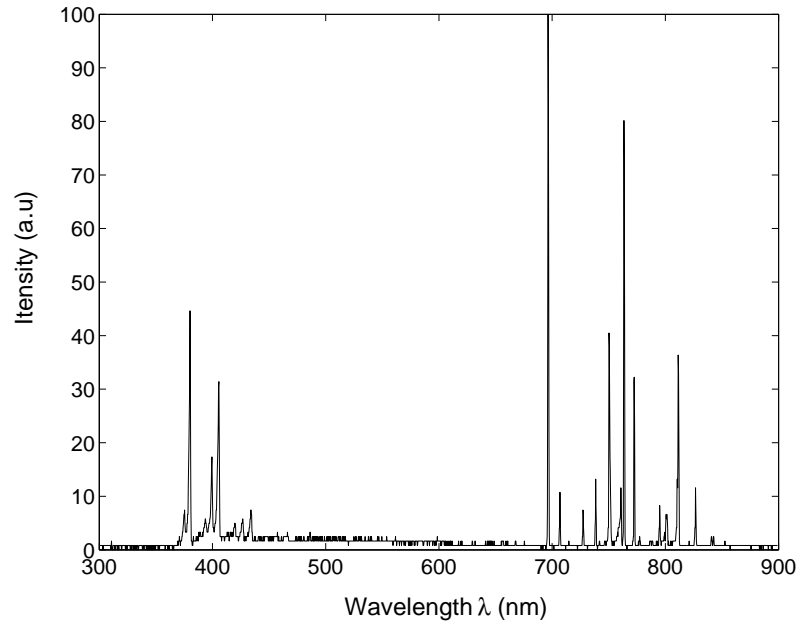
Glow mode

When observed from the side of the electrodes, the glow mode appears completely homogeneous and spread over the whole electrode area. Pictures taken in the configuration

² With the same RF power the discharge is spread over a much smaller area than in the glow mode.



(a) Glow discharge spectrum



(b) Filamentary discharge spectrum

Figure 2.9: Spectrum in each mode of the plasma

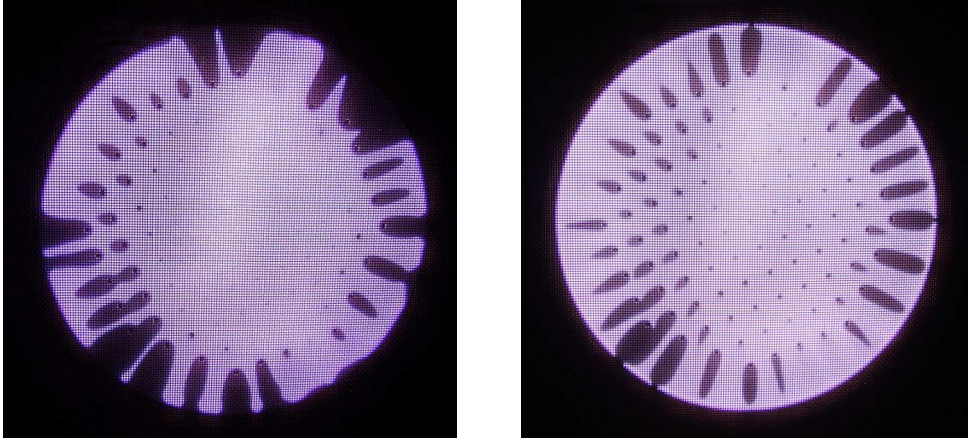


Figure 2.10: Axial view of the glow mode

of figure 2.4 in the direction perpendicular to the electrodes prove that some regions of the glow discharges do not emit any visible light as illustrated in figure 2.10.

Two reasons may account for this phenomenon:

- Exactly under each hole of the argon “shower head” there is a region where the gas does not emit any visible light. The electric field directly in front of the holes (on the grounded electrode) is slightly weaker. Therefore the ionization might not be sufficient to sustain the discharge at this place.
- It is also noticeable that the dark regions are getting wider as the holes are closer to the edge of the electrodes. Their frontier outline is following the centrifugal argon flow (tear drop shape) out of holes in the radial direction outwards. When the argon flux is reduced the dark regions get smaller even if the total brightness of the plasma is reduced (due to the smaller argon debit). This suggests that the discharge does not spread to the regions where too many neutral atoms are injected.

How the dark regions shape and surface areas react to a variation in the gap size is not clear. For a constant argon flow a reduction of the gap size results in an increase of the gas speed. This should blow away more excited species and enlarge the dark regions but at the same time the electric field is increased making the breakdown easier (as predicted by the Paschen curve).

The dark regions are not steady, their sizes and shapes are constantly changing especially when the argon flow is low. This fingering phenomenon is illustrated on figure 2.11. A wide range of pattern geometries have been classified by [Samuell \(2006\)](#).

By increasing the voltage while keeping a glow mode, the dark regions are avoided as shown on figure 2.12. The voltage can even be increased until the plasma penetrates the “shower head” holes. The Debye length must be of the order of a third

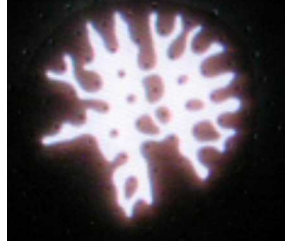


Figure 2.11: Axial view of plasma fingering



Figure 2.12: Axial view of plasma penetrating the “shower head” holes

of the hole diameter (0.15 mm) for the plasma to exist inside the hole. Using the approximation $T_e \simeq 1.5 \text{ eV}$ ³ in the relation giving the Debye length in practical units $\lambda_D(\text{cm}) = 743 \sqrt{\frac{T_e}{n_e(\text{cm}^{-3})}}$, the electron density is given by:

$$n_e = \frac{743^2 T_e}{\lambda_D^2} \simeq 3 \times 10^{11} \text{ cm}^{-3} \quad (2.9)$$

This result agrees with measurements obtained for the glow mode density in section 3.2.2.

Filamentary mode

The axial view allows a much better analysis of the filament arrangements than the side view. In the axial view set-up, the Pyrex dielectric (which is not as thermal resistant as the 4 mm Alumina disk) was often destroyed by the filaments. The use of ITO was not possible in this mode because the glass layer it is deposited on is too fragile.

Many filament distributions are possible. They always exhibit a self-organization behaviour. In figure 2.13 the filaments do not cover the whole electrode area because the fine copper mesh placed under the Pyrex plate was not perfectly flat, hence the electric field is not constant everywhere. However, the distance between filaments is fairly regular and self-organisation is clearly discernible. Sometimes they form peculiar patterns such as the circle presented figure 2.14.

³ Approximation already made in section 2.2.2 to estimate the diffusion of an electron avalanche.

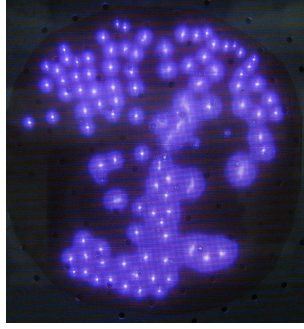


Figure 2.13: Axial view of plasma filaments

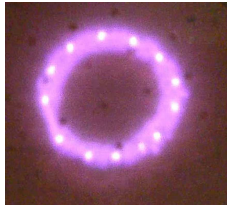


Figure 2.14: Filaments forming a circle from [Samuelli 2006](#)

2.2.3 Pulsing the RF power supply

The use of a pulse generator to turn the RF voltage ON and OFF was first motivated by the investigation of the early instants of the breakdown. When the electronic equipments and the optical system are triggered on the pulse generator, the ignition of the plasma can be studied.

It was remarkable that the pulsing parameters dramatically influences the plasma properties. It was even found possible to control the glow \rightleftharpoons filament transition simply by changing the pulse properties. The appropriate pulse periods and pulse widths that lead to one or the other mode are listed in section 2.2.5. In order to pulse the plasma an *Agilent 33220-A* waveform generator is plugged into the RF power supply.

In the PMT signal, 20 *ns* oscillations with a decreasing magnitude were observed as shown on figure 2.15. The rate of this decrease depends on the *RC* time response of the optical set-up. This isolated peak is due to the impact of a single photon on the first dynode of the PMT which is then amplified by the 10 following dynodes of the PMT. To obtain a larger and more significant value of the atomic line signal, the PMT voltage is averaged over 8 pulses.

The pulsed output voltage and the intensity of the 696.55431 *nm ArI* line are shown on figure 2.16. The RF voltage increases to a maximum in less than 1 μs (time response due to the matchbox) and reaches the value of 700 *V*. After the ignition of the plasma, the voltage drops to a lower constant value at 2 μs . The intensity of the *ArI* line

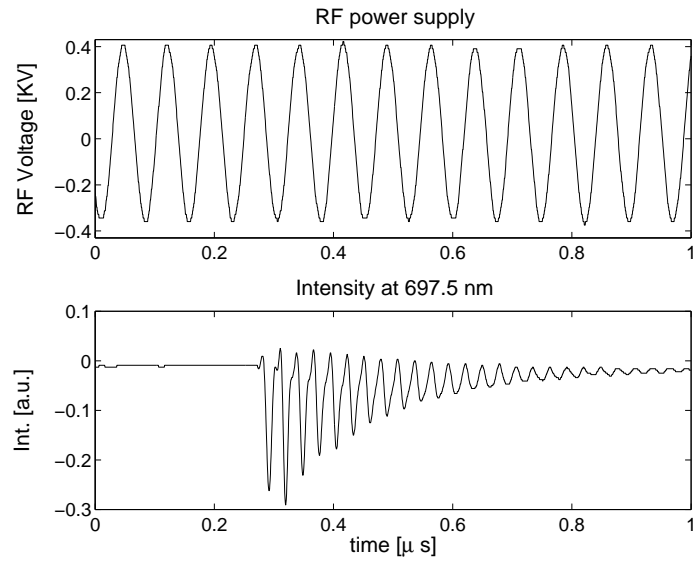


Figure 2.15: Oscillation in the PMT signal due to the impact of a single photon

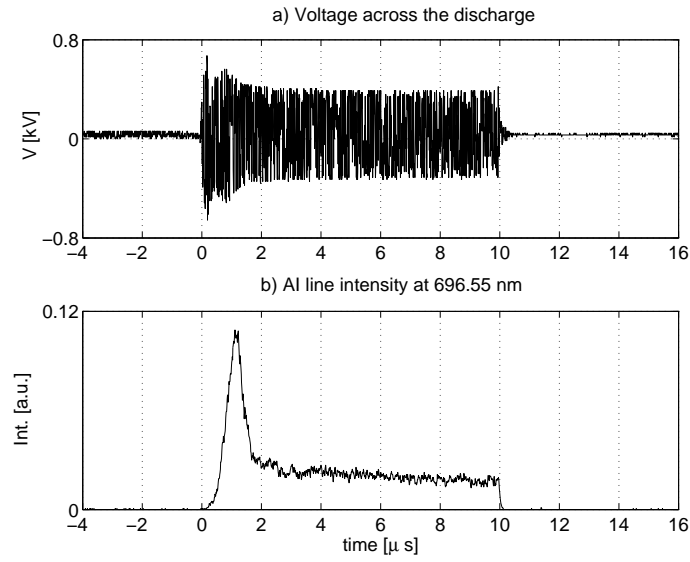


Figure 2.16: Evolution of an *ArI* line during a pulse

increases rapidly, reaching a maximum after $1\ \mu s$, then drops by over a factor of 5 when the voltage drops to become fairly constant at $2\ \mu s$. The light intensity drops to zero as soon as the pulse ends. This demonstrates that the plasma is turned off between each pulse. This behaviour was observed for all emission lines of the plasma spectrum.

When the discharge is pulsed in any mode, it is noticeable that the plasma which is usually silent in the continuous RF mode is actually making a noise. The pitch of the sound is the pulse frequency and changing the width of the pulse does not affect the sound. This indicates that only the breakdown at the beginning of each pulse creates a sound and that apart from this sound during the ignition, the discharge is silent. This sound is probably due to the momentum transfer from ions to neutral atoms of the gas.

2.2.4 Fast imaging

Current and voltage measurements do not make the modes discernible. No difference between the glow mode and the filamentary mode is noticeable in electric measurements (see section 3.1). The I curves and V curves are always similar to the one presented on figure 3.1. However, if the discharge is in a filamentary mode, a simple visual check will confirm it. This is the motivation of fast imaging investigations.

Axial and radial pictures with short exposure time were taken with a *Shimadzu Hyper Vision-1* camera. The CCD set-up and triggering system has been tuned with the help of Benjamin Powell from *Advanced Imaging and Inverse Methods* at the ANU. The camera performances are 100 frames of black and white video with a maximum frame rate of a million frames per second. The opening of the camera gate is triggered on the pulse generator.

Both the filamentary mode and the glow mode are pictured. The principles for the control of the glow \rightleftharpoons filament transition are expanded upon in section 2.2.5. The examination of the two different modes on a short time scale from both axis considerably helps the understanding of this transition.

Fast imaging of the filamentary mode

In figure 2.17 a sequence of 42 pictures is shown. The exposure time is set on $16\ \mu s$ and a picture is taken every $16\ \mu s$. Hence the total length of the sequence is $42 \times 16 = 672\ \mu s$.

The sequence is recorded when the plasma is in the filamentary mode. The RF power supply is pulsed with a $80\ \mu s$ pulse width and $900\ \mu s$ pulse period (duty-cycle of 9%). Between two pulses the gap is free of filaments but for each pulse, the filaments remain at the exact same spot even when the plasma is OFF for nearly a $1\ ms$. This confirms that the charges deposited on the dielectric remain on the surface for a time much longer than the plasma mechanisms time scale. Memory effects on periods longer than $10\ s$ have been encountered.

A sequence of radial pictures is also presented on figure 2.18. The exposure time is $2\ \mu s$ and a picture is taken every $2\ \mu s$. The pulse width is $16\ \mu s$ and the pulse period

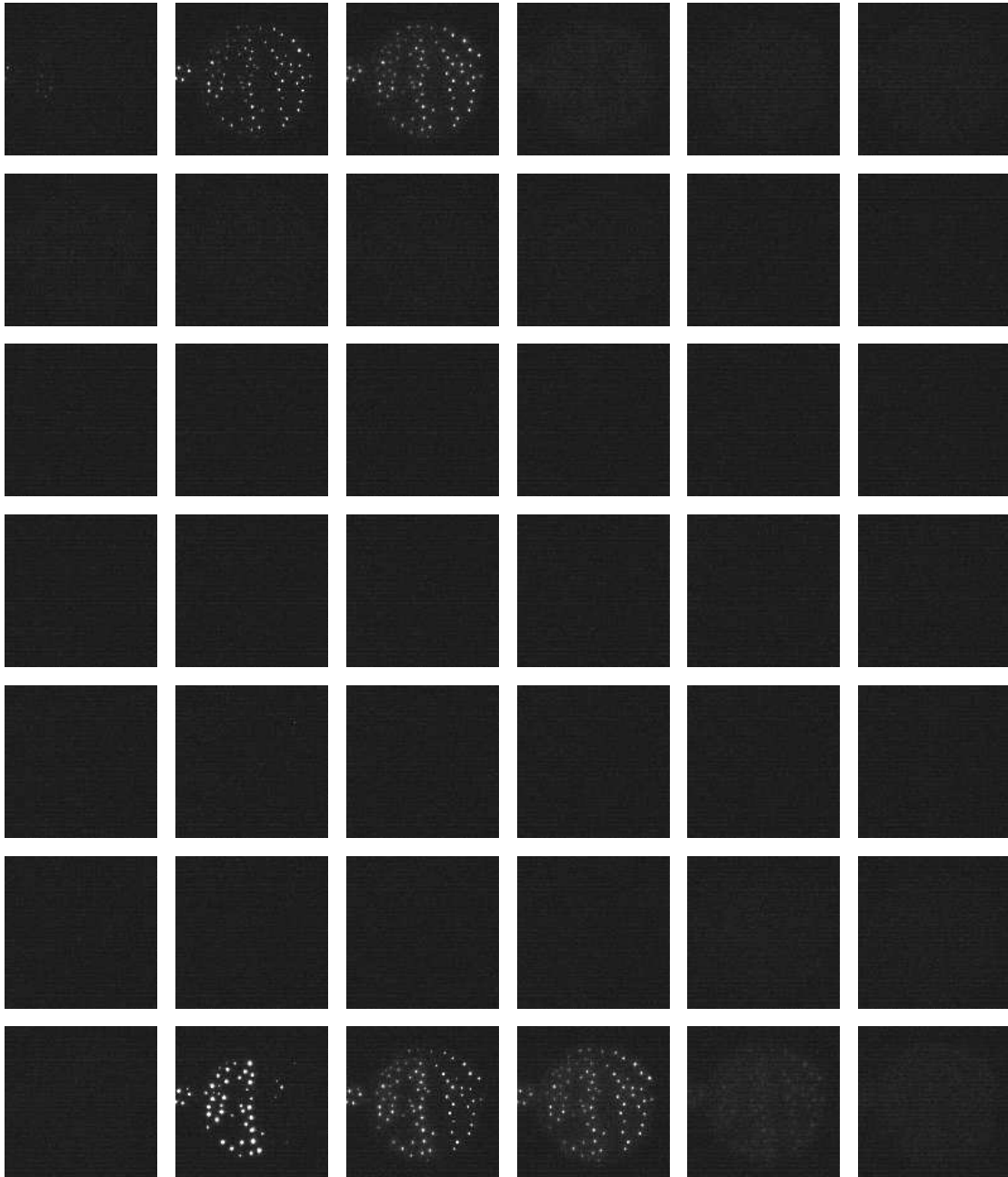


Figure 2.17: Axial pictures taken every 16 μs in the filamentary mode

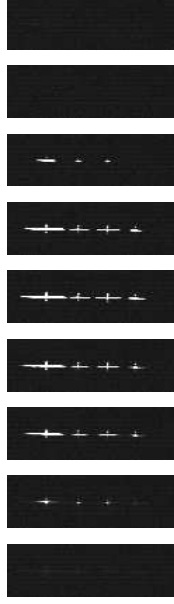


Figure 2.18: Radial pictures taken every $2 \mu s$ in the filamentary mode

is $600 \mu s$. 4 filaments are created at the ignition of the discharge. Their position, their number, and the distance between them remain constant. Only the intensity of the light they emit is changing during the pulse. The bright expansion perpendicular to the vertical filament is the reflection of the light on the Pyrex on the bottom electrode. This reflection is also seen by eye as illustrated on figure 2.7 (b).

Fast imaging of the glow mode

The sequence of figure 2.19 is composed of 4 pictures taken every $8 \mu s$. The exposure time is $8 \mu s$. The pulse width is $90 \mu s$ and the pulse period is $3 ms$. Although it is taken during a glow mode, a very bright filament that saturates the CDD detector appears in the second frame. In the second frame the main filament splits in four different filaments of lower brightness and smaller diameter. There is still the main initial filament in the middle, but not as bright or as large. Each of these four new filaments escapes the centre rapidly. Finally, on the last picture they have all faded away and the CCD does not detect the light of the glow mode which is now present over all the electrode area. This result indicates that the plasma that appears completely homogeneous with naked-eye inspection is actually the mode that is established after a filament ignition.

This is probably due to the difference between the breakdown voltage and the sustain voltage. During a very short time the voltage is at the breakdown value nearly two times higher than the sustain voltage. The high electric field at this instant probably favours the filamentary mode.

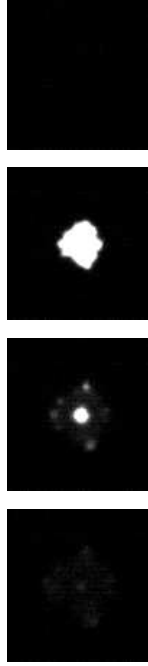


Figure 2.19: Axial pictures taken every $8 \mu s$ in the glow mode

2.2.5 Filament \rightleftharpoons glow transition controlled by pulse

As mentioned earlier, the mode of the discharge is not controllable when a continuous RF voltage is applied, but with a pulse RF signal both modes can be insured. The value of the pulse width associated with the value of the pulse period fixes the mode of the plasma.

For sufficiently small duty-cycle and short pulse widths the dielectric does not reach elevated temperatures. Immediately after the discharge is turned off a thermocouple is put in close contact with the dielectric surface and attached to the indicating device by a compensating cable. It indicates a dielectric temperature below $80^{\circ}C$. It is the gas that transfers heat to the dielectric, therefore the gas temperature is certainly close to the dielectric temperature below $100^{\circ}C$. In a continuous RF regime, the dielectric temperature can rise above $250^{\circ}C$. The relatively low gas temperature of the pulsed plasma makes the discharge mechanisms very different from the continuous RF regime.

With appropriate pulse parameters a stable homogeneous plasma can be sustained for as long as desired. It is also possible to select a filament mode in order to analyse their lifetime or the patterns they form. Figure 2.22 shows the limits of the two discharge modes in a pulse period versus pulse width diagram for an input power of $200 W$, a $2 mm$ gap and an argon debit of $1 L/min$.

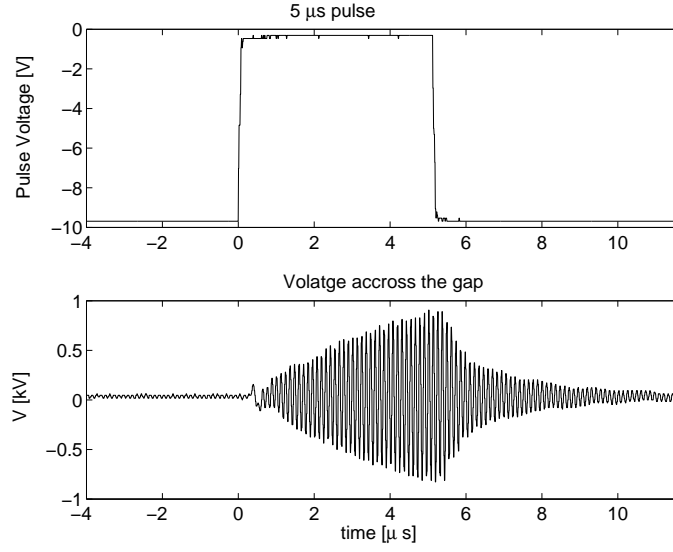


Figure 2.20: Pulse width limit of $5 \mu s$

As observed with the axial fast framing camera (sequence 2.19), the ignition of the pulsed glow mode is composed of filaments that last for approximately $4 \mu s$. The evolution of the light intensity over a pulse (figure 2.16) also asserts the existence of bright event at the start of the discharge, before the voltage across the gap falls down.

It was found possible to isolate only the ignition filament phase by reducing the pulse width down to a minimum of $5 \mu s$. This minimum is due to the response time of the matchbox and of the RF power supply itself. When we decrease the pulse to $5 \mu s$ the voltage out of the matchbox has just enough time to reach the breakdown threshold. Then the pulse is stopped and so the RF power is turned OFF immediately after the maximum voltage has been reached. The glow mode that should follow the filamentary ignition does not have time to appear. Due to the time response of the whole electric circuit, pulse widths lower than $5 \mu s$ could not be investigated because the breakdown voltage could not be reached within such a short time.

A short pulse of $5 \mu s$ is presented on figure 2.20 as well as the corresponding voltage across the gap. The breakdown voltage is reached only at the end of the pulse. The complete pulse signal $100 \mu s$ periodic is shown on figure 2.21 (a). In this case filaments cover all the electrodes area. Their arrangement is perfectly steady and stable.

The reversed transition is tested: (a) \rightarrow (b)

Increasing the pulse width above $5 \mu s$ allows the glow mode to appear after the ignition phase. The voltage after $5 \mu s$ is lower than the ignition voltage⁴ which favours the glow mode.

⁴ The RF generator is not a Thevenin ideal voltage source. It can not deliver a constant voltage when a high current is going through the gas after the breakdown.

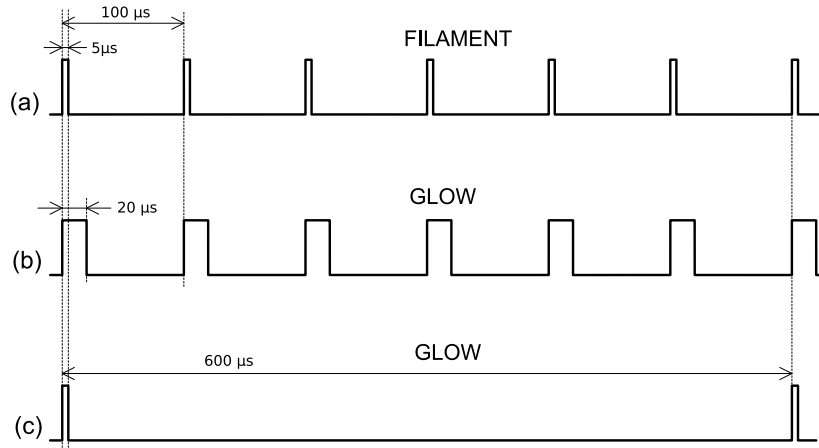


Figure 2.21: Pulse parameters

If the pulse width is still increased as close as possible to the pulse period value (reaching the 100 % duty-cycle limit) the problem of the minimum response time of the RF power supply and matchbox occurs again. Consequently the region where *pulse width* \mapsto *pulse period* was not investigated. However, it is probable that with a duty-cycle close to 100% the gas will get quite hot and will favour the apparition of filaments.

Transition signal (a) \rightarrow signal (c):

Another solution to return to the glow mode is to increase the pulse period without changing the pulse width as represented on the signal (c). When the pulse period is 1 ms and the pulse width is kept constant at 5 μs , the discharge changes from a filamentary mode to an apparent glow mode.

This transition is not very sharp and can occur in the opposite direction. As for the signal (b), the ignition of the glow discharge exhibits a phase of intense light emission and makes a noise which pitch is the pulse frequency. However, the level of the light intensity of these ignition filaments is much lower than for signal (a) and (b) and their lifetime is shorter ($\sim 2 \mu s$). The light peak is too short and too weak to be observed with the CCD but *ArI* lines peaks of approximately 2 μs wide are detected.

A possible reason for this transition is the low gas and dielectric temperature. Important differences are noted between the temperatures corresponding to signal (a) and signal (c). ($80^\circ C$ and room temperature $\sim 25^\circ C$ respectively).

Conclusion and interest of the pulse mode for surface treatment

In order to summarize this section dedicated to the characterisation of each mode, let us emphasize that the natural tendency of this argon discharge to turn into filaments

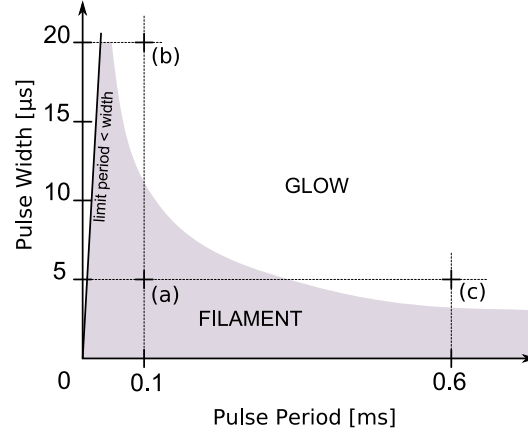


Figure 2.22: Filament \rightleftharpoons Glow transitions

can be controlled. This RF atmospheric argon discharge is very unstable but the use of a pulse generator which indirectly controls the gas and dielectric temperatures makes the whole system adjustable (pulse width and pulse period). The glow mode can be sustained for as long as desired regardless of the ambient conditions. Optical access to the discharge allows for more information about this apparent glow mode. Both fast CCD imaging and spectral lines measurements attest the presence of ignition filaments at the start of the glow mode.

This is not distinguishable with a mere naked eye observation. However it was found possible to avoid the formation of long life time filaments and to force a homogeneous discharge spread on the whole electrode area. Moreover, the observations of these transitions shed light on the parameters that control the existence of each mode. It is very likely that a high gas and dielectric temperature combined with a high electric field result in a filamentary mode.

When the RF generator is running continuously, both modes can exist depending on all the experimental parameters but also on ambient conditions which are not easily controllable (pressure and temperature). If the plasma is kept ON for more than a few minutes without being pulsed, it inevitably ends-up in a filamentary mode. In addition, for a continuous RF excitation the filament mode is found to be irreversible and more stable than the glow mode. On the contrary, pulsing the discharge is always efficient in forcing the glow mode regardless of the ambient conditions.

The values presented in figure 2.21 and 2.22 depend on the gap size, the argon flow and the RF voltage. However, even with different experimental parameters, limit values are very contiguous and similar transitions are observed leading to the same conclusions. In the continuous RF regime, the filaments live during all the RF ON time. When a pulse signal is used to control the mode, only short lifetime filaments $\leq 5 \mu s$ are observed.

For safe surface treatment, this mode control by pulse is of particular interest. Despite the existence of some filaments at the ignition of the glow mode, the polymer film

is never burnt. These filaments that only last for a few micro-seconds (not visible with the naked-eye) are not destructive, contrary to continuous RF ones.

Glow plasma modes are found for long pulse periods combined with short pulse widths leading to low gas and dielectric temperatures. In section 3.4 the efficiency of this plasma regime for the modification of the hydrophobicity of polymers is discussed.

Chapter 3

Plasma diagnostic and application to surface treatment

3.1 Electric measurements

The variations of the current through the gap is an easy access measurement that provides a lot of informations on the discharge properties. The most convenient current measurement method in DBDs running at around 10 kHz is to place a resistor in series with the electrodes. Most often a $50\ \Omega$ dummy load picks up the current to the ground.

Since the discharge is excited at 13.56 MHz the serial resistor is unusable because it disturbs the impedance matching. For the same reason, Lissajous figures measured with an external capacitor to calculate the power dissipated in the discharge are not applicable at 13.56 MHz . A current transducer is used instead. It acts as the secondary winding of a transformer, the first winding being the single loop created by the DBD circuit itself. Even if the mutual influence of the primary and secondary windings results in a equivalent resistance of a few Ohms, this measurement method is almost not disruptive for the impedance matching.

An induction current directly related to the discharge current runs through the clamp-on Rogowsky coil (300 MHz of bandwidth). The phase angle and the intensity of the induction current are related to those of the discharge current so that its properties can be measured without modifying the electric circuit formed by the RF power supply, the matchbox and the DBD.

Figure 3.1 shows the I-V curve for the homogeneous pulsed plasma when the gap is 2 mm . Only the regime which is established after $4\ \mu\text{s}$ is represented. For the ignition phase where bright filaments are present in the gas gap, the current plots are identical. All the I-V curves obtained for the filamentary mode are similar to those obtained for the glow mode. However, knowing that the filaments occupy a smaller surface area on the electrodes, the current density is greater for the filamentary mode even if the total current intensities are comparable.

After the breakdown, the plasma is sustained with an applied voltage of 250 V . The

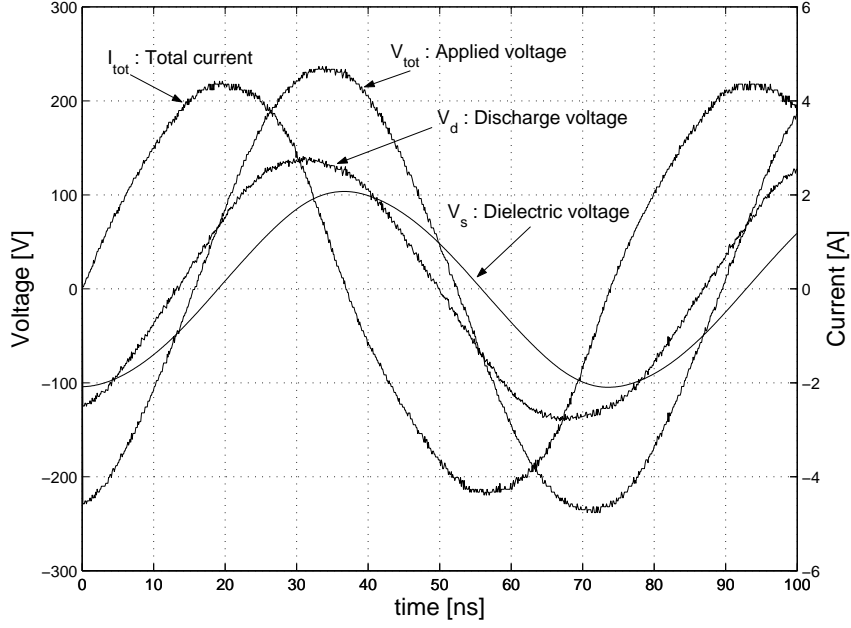


Figure 3.1: Gas voltage

current curve is almost analogous to a pure capacitive impedance where the current leads the voltage with a $\pi/2$ phase shift. A minor deformation is noticeable: the slight bump on the rising front of the I curve due a conduction current in the discharge after the breakdown and a phase shift lower than $\pi/2$ accounting for the resistive part of the discharge impedance. This contrast with usual DBD at 10 kHz in which sharp current peaks of only several nano seconds are observed. It shows that this experiment is similar to a RF capacitive discharge. Even in the filamentary mode, the I curve remains smooth and free of short current peaks.

The measured voltage corresponds to the total applied voltage V_{tot} . Some of this voltage drops across the solid dielectric layer V_s . This part of the voltage is not directly measurable but can be calculated from the total current I_{tot} that goes through the discharge:

$$V_s(t) = \frac{1}{C_s} \int_{t_0}^t I_{tot}(\tau) d\tau + V_s(t_0)$$

where C_s is the solid dielectric capacity and t_0 is the initial time for the integral which can be adjusted so that the average of V_s over a period is zero. An equivalent circuit of the DBD is sketched on figure 3.2. By subtracting the voltage across the dielectric from the total applied voltage we get the voltage across the gas gap:

$$V_d(t) = V_{tot}(t) - V_s(t)$$

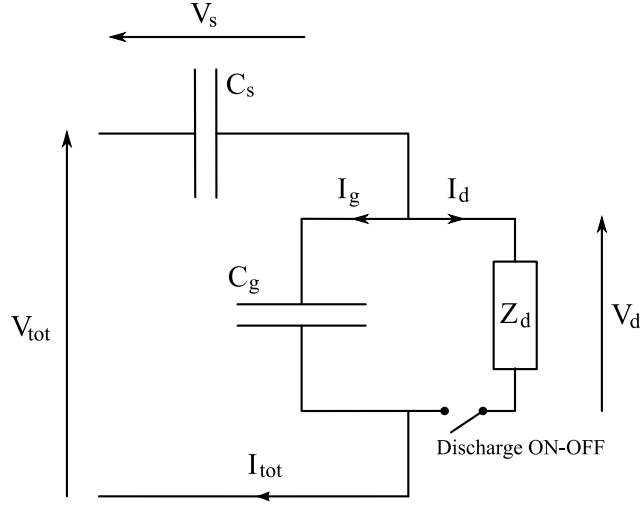


Figure 3.2: DBD equivalent circuit

The dielectric is a purely capacitive component so V_s and I_{tot} have a $\pi/2$ phase shift. The voltage across the gap has a phase shift with the total current lower than $\pi/2$ which is due to the resistive behaviour of the plasma. The actual voltage across the plasma is approximately 150 V. The I-V curve results of figure 3.1 agree with those reported in a recent study by [Shi et al. \(2006\)](#) on a helium RF DBD despite the fact that atmospheric discharges are more homogeneous in helium than in argon.

The power consumption displayed on the RF generator does not correspond exactly to the power dissipated in the plasma because of electric losses in the matchbox and in the parasite resistivity of the RF cables. The average power dissipated in the discharge is calculated from V_d and I_{tot} :

$$P = \frac{1}{T} \int_0^T I_{tot}(t) V_d(t) dt$$

In section 3.2.2 a method to evaluate the electron density from the dissipated power in case of a homogeneous glow discharge is expanded upon.

From the discharge voltage across the gas gap V_d , the displacement current due to C_g is found as follows:

$$I_g(t) = C_g \frac{\partial V_d(t)}{\partial t}$$

From I_g we obtain the discharge current through the impedance Z_d :

$$I_d(t) = I_{tot}(t) - I_g(t)$$

The current curves are shown on figure 3.3. The displacement current due to the gas gap capacity is much lower than the discharge current. The discharge current has a regular

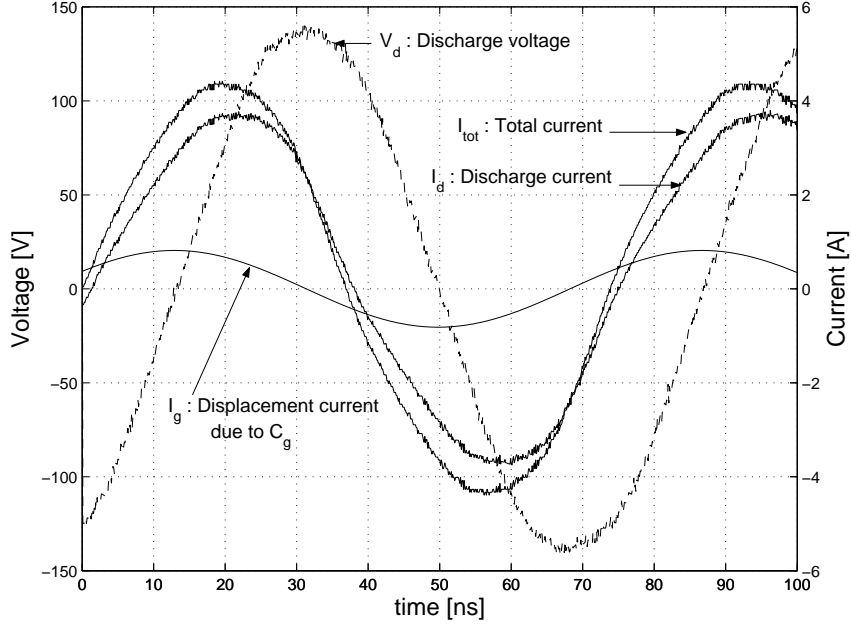


Figure 3.3: Conduction current in the discharge

sine like shape as observed in classical low pressure capacitive discharges (Raizer et al., 1995). This behaviour is common to the glow and the filamentary mode which proves that the filaments observed in this discharge have a different nature from the filaments present in 10 kHz DBDs (Massines et al., 2005) and that the discharge remains an RF capacitively coupled plasma even when it is only composed of filaments.

RF capacitively coupled discharges are known to operate in two modes. The α mode, also referred to as the normal mode, and the γ mode where a sheath breakdown occurs due to the importance of space charge from secondary emission and ionization (Raizer et al., 1995). The emission intensity near the electrodes in the α mode is much weaker than in the γ mode. In the γ mode, most of the light is emitted from the electrode vicinity (Raizer et al., 1995, Chapter 1.8 RF discharge modes).

In the present set-up, the vertical optical resolution is not sufficient to distinguish if the majority of the light is emitted in the sheath or in the bulk of the plasma. Whether the discharge operates in the α mode or in the γ mode could not be investigated in detail with plasma imaging.

However on picture 3.4 (a) the glow mode exhibits a dark region near the electrode so it is more likely that the discharge occurs in the α mode when the plasma is in glow mode. On picture 3.4 (b) the filaments are brighter than the glow plasma and most of the light comes from the electrodes (the bright region that extends on the electrodes is due to the filament reflection on their surfaces). Previous studies by Shi et al. (2003)



Figure 3.4: Comparison of the luminous regions position

and Moon (2006) indicate that the γ mode is less stable than the glow mode and results in a discharge contraction which causes the visual appearance of filaments. This suggests that a change in the mode is probably involved in the transition $\text{glow} \rightleftharpoons \text{filament}$.

3.2 Electron density

3.2.1 Filamentary mode - Stark Broadening

In the filamentary mode, the electron density is expected to be sufficiently high ($\geq 10^{13} \text{ cm}^{-3}$) to be determined by the Stark Broadening of the Balmer β hydrogen line. Electrons and ions in the plasma create a microscopic electric field around the excited atoms which perturbs their orbital energetic levels and thus the way they emit radiations. It results in a shifting and a broadening of spectral lines.

The Stark broadening affects all the atomic lines of the spectrum differently. The linear Stark effect is a perturbation depending on $1/r^2$ for the hydrogen atom and the quadratic Stark effect perturbation depends on $1/r^4$ for other atoms (r is the distance between the perturbation and the emitter). Electron density diagnostics based on Stark broadening have been performed on many different atomic lines. For instance the Stark broadening of the 696 nm argon line is measured by Dong et al. (2005) to give an electron density of $3.4 \times 10^{15} \text{ cm}^{-3}$ in an argon atmospheric pressure micro-discharge. In our condition the broadening of this argon line is not distinguishable among other dominant effects. Only the Stark broadening of the hydrogen $H\beta$ line is important enough to give a reliable electron density value.

There are other types of phenomena occurring in the plasma that produce a line broadening. Three pressure broadening mechanisms: Van der Waals, resonance and Stark contribute to the deformation of spectral lines emitted in the plasma. The theoretical shape of the hydrogen Balmer β line depending on the electron density has been widely studied. The $H\beta$ line shape at 486.1 nm gives a reasonable approximation of the electron density for values greater than $\sim 5 \times 10^{13} \text{ cm}^{-3}$ (Becker et al., 2004, Chapter 8.5.4 Measurements of electron number density by optical emission spectroscopy).

Water vapour is added to the discharge as a source of hydrogen which is dissociated

Broadening	FWHM in nm
$\Delta\lambda_{resonance}$	$60.4 \chi_H(P/T) \simeq 0.02$
$\Delta\lambda_{Van\ der\ Waals}$	$3.6 \times P/T^{0.7} \simeq 0.06$
$\Delta\lambda_{Doppler}$	$3.48 \times 10^{-4} \sqrt{T} \simeq 0.006$
$\Delta\lambda_{natural}$	6.2×10^{-5}
$\Delta\lambda_{instrumental}$	0.19
$\Delta\lambda_{Stark}$	$2 \times 10^{-11} (n_e)^{2/3}$

Table 3.1: FWHM for different broadening mechanisms (from [Becker et al. 2004](#)). P is the pressure in atmosphere T is the gas temperature in Kelvin (close to room temperature) χ_H is the mole fraction of hydrogen atoms ($\sim 10\%$) n_e is electron density in cm^{-3}

from the water molecule. The argon gas line is split: one of pure argon, and the other with argon going through a bubbler half filled with water (figure 2.5). Adding water vapour to the plasma disturbs its properties and it was not possible to find the glow mode even though the minimum water vapour possible was added to allow the $H\beta$ line to be detected in the spectrum background light of other species¹.

In theory the Stark broadening effect depends on both electron temperature and density, however for atmospheric pressure plasma in argon ($10^{11} \leq n_e \leq 10^{17} cm^{-3}$) the variation with electron temperature can be neglected ([Gigososy and Cardenoso, 1996](#)). Table 3.1 from [Becker et al. 2004](#) gives the Full Width at Half Maximum (FWHM) broadening values for all the mechanisms that affects the $H\beta$ line in these conditions.

Optical measurements are made on the radial axis as well as on the vertical axis with the transparent electrode. No difference in the line broadening is perceptible between those two view axes.

The openings of the two slits (input of the monochromator and input of the PMT) are set to $60 \mu m$. With a narrower opening the signal from the $H\beta$ line is too low to be detected; with a wider opening the instrumental resolution is not sufficiently high and the resulting spectral output would be the sum of several atomic lines rather than the $H\beta$ line. The calibration of the instrumental function was made with a mercury lamp on the HgI 546.075 nm line, and was found to be a Gaussian of FWHM 0.19 nm.

Of all the mechanisms independent of the electron density, the instrumental broadening is the largest by one order of magnitude. The main broadening mechanisms are taken into account to fit the experimental data ; the Doppler and the natural broadenings are neglected. Each broadening mechanism being independent of the others, the combined line profile is the convolution product of the line profiles of each mechanism. The Stark

¹ Adding electronegative oxygen may also slightly alter the electron density. The use of a $Ar-H_2$ gas mixture would have probably given better results

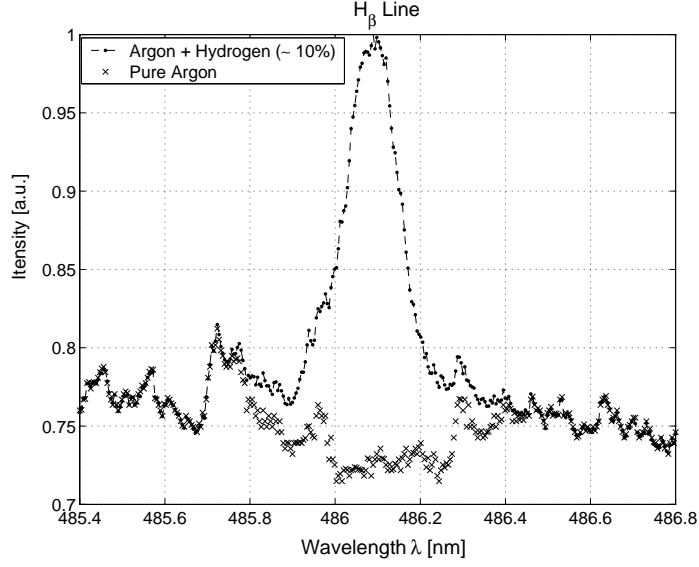


Figure 3.5: Spectrum with and without the $H\beta$ line

broadening, the Doppler and the resonance broadenings are known to be Lorentzian functions (Griem, 1997). The instrumental broadening is a Gaussian function.

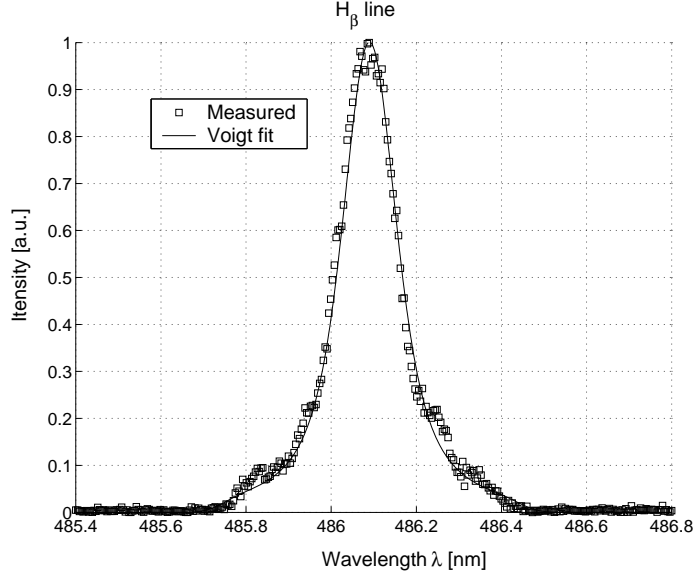
The integral value of each function must be equal, and the total convolution profile must fit the measured $H\beta$ line. The convolution of the three Lorentzian functions (Van der Waals \otimes resonance \otimes Stark) is a Lorentzian function so the overall convolution with the instrumental Gaussian is a Voigt function. In order to fit only the $H\beta$ line, the background spectrum signal is subtracted from the signal measured when hydrogen is added to the discharge² (figure 3.5). An example of fitting the Voigt profile to the measured line is shown in figure 3.6.

The average FWHM of the Stark Broadening for different monochromator settings is 0.22 nm resulting in an electron density of 10^{15} cm^{-3} (for filamentary mode). This value concurs with results obtained by other groups (Dong et al., 2005) who measured the Stark Broadening of an argon line.

3.2.2 Glow mode - Power Balance

The addition of hydrogen necessary to measure the Stark broadening of the $H\beta$ line disturbs the discharge so that the glow mode could not be observed even using the correct pulse parameters found in section 2.2.5. Furthermore the electron density in the glow mode is too small to produce a Stark broadening that could be deconvoluted from other broadening mechanisms. Hence, the Stark broadening method is not applicable in

² This Voigt fit is slightly altered from the published work Balcon et al. 2007.

Figure 3.6: Voigt fit of the H_β line

this situation.

The glow mode discharge is homogeneously spread over the whole electrode area, so the plasma density can be estimated from a power balance method described by [Lieberman and Lichtenberg \(1994, Chapter 3.5: Energy Loss per Electron-Ion pair Created – page 81 and Chapter 10.2 Electropositive Plasma Equilibrium – page 304\)](#). The energy lost by the system per electron-ion pair can be written:

$$E_{lost} = V_p + E_e + E_{col}$$

where, V_p is the plasma potential (kinetic energy gained by each ion falling down the wall sheath of $\sim 5kT_e$), E_e is the kinetic energy of electrons lost to the wall ($\sim 2kT_e$), E_{col} represents the collisional energy loss per electron-ion pair created (taking into account the ionization potential, the excitation energy lost per photon in radiation and elastic collisions with neutrals).

E_{lost} depends on T_e which is expected to be between 1 and 2 eV ([Park et al., 2001](#)), and under these conditions E_{lost} can be reasonably approximated to 50 eV for argon ([Lieberman and Lichtenberg, 1994](#)). The total power absorbed by a capacitively coupled plasma can be written:

$$P_{abs} = 2A e n_e v_b E_{lost}$$

where $2Aen_e v_b$ represents the total current of the discharge over the area $2A$ of the two electrodes ($A = 78.5 \text{ cm}^2$), v_b is the Bohm velocity (which equals the ion sound speed, in our conditions $\sim 2 \times 10^5 \text{ cm.s}^{-1}$).

Here we are ignoring the large sheath that is formed at low pressure from the self bias voltage which dominates power loss for these discharges. The present system is very collisional and it is not clear how the high pressure sheath on the powered electrode would behave hence we have ignored it for the present estimate³.

P_{rf} is calculated from the current values measured on the Rogowski coil and the voltage across the gap (section 3.1). The balance between $P_{rf} = 200\text{ W}$ and the power dissipated in the plasma P_{abs} leads to:

$$n_e = P_{rf} / (2Aev_b E_{lost})$$

$$n_e \simeq 5 \times 10^{11} \text{ cm}^{-3}$$

This is consistent with the estimation of $3 \times 10^{11} \text{ cm}^{-3}$ obtained in equation 2.9 in section 2.2.2.

The electron density in the glow mode is about 2000 times less than the electron density in the filamentary mode (calculated in section 3.2.1) and is possibly due to the different area of the filamentary discharge compared to the glow discharge. If the same loss mechanism for the glow mode and filamentary mode is assumed, one would expect the total area covered by the filaments to be $78.5 \text{ cm}^2 / 2000 \simeq 4 \times 10^{-2} \text{ cm}^2$. From the burn marks left on the polymer film when the discharge was in a filamentary mode, the diameter of a single filament is estimated to be approximately 0.1 mm (area of $3.14 \times 10^{-4} \text{ cm}^2$) hence around 130 filaments are expected over the electrode area which is in good agreement with the observation.

3.3 Electron temperature

Under certain conditions of equilibrium and optical thinness, intensity ratios of argon atomic lines give a reasonable approximation of the electron temperature. The elementary line ratio method (known as the Boltzmann plot), where intensities from a single stage of ionization are compared, is an imprecise method when the levels of energy are within the range of kT_e . More accuracy is gained from the comparison of intensities from successive ionization levels with the Saha equation.

The spatial resolution of the optical system does not allow the comparison of the electron temperature in the sheath and in the bulk of the plasma (2 mm gap). Thus the resulting electron temperature is not resolved vertically.

These measurements are valid if the source is optically thin in the direction of observation. This condition is fulfilled when most of the photons escape the plasma without being absorbed and remitted too many times.

3.3.1 Optically thin plasma

With the transparent electrode set-up the Abel inversion described in [LeToulouzan 1981](#) is not required. Through the bottom electrode, it is possible to analyse the radial

³ If it is taken into account the plasma density would need to be about a factor of 3 lower.

dependence of the spectral lines. The amount of radiation trapping and the gas flow are the only values that vary along the radius of the electrode. A photon emitted in the centre of the plasma cylinder is more likely to be absorbed than a photon emitted at the edge of the plasma and the gas speed increases with the distance from the centre.

A simple optical mask placed on the mirror (figure 2.4) or a translation of the optical fibre relative to the lens allows us to select from which part of the plasma disk image we collect light. It is found that there is no significant difference between the spectrum near the edge and the spectrum at the centre. Furthermore, the spectral data acquired with the transparent electrode set-up are similar to the radial axis data. This indicates that the radiation trapping is not an important phenomenon in this discharge despite the important density of the neutral species.

The optical thinness can be validated with the calculation of absorption coefficients for the set of wavelengths we have computed. For a transition line of wavelength λ_0 the absorption coefficient is given by the following equation:

$$\kappa(\omega) = L(\omega) \frac{\lambda_0^2 g_2}{4\tau_0 g_1} n_{Ar^*} \quad (3.1)$$

where g_1 and g_2 are the statistical weights of the upper and lower levels of the transition respectively. τ_0 is the natural life time of the excited state and n_{Ar^*} is the density of the lower level that can absorb the radiation. The density of metastable Ar^* is approximately $3 \times 10^{18} \text{ cm}^{-3}$ (see section 5.2.2 and Oda et al. 2006). $L(\omega)$ is the Lorentzian profile defined by:

$$L(\omega) = \frac{\Delta\omega_p/2\pi}{(\omega - \omega_0)^2 + \Delta\omega_p/4} \quad (3.2)$$

The measured FWHM $\Delta\omega_p$ is lower than 0.5 nm for all the wavelengths of table 3.2. The absorption coefficient of the 696.5 nm line is shown on figure 3.7. It exhibits a maximum of approximately 2.5 m^{-1} for λ_0 which means that for a photon of this wavelength, the mean free path is 2.5 m . The mean free paths for all the wavelengths of interest are of this order of magnitude. This is much larger than the dimensions of the plasma which is thus considered to be optically thin.

In these optical thinness conditions, the absolute intensity of the ray corresponding to the transition $a \rightarrow b$ is given by:

$$I_{ab} = \frac{L}{4\pi} hc \frac{A_{ab}N_a}{\lambda_{ab}} \quad (3.3)$$

where L is the plasma length along the view axis, h is the Plank constant, c is the celerity of light in vacuum, A_{ab} is the probability of the transition $a \rightarrow b$ (Einstein coefficient), N_a is the population of the upper level of the transition and λ_{ab} is the wavelength of the radiation.

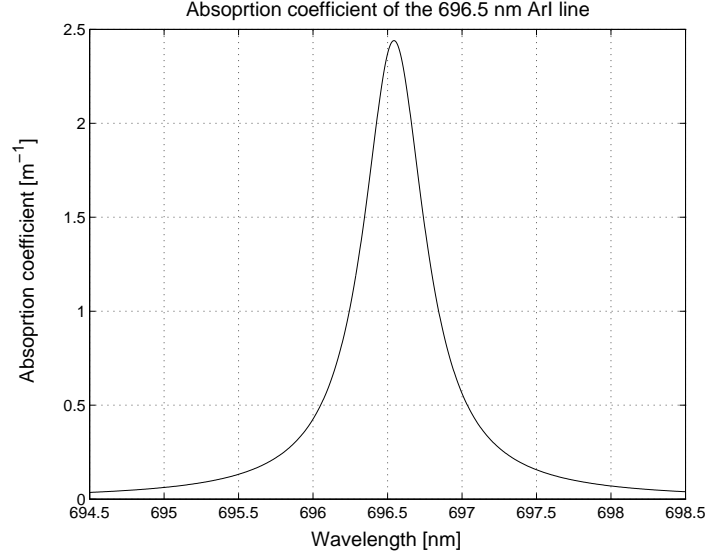
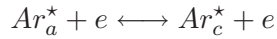


Figure 3.7: Absorption coefficient

3.3.2 Boltzmann plot

The use of the Boltzmann plot method requires at least partial Local Thermal Equilibrium (pLTE) between the upper levels of each transition (Griem, 1997). The Thermodynamic Equilibrium is said to be local (LTE) when sub-systems of different temperatures are analysed separately as in this atmospheric pressure RF CCP where the gas remains close to room temperature. Given the importance of electron impact collisions at atmospheric pressure, the electron velocity is assumed to be close to a Maxwellian function so one can speak about the local electron temperature.

In the case of the partial LTE, only part of the atomic system is ruled by a Boltzmann balance which describes the exchange of internal energy:



The forward reaction of excitation and the backward reaction of de-excitation compensate each other.

The higher excited states form the partial system in equilibrium. In this hypothesis, for two transitions $a \rightarrow b$ and $c \rightarrow d$ (see the Grotrian diagram, figure 3.8) the Boltzmann distribution relation is:

$$\frac{N_a}{N_c} = \frac{g_a}{g_c} e^{(E_c - E_a)/kT_e} \quad (3.4)$$

where k is the Boltzmann constant, T_e is the electron Temperature, N_c is the population of the upper level of the transition $c \rightarrow d$, g_a and g_c are the statistical weights of levels a and c , E_a and E_c are the energies of the levels a and c .

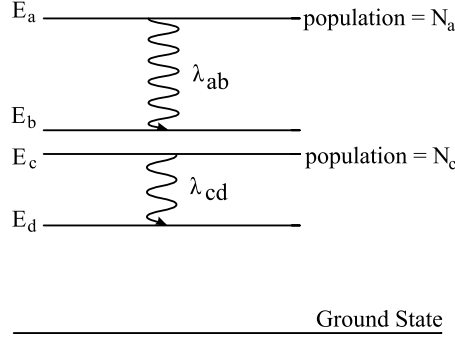


Figure 3.8: Grotrian diagram

Equation 3.4 can be arranged so that the density of the species excited to level a can be written:

$$N_a = \frac{N}{Z} g_a e^{-E_a/kT_e} \quad (3.5)$$

where N is the total population and Z is the canonical partition function: $\sum_i g_i e^{-E_i/kT_e}$. Combining equations 3.3 and 3.5 yields:

$$I_{ab} = \frac{L}{4\pi} hc \frac{N}{Z} \frac{A_{ab}g_a}{\lambda_{ab}} e^{-E_a/kT_e}$$

The plot of $\ln(I\lambda/gA)$ as a function of E_a for each ArI line, gives points which would be perfectly aligned in the case of a plasma in LTE. The slope of this line is $-1/kT_e$ leading to T_e . This method was tested on an inductively coupled plasma of fairly well known parameters where it is possible to decrease the pressure to check how the electron temperature would vary. A picture of this ICP source is shown on figure 3.9.

On figures 3.10 (a) and (b), the slope of the $-1/kT_e$ line is given by the least square algorithm which minimizes the sum of the squared errors. Some points are relatively distant from the main line so for the corresponding atomic transitions the pLTE hypothesis is questionable. However, the Boltzmann plots obtained with 25 ArI lines for 7 mT and 150 mT in the ICP lead to temperatures in agreement within 25% with Langmuir probe measurements made by Sutherland (2005, Chapter 4). As expected, the electron temperature decreases when the pressure increases.

This Boltzmann plot method is very sensitive to the ratio between kT_e and the upper energies of the transitions. The energy spread is approximately 4 eV which is relatively close to the electron temperature. When the Boltzmann plot method is applied to the ArI lines seen in the atmospheric pressure capacitive discharge, the energy spread of the upper levels of ArI is too small compared to kT_e and the results are not realistic. In order to obtain a higher accuracy, it is necessary to compare the line intensities between different levels of ionization.

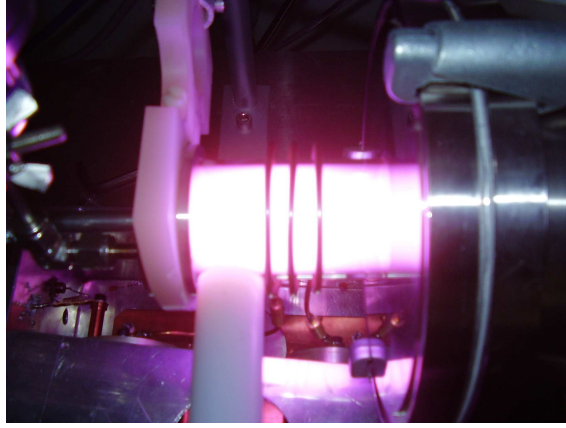
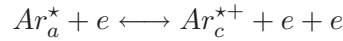


Figure 3.9: ICP source

3.3.3 Saha equation

When spectral lines from ArI and $ArII$ are compared there is at least the ionization potential difference between the energetic levels. This potential is nearly 10 times greater than kT_e which makes this method much more accurate than the Boltzmann plot. The comparison between neutrals and ions requires the use of the Saha equation which contains the electron density. It is important to point out that the density has to be known from an independent measurement of which the validity will directly affect the temperature estimation.

A partial local Saha equilibrium (pLSE) has to be assumed. For the pLSE to be valid, the same conditions as for the pLTE have to be fulfilled (pLSE \Rightarrow pLTE) and in addition the balance between the production and destruction of electrons has to be in equilibrium ([van der Mullen et al., 1994](#); [Griem, 1997](#)).



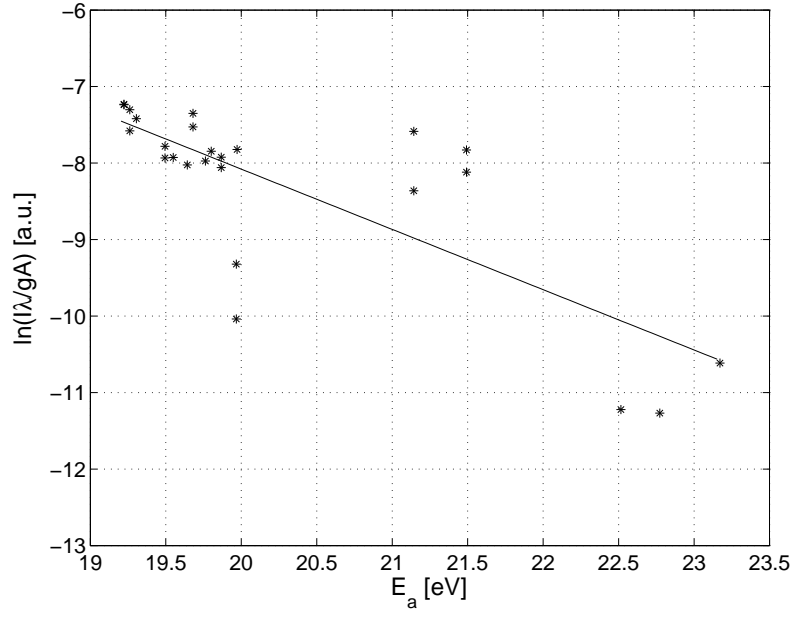
In the electron-induced Saha equilibrium, ionization and three bodies recombination are balanced and in addition the Boltzmann equilibrium is achieved. At atmospheric pressure, the system is highly collisional so atomic and ionic transitions of the higher level are mainly induced by free electrons. Hence a pLSE between the upper levels of each transition is not a bad assumption. The Saha equation for the excited ions and neutral is:

$$\frac{n_e N_+}{N_n} = 2 \frac{g_+}{g_n} \left[\frac{2\pi m_e k T_e}{h^2} \right]^{3/2} e^{-(E_a - E_c + E_i)/k T_e} \quad (3.6)$$

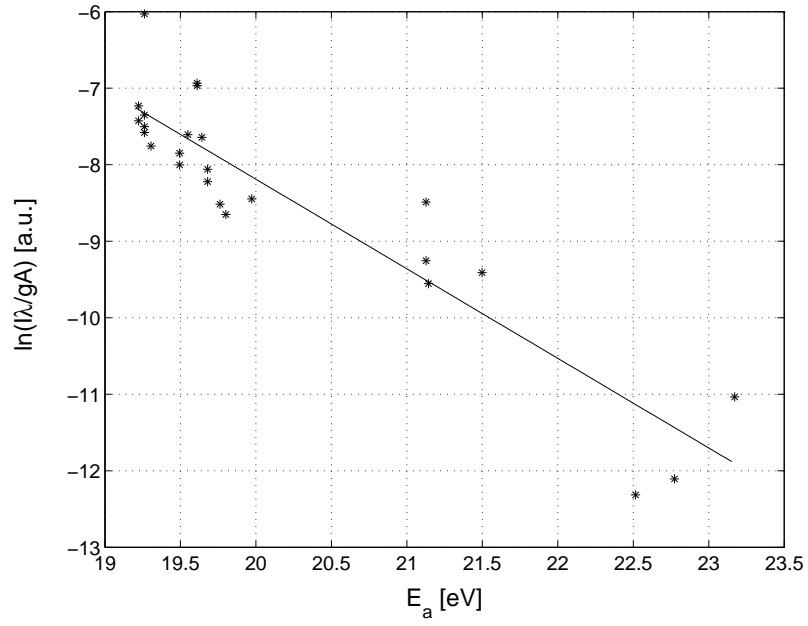
where:

E_i is the ionization potential of argon

N_n is the population of the upper level of a given transition $a \rightarrow b$ of neutral argon (ArI)



(a) Boltzmann plot for ICP at 7 mT, $T_e \simeq 1.27$ eV



(b) Boltzmann plot for ICP at 150 mT, $T_e \simeq 0.85$ eV

Figure 3.10: Boltzmann plots for the ICP source

	Wavelength [nm]	Transition configurations	$E_i - E_k$ [eV]	$g_i - g_k$
<i>ArI</i>	696.5431	$3s^23p^5(^2P_{3/2}^\circ)4s - 3s^23p^5(^2P_{1/2}^\circ)4p$	11.54 – 13.32	5 – 3
	750.3869	$3s^23p^5(^2P_{1/2}^\circ)4s - 3s^23p^5(^2P_{1/2}^\circ)4p$	11.82 – 13.47	3 – 1
	772.3761	$3s^23p^5(^2P_{3/2}^\circ)4s - 3s^23p^5(^2P_{3/2}^\circ)4p$	11.54 – 13.15	5 – 3
<i>ArII</i>	413.1724	$3s^23p^4(^1D)4s - 3s^23p^4(^1D)4p$	18.42 – 21.42	4 – 2
	427.7528	$3s^23p^4(^1D)4s - 3s^23p^4(^1D)4p$	18.45 – 21.35	6 – 4

Table 3.2: Spectral data of levels from *NIST* (Ralchenko et al., 2007)

line) and N_+ of the transition $c \rightarrow d$ of ionized argon (*ArII* line)
 g_n and g_+ are the statistical weights of levels a (neutral) and c (ionized), respectively.

Coupling equation 3.3 and 3.6 leads to:

$$\frac{I_+}{I_n} = \frac{2}{n_e} \frac{\lambda_n A_+ g_+}{\lambda_+ A_n g_n} \left[\frac{2\pi m_e k T_e}{h^2} \right]^{3/2} e^{-(E_a - E_c + E_i)/k T_e} \quad (3.7)$$

where:

I_n is the intensity of the *ArI* line (transition $a \rightarrow b$)

I_+ is the intensity of the *ArII* line (transition $c \rightarrow d$)

λ_n , λ_+ , A_n and A_+ are the wavelengths and probabilities of the transitions.

In equation 3.7, the temperature dependence of the intensities ratio is not only in the exponential term but also in the factor $(kT_e)^{3/2}$, hence it is impossible to use a graph based averaging of the temperature as done with a classic Boltzmann plot. However, for a given *ArI/ArII* ratio the electron temperature can be calculated from equation 3.7 as shown on figure 3.11. It represents the logarithm of the *ArI*₇₇₂₃/*ArII*₄₁₃₁ ratio as a function of T_e for a plasma density of $n_e = 5 \times 10^{11} \text{ cm}^{-3}$ (glow mode). The cross-over point between the curve $\ln(I_+/I_n)$ and the line representing the measured ratio yields the electron temperature.

All the computed argon lines are shown on table 3.2 Three *ArI* lines and two *ArII* lines will give six *ArI/ArII* ratios, each of them giving a temperature.

Six *ArI/ArII* ratios for the Saha equation lead to six temperatures which are found to be very close: only 5% variation between them. This validates “a posteriori” the

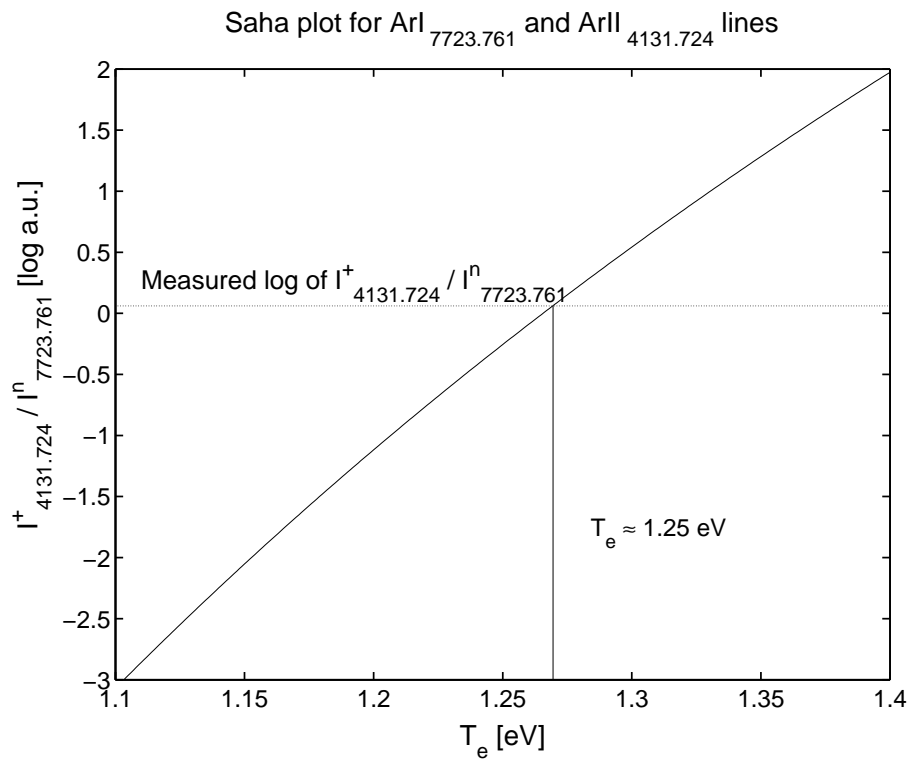


Figure 3.11: Example of $ArI/ArII$ ratio as a function of T_e

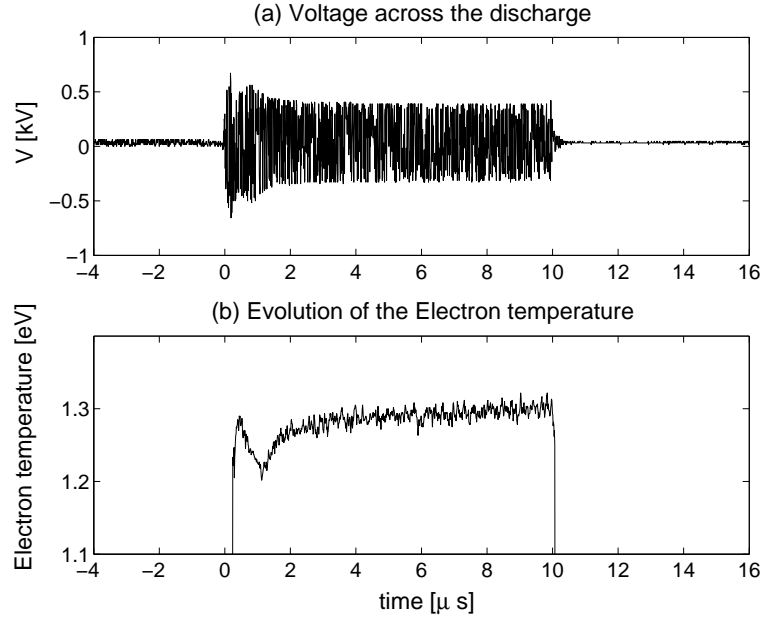


Figure 3.12: T_e during a $10 \mu s$ pulse in the glow mode using a constant $n_e = 5 \times 10^{11} cm^{-3}$

hypothesis that at least the excited states computed here are close to pLSE⁴.

An average of the six temperatures is calculated and the temporal evolution is observed during a $10 \mu s$ pulse width as represented in figure 3.12. For the same pulse, the intensity of all argon lines start with a peak at the beginning of the pulse and then decreases to reach a plateau as the voltage drops (the $696.5 nm$ line is represented on figure 2.16). The electron temperature also starts with a peak and decreases just after the voltage drops. Then, unlike the light intensity, it slowly increases to reach a plateau of greater value than the initial temperature even when the voltage stays constant at a lower value.

The measurements of the electron density from Stark broadening and power balance are not time resolved but averaged, hence the density values used in the Saha equation are constant for the pulse ON time. This is probably not very realistic as we know that the ignition of the discharge is composed of filament. It affects the temperature evolution since its calculation is based on the electron density. However, the average value of an electron temperature between 1.2 and 1.3 eV for the glow mode is reliable. A similar curve is obtained for the electron temperature in the filamentary mode but with a slightly greater value varying between 1.5 and 2 eV.

⁴ This does not validate the densities found in section 3.2. Another value of n_e would have also lead to approximately 5% contiguity even if the resulting temperature would have been different.

3.4 Surface treatment

One of the numerous applications of atmospheric pressure plasma is surface modification. The main advantage of surface treatment using non-equilibrium plasmas is the low temperature of reactive species. The external electric field accelerates the electrons much more than the heavy ions so that the gas is not in thermodynamic equilibrium. In the present discharge the electrons have an energy of approximately $1.5 \text{ eV} = 1.7 \times 10^4 \text{ K}$ whereas the gas temperature is much lower: around 300 K . This kind of two-temperatures plasma is often referred to as “cold” plasma.

In the CCP source studied here, the high value of the electron temperature is due to the electric field so that electron impact collisions create active species while the gas remains at a low temperature. At atmospheric pressure, given the high gas density, large currents can heat the electrodes and result in a thermionic emission of electrons. Therefore thermal arcs carrying a considerable current are likely to exist. The dielectric barrier limits the current through the gas in order to avoid the thermalization and surface damages.

The absence of vacuum systems and pumping down time is attractive for all the industries of plasma processes. Atmospheric pressure surface treatment has been widely studied in DBDs at 10 kHz (Massines and Gouda, 1998; Massines et al., 1998; Roth et al., 2005; Sira et al., 2005; Shenton and Stevens, 2001) and in RF capacitive discharges with dielectric barrier by Moon et al. (2003). In both cases the interaction of the plasma with the polymer surface increases its wettability. The source studied in this work is designed to optimize time efficiency of the treatment. The discharge is not enclosed in a vessel and argon flows in a not controlled atmosphere. Thereby the treatment of successive samples can be achieved “on line” (Hopfe and Sheel, 2007) which is of particular interest for textile and polymer manufacturers who have to deal with long surfaces.

With a continuous RF discharge the electrode and the dielectric quickly reach a temperature of 220°C , which may cause severe damage to the polymer. Besides, when the plasma is kept ON for a time long enough to affect the surface of the polymer, the continuous RF discharge turns into a filamentary mode. Even if the filaments are not extremely hot, they can locally melt or burn the polymer as they remain at constant positions. Moreover the filamentary discharge is not homogeneous so the surface functionalization would not be uniform.

The pulse parameters found in section 2.2.5 prevent this transition from occurring and at the same time the temperature of the polymer is reduced by a factor of 3 compared to a continuous mode. With a $100 \mu\text{s}$ pulse width and a pulse period of 1 ms (duty-cycle of 10 %) the temperature remains below 80°C and the discharge is prevented from turning into filaments.

The tested polymer is Polyethylene Terephthalate which is present in a large number of consumer products. It can be introduced in the gap when the discharge is already ON or before the breakdown. The wettability of the samples is tested with the sessile

drop method and Scanning Electron Microscope images are analysed.

3.4.1 Contact angle measurement

We evaluate the contact angle of a droplet of de-ionized water on the polymer with goniometer coupled with a software that fits circles onto the droplet image (*KSV CAM200*). The angle measurement requires two sets of data acquisition: one while filling the droplet and one when sucking the water out. If the liquid advances, the dry surface pushes on the contact line which increases the angle. When the surface has not been correctly cleaned, the droplet fills up but the contact surface with the polymer is contained by dirt particles, increasing the angle until the droplet becomes too large and expands brutally. Of course this diminishes the accuracy of the contact angle measurement but it is a convenient way to assess and compare the cleanliness of the samples. When the liquid recedes, the hydrophilic domain holds back the draining motion thus decreasing the contact angle. The resulting angle is the average of the advancing and receding angle

In figure 3.13 (a) and (b) the steady sessile droplet of de-ionized water on untreated and treated polymer is shown⁵. An increase in the hydrophilic behaviour of the polymer is observed: the untreated contact angle of the polymer sample is 90° and after one minute of exposure in the discharge (pulsed glow mode), the contact angle decreases to 53°. The Young equation gives the relation between the contact angle and interfacial free energies:

$$\sigma_{l/g} \cos\theta = \sigma_{s/g} - \sigma_{s/l}$$

where θ is the contact angle and $\sigma_{l/g}$, $\sigma_{s/g}$, $\sigma_{s/l}$ are the free energies of the interfaces for the phases liquid/gas, solid/gas and solid/liquid respectively. As $\sigma_{l/g}$ and $\sigma_{s/g}$ are constant, a diminution of the contact angle θ ($\cos\theta \nearrow$) results in a decrease of $\sigma_{s/l}$. This proves that the plasma affects the surface free energy of the polymer. The reason for this modification is debatable. Cleaning or etching effects that increase the surface roughness are sometimes mentioned. Indeed, surfaces covered with dust are often hydrophobic and etched surfaces are more porous and also more hydrophobic.

All samples were cleaned with a strong dry air spray at each stage of the process from the treatment to the contact angle measurements so it is very doubtful that only a mere cleaning of the surface is involved in the wettability increase. Furthermore a dirty surface would be identified from an important difference between the advancing and the receding angle in which case the wettability test would be cancelled. It is more probable that the energetic particles from the discharge break some bonds of the long carbon chains on the polymer surface. These free bonds created by impact of ions and radical species alter the interaction properties with water.

3.4.2 Scanning Electron Microscope

In order to observe the surface modification with more accuracy, high resolution pictures were taken with a *Hitachi S4500 Cold Field Emission Scanning Electron Microscope*.

⁵The static contact angles of pictures 3.13 (a) and (b) are not representative of the actual complete measurements.

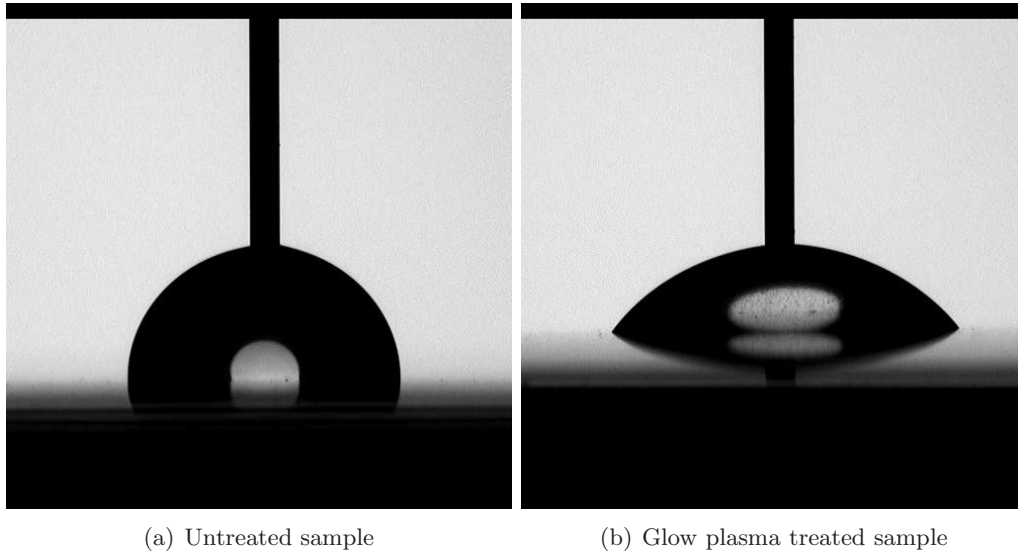


Figure 3.13: Contact angle measurements

The PET sample being an insulator, it must be coated with a metallic layer to create an image in the SEM. The treated samples were prepared for SEM by A. Caillard in the low pressure plasma reactor described in [Caillard et al. 2007](#). Approximately 4 nm of platinum is deposited by pulverization on the polymer sample.

On figure 3.14 the SEM images of the reference sample and the treated sample are shown. The polymer surface is rather slick, no micro burning marks are observed and no particular 3D structure is visible. However, it is noticeable that the platinum layer is cracked differently on each sample. The adhesion of the platinum on the polymer is poor for the untreated sample.

The SEM image 3.14 (b) shows fewer cracks which indicates a better adhesion of the platinum film on the PET. This proves that the surface modification is interesting not only for wettability improvement but also for polymer metallic coating or thin film deposition often needed in technological applications.

To evaluate the possibility of direct industrial applications, the time efficiency and the longevity of the surface modification were tested. Figure 3.15 (a) shows the evolution of the contact angle as a function of the exposure time in the reactor (pulsed glow mode). This does not take into account the 10 % duty cycle. The exposure time is the total residence time of the sample in the discharge so the effective time of interaction plasma/surface is 10 times lower. The pulse period might actually play a role in the surface modification as reactive species in the post-discharge can interact with the surface.

The contact angle variation is not linear, the surface modification is faster at the beginning of the treatment than after 10 seconds. A plateau is reached at 60 seconds which

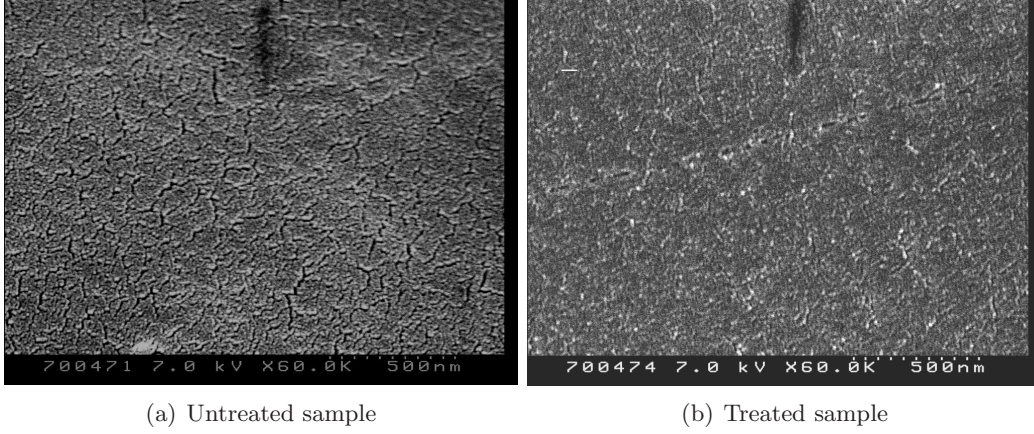


Figure 3.14: SEM images of polymer samples

is an acceptable time considering that this reactor is designed for “on-line” processes.

Figure 3.15 (b) shows that the surface modification is durable for a number of days (around two months before recovering the original wettability level). This is also valuable for industrial purposes in which logistic issues matter. Some surface treatments are efficient but last only for a couple of hours. The wettability increase obtained with this plasma source is steady enough to suit the long periods of time often involved in material processing. This long lasting effect also confirms that the surface modification is not simply due to surface cleaning but rather consists of destroying long chained molecules at the surface.

Conclusion

In order to conclude on this chapter we emphasize the electron density and temperature measurements in each mode of the discharge. In the glow mode the electron density is approximately $5 \times 10^{11} \text{ cm}^{-3}$ with a temperature of 1.5 eV . In the filamentary mode the density is 2000 times higher around 10^{15} cm^{-3} with a temperature of 1.7 eV . These values corroborate the simulation results obtained in the next chapters.

The optimization of the surface treatment mechanism is not the main purpose of this experiment. The results are encouraging but the performances can certainly be enhanced. The whole operation can be much more elaborated: many parameters such as gas flow, gas composition, gap between electrodes, applied voltage, pulse period and width can influence the treatment of different polymers. Surely the exposure time can be reduced by a large factor without affecting the treatment efficiency especially if we choose a polymer that resists higher temperatures.

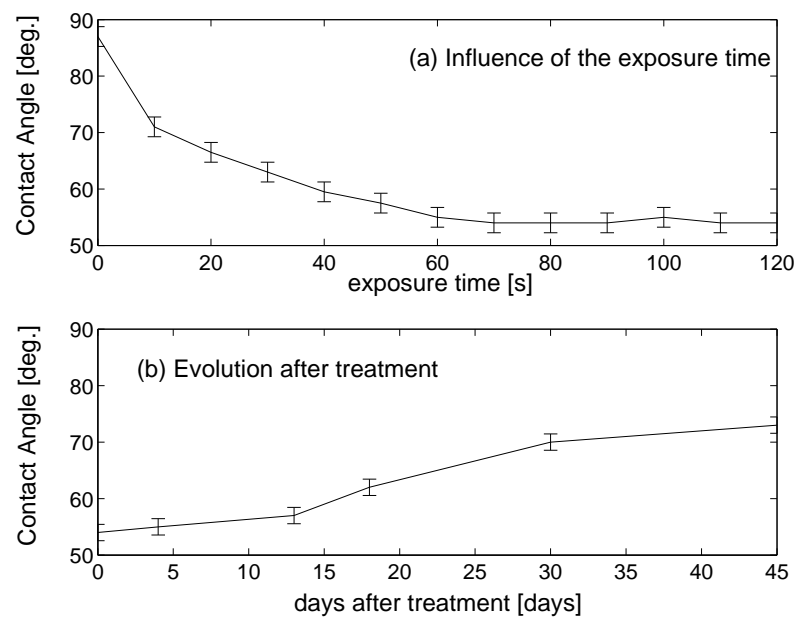


Figure 3.15: Evolution of the wettability

Chapter 4

Numerical model

4.1 Motivation

Spectroscopic and electric measurements give the main characteristic features of the capacitively coupled RF discharge. The electron density and temperature can be calculated from optical and electric data but some parameters are not directly measurable. In order to gain insight into the plasma behaviour, especially concerning the main ionization processes and the breakdown, a 1D fluid model is developed. Simulations also give time and space resolved information that helps in understanding the evolution of the gas discharge. These results can be used to optimize and control plasma parameters.

Section 2.1.4 led us to the conclusion that the gas is only composed of argon atoms. This simplifies the model which only has to account for argon kinetic. The choice for a unidimensional approach is justified by the symmetry of the experimental set-up. In addition, optical measurements resolved in the radial axis show that the parameters of the glow mode do not depend on the radial position. It is not the aim of the model to describe the filamentary mode hence the radial and azimuthal dimensions are not simulated.

Standard fluid models have already been successfully used in numerous and various plasma conditions (Boeuf, 1995; Hagelaar, 2000; Hammond, 2002). In this approach the plasma particles are represented by macroscopic quantities such as density, flux and mean energy. The model written during the thesis is based on the classical fluid equations obtained from common approximations and coupled with Poisson's equation.

In section 4.2 we describe the traditional fluid approach and the specificity of the model used to simulate the atmospheric pressure RF discharge. Writing a new model helps understanding its basic assumptions and its limitations and therefore a better interpretation of the results can be gained. It also provides a better versatility since the code is easily modified according to a particular need. For instance in section 4.4 an external circuit is added to the model to fit the experimental set-up. In the following sections the spatio-temporal solving methods and the boundary condition are detailed.

4.2 Governing equations

4.2.1 Moments of Boltzmann's equation

The evolution of particle positions and velocities in a unidimensional space is described by Boltzmann's equation as discussed in appendix A:

$$\frac{\partial f}{\partial t}(x, v, t) + v \frac{\partial f}{\partial x}(x, v, t) + a(x, t) \frac{\partial f}{\partial v}(x, v, t) = \left\{ \frac{\delta f}{\delta t} \right\}_{col}(x, v, t) \quad (4.1)$$

Where f is the distribution function of the considered particles. The only external force experienced by charged particles comes from the electric field so:

$$a = qE/m$$

where q is the charge and m is their mass. The plasma particles are electrons, ions and neutral atoms ; each kind of particle obeys its own Boltzmann's equation. The space charge field is taken into account by coupling Poisson's equation with Boltzmann's equation for each kind of particle.

Successive integrations of Boltzmann's equation over velocity space are performed. They lead to the velocity moments also known as the fluid equations (transport of mass, transport of momentum, transport of energy). A Boltzmann solver that calculates the electron energy distribution function is used in addition to the 1D model.

For electrons we use the transport and reaction coefficients calculated with the numerical solver *BOLSIG+* developed by Hagelaar and Pitchford (2005). In this Boltzmann solver the electron distribution function is calculated for different electric field values. When integrated with the collisional cross-sections the electron distribution function gives the transport and reaction coefficients.

For ions and neutral atoms the rate coefficients of electron impact reactions are also taken from *BOLSIG+* and the transport coefficients are found in various references of literature as described in section 4.5.

Particle conservation: the continuity equation

The first moment of Boltzmann's equation is obtained by an integration of equation 4.1 over the velocity space. First let us point out that for any variable $X(x, v, t)$, the mean value is given by:

$$\overline{X}(x, t) = \frac{\int X(x, v, t) f dv}{\int f dv} = 1/n \int X(x, v, t) f dv$$

Integral of Boltzmann's equation:

$$\int \left(\frac{\partial f}{\partial t} + v \frac{\partial f}{\partial x} + \frac{qE}{m} \frac{\partial f}{\partial v} \right) dv = \int \left\{ \frac{\delta f}{\delta t} \right\}_{col} dv$$

First term:

$$\int \frac{\partial f}{\partial t} dv = \frac{\partial}{\partial t} \int f dv = \frac{\partial n}{\partial t}$$

Second term:

$$\int v \frac{\partial f}{\partial x} dv = \frac{\partial}{\partial x} \int v f dv = \frac{\partial n \bar{v}}{\partial x}$$

Third term:

As E does not depend on v ¹ and $\forall x \quad f(x, v_{min}, t) = f(x, v_{max}, t) = 0$,

$$\frac{qE}{m} \int \frac{\partial f}{\partial v} dv = \frac{qE}{m} [f]_{v_{min}}^{v_{max}} = 0$$

The RHS term $\int \left\{ \frac{\delta f}{\delta t} \right\}_{col} dv$ is simply the source S of particles resulting from instantaneous, local destructions and creations by collisions at the position x and the instant t .

This 1D calculation can easily be extended to a 3D case with vectorial variables. The first moment of Boltzmann's equation accounting for the particle conservation can be written in its general form:

$$\frac{\partial n}{\partial t} + \nabla \cdot \mathbf{\Gamma} = S \quad (4.2)$$

Where $\mathbf{\Gamma} = n \bar{\mathbf{v}}$ is the particle flux. The source term is obtained either from the Townsend coefficient tabulated as a function of the reduced electric field in experimental references or from *BOLSIG+* (used with the corresponding experimental reaction cross sections).

Unless we make a very poor assumption on the particle mean velocity $\bar{\mathbf{v}}$, we ignore its value and its variation in space and time. Hence an equation for the particle velocity is required. Another integration of Boltzmann's equation is performed.

Momentum conservation

The conservation of the particles momentum $m \mathbf{v}$ is obtained by multiplying Boltzmann's equation by $m \mathbf{v}$ and integrating over velocity space:

First term:

$$\int m v \frac{\partial f}{\partial t} dv = m \frac{\partial n \bar{v}}{\partial t}$$

Second term:

$$\int m v v \frac{\partial f}{\partial x} dv = m \frac{\partial n \bar{v} \bar{v}}{\partial x}$$

We decompose the particle velocity as follows:

$$v = V + \bar{v}$$

Where V is the thermal velocity which satisfies $\bar{V} = 0$.

$$\bar{v} \bar{v} = \overline{V V} + 2 \overline{V \bar{v}} + \overline{\bar{v} \bar{v}} = \overline{V^2} + \bar{v} \bar{v}$$

$$m \frac{\partial n \bar{v} \bar{v}}{\partial x} = m \frac{\partial n \overline{V V}}{\partial x} + m \frac{\partial n \bar{v} \bar{v}}{\partial x}$$

¹ The case of a magnetic force depending on the particles velocity is discussed by [Bittencourt \(1986\)](#).

Third term:

As the force qE does not depend on the particle velocity:

$$\int mv \frac{qE}{m} \frac{\partial f}{\partial v} dv = qE \int v \frac{\partial f}{\partial v} dv$$

Using an integration by part:

$$qE \int v \frac{\partial f}{\partial v} dv = qE \int f dv = -nqE$$

RHS term:

$$\int mv \left\{ \frac{\delta f}{\delta t} \right\}_{col} dv = -mn \overline{\nu v}$$

Where ν is the momentum transfer frequency of collisions between the considered particle and neutral atoms.

Finally the complete equation is written:

$$m \frac{\partial n \overline{v}}{\partial t} + m \frac{\partial n \overline{V V}}{\partial x} + m \frac{\partial n \overline{v v}}{\partial x} = nqE - mn \overline{\nu v}$$

If we generalize to an isotropic 3D case, viscous forces appear in the non-diagonal terms of the tensor $\mathbf{V V}$. Let us call $\underline{\underline{p}}$ the pressure tensor.

$$m \nabla n \overline{\mathbf{V V}} = \nabla \underline{\underline{p}}$$

and the momentum conservation equation is:

$$m \frac{\partial n \overline{\mathbf{v}}}{\partial t} + m \nabla (n \overline{\mathbf{v v}}) = nq\mathbf{E} - \nabla \underline{\underline{p}} - mn \overline{\nu \mathbf{v}} \quad (4.3)$$

This equation can be simplified with the classical drift-diffusion approximation.

- Given the high density of neutral atoms, the electron-neutral collision frequency is much greater than the electric field frequency. Thus the electron inertia term $\frac{\partial}{\partial t} mn \overline{\mathbf{v}}$ is neglected.

For heavy ions and neutral atoms, it is necessary to ensure quantitatively that the ion-neutral collision frequency ν suffices for the inertia term to be negligible. We call m_p the ion mass and μ_p is the ion mobility. From

$$\mu_p = e / (m_p \nu)$$

it is possible to evaluate the order of magnitude of ν . For a typical electric field of 10 *Townsend* (which corresponds to 244 V/mm at atmospheric pressure) the mobility of Ar^+ ions is $\mu_p = 1.6 \times 10^{-4} m^2 V^{-1} s^{-1}$. With the argon mass of $m_{Ar} = 6.64 \times 10^{-26} kg$ The ion-neutral collision frequency is:

$$\nu = \frac{e}{m_{Ar} \mu} = 1.5 \times 10^{10} s^{-1}$$

This is three orders of magnitude higher than the applied RF frequency: $13.56 \times 10^6 s^{-1}$ so $\frac{\partial}{\partial t} mn \overline{\mathbf{v}}$ is negligible for ions as well.

- For electrons, the drift velocity due to the external field is negligible compared to the thermal speed: $\bar{v} \ll \overline{VV}$.
- For electrons, the temperature is related to the pressure by the following equation:

$$p = m_e \overline{VV} = n_e k T_e$$

Where k is the Boltzmann constant and T_e is the temperature.

$$\nabla p = k T_e \nabla n + k n_e \nabla T_e$$

Assuming slow time variations where electrons can exchange energy with their surroundings, the thermodiffusion $k n_e \nabla T_e$ is negligible compared to the diffusion $k T_e \nabla n_e$.

Equation 4.3 becomes:

$$m n \bar{v} \bar{v} = n q \mathbf{E} - k T \nabla n$$

$$n \bar{v} = \frac{n q}{m \bar{v}} \mathbf{E} - \frac{k T}{m \bar{v}} \nabla n$$

With the mobility of the particles expressed in $m^2 V^{-1} s^{-1}$:

$$\mu = \frac{|q|}{m \bar{v}} \quad (4.4)$$

and the diffusion coefficient in $m^2 s^{-1}$:

$$D = \frac{k T}{m \bar{v}} \quad (4.5)$$

the drift-diffusion equation becomes:

$$\begin{aligned} \mathbf{\Gamma} &= n \mu \mathbf{E} - D \nabla n && \text{For positively charged particles} \quad (a) \\ \mathbf{\Gamma} &= -n \mu \mathbf{E} - D \nabla n && \text{For negatively charged particles} \quad (b) \end{aligned} \quad (4.6)$$

Local Field approximation

To close the system and stop the successive integrations, the knowledge of μ , D and the source term S , which all depend on the electron mean energy, is necessary. The mobility of ions and neutral atoms is given in literature as a function of the reduced field and the diffusion coefficient D is calculated from the Einstein relation which arises from equations 4.4 and 4.5 :

$$D = \mu \frac{k T}{|q|}$$

For electrons, *BOLSIG+* can calculate the transport coefficients depending on the reduced field.

The tabulation of all the transport coefficients as a function of the local reduced field is known as the local field approximation. In this approximation, it is assumed that there is no transport of energy in the system other than collisional processes. In particular, it implies that the energy of electrons is directly linked, spatially and temporally to the electric field and that their heating is exactly balanced by the energy loss in collisions. This hypothesis can be unsatisfied in the regions of strong electric field. If the mean free path of electrons is not small with respect to the characteristic distance of field variations, electrons can gain energy at a particular position and dissipate it somewhere else.

Moreover, when the electric field is due to ambipolar diffusion and electrons are retained by this electric field, it is inconsistent to relate the energy of electrons to the reduced field. This occurs at the anode and in the bulk of the plasma which covers a large part of the gap.

For heavy particles with low mobility the local field approximation is valid but for electrons it is more appropriate to calculate another moment of Boltzmann's Equation describing the transport of their mean energy.

Besides, the use of the energy equation for electrons brings more stability and accuracy to the model. A first model based on the local field approximation has been tested. It leads to numerical instabilities that amplify themselves and propagate in the entire gap so that the model was not converging. Numerical stability was gained with the use of the energy equation, stationary solutions were found for conditions that would diverge with the local field approximation. The transport coefficients of electrons as well as the reaction coefficients as a function of the mean electron energy are calculated with *BOLSIG+* (see table 4.2).

Energy equation for the electrons

As done by Boeuf (1995) and Hagelaar (2000), instead of the local field approximation we use a more sophisticated and realistic model accounting for the transport of energy mainly carried by electrons in this very collisional discharge.

The kinetic energy gained by electrons in the electric field is transformed into a thermal random energy by frequent collisions. The term accounting for the kinetic energy due to their relatively slow drift motion is usually neglected so that:

$$\bar{\varepsilon} = \frac{3}{2}kT_e$$

where $\bar{\varepsilon}$ is the mean electron energy.

The energy transport equation is obtained by multiplying Boltzmann's equation 4.1 by $1/2 mv^2$ and integrating over velocity. Details of these calculus manipulations are found in Moisan and Pelletier 2006. After simplifications we find that the electron mean energy obeys a continuity equation:

$$\frac{\partial n_e \bar{\varepsilon}}{\partial t} + \frac{5}{3} \nabla \cdot (n_e \bar{\varepsilon} \mathbf{v}_e) + \nabla \mathbf{Q} + n_e e \mathbf{E} \cdot \mathbf{v}_e = -n_e \bar{\nu}_e \bar{\varepsilon} \quad (4.7)$$

Where \mathbf{Q} is the heat flux,

$n_e e \mathbf{E} \cdot \bar{\mathbf{v}}_e$ is the heating term representing the energy gained by electrons in the electric field,

$P(\bar{\varepsilon}) = -n_e \bar{\nu}_e \bar{\varepsilon}$ is the energy lost in collisions which depends on the mean energy itself.

In the momentum conservation equation 4.3 the electron inertia term was neglected because the frequency corresponding to the exchange of momentum by collisions is much greater than the frequency of the electric field. This is generally not the case for the kinetic energy that is exchanged by collisions at a much smaller rate than the momentum.

In equation 4.7 the electron mean energy flux appears as:

$$\nabla \Gamma_\varepsilon = \frac{5}{3} \nabla \cdot (n_e \bar{\varepsilon} \bar{\mathbf{v}}_e) + \nabla \mathbf{Q}$$

Let us call n_ε the electron mean energy density so that:

$$n_\varepsilon = \bar{\varepsilon} n_e$$

Then the energy flux is related to the electron flux by the following formula:

$$\Gamma_\varepsilon = \frac{5}{3} \Gamma_e \bar{\varepsilon} + \mathbf{Q} \quad (4.8)$$

The equation governing the evolution of \mathbf{Q} is obtained with another integration of Boltzmann's equation. The hierarchical system arising from successive integrations of Boltzmann's equation is closed when we assume that the heat flux is proportional to the temperature gradient:

$$\mathbf{Q} = -\lambda_e \nabla T_e$$

Where $\lambda_e = \frac{5}{2} k n_e D_e$ (Raizer, 2001) is the thermal conductivity coefficient, and as $\bar{\varepsilon} = \frac{3}{2} k T_e$ the equation for the heat flux is:

$$\mathbf{Q} = -\frac{5}{3} n_e D_e \nabla \bar{\varepsilon} \quad (4.9)$$

Combining the drift-diffusion equation 4.6 (b) for electrons with equations 4.8 and 4.9 leads to:

$$\begin{aligned} \Gamma_\varepsilon &= \frac{5}{3} \bar{\varepsilon} (-n_e \mu_e \mathbf{E} - D_e \nabla n_e) - \frac{5}{3} n_e D_e \nabla \bar{\varepsilon} \\ \Gamma_\varepsilon &= -\frac{5}{3} n_\varepsilon \mu_e \mathbf{E} - \frac{5}{3} (\bar{\varepsilon} D_e \nabla n_e + n_e D_e \nabla \bar{\varepsilon}) \\ \Gamma_\varepsilon &= -\frac{5}{3} n_\varepsilon \mu_e \mathbf{E} - \frac{5}{3} D_e \nabla n_\varepsilon \end{aligned} \quad (4.10)$$

where
 $\mu_\varepsilon = \frac{5}{3}\mu_e$ represents the mobility of energy.

$D_\varepsilon = \frac{5}{3}D_e$ represents the diffusion coefficient of energy.

As the energy is supposed to be carried by electrons, its “drift” is against the electric field:

$$\Gamma_\varepsilon = -n_\varepsilon\mu_\varepsilon\mathbf{E} - D_\varepsilon\nabla n_\varepsilon$$

If we note the heating term $H = -n_e e \mathbf{E} \cdot \bar{\mathbf{v}}_e$ Equation 4.7 has a simpler form similar to a continuity equation:

$$\frac{\partial}{\partial t}n_\varepsilon + \nabla \cdot \Gamma_\varepsilon = H - P(\bar{\varepsilon}) \quad (4.11)$$

4.2.2 Poisson’s equation

In order to make the model self-consistent, the electric field created by space charge needs to be calculated and then added to the external RF field. Poisson’s equation implies that the local charge is the source term for the spatial variation of the electric field:

$$\nabla \cdot \mathbf{E} = \frac{\rho}{\epsilon_0}$$

Since we do not apply any magnetic field in the experiment, the electric field derives from a potential as follows:

$$\mathbf{E} = -\nabla V \quad (4.12)$$

Then Poisson’s equation for the potential is:

$$\nabla \cdot (-\nabla V) = -\Delta V = \frac{\rho}{\epsilon_0}$$

4.2.3 Boundary conditions

Thermal velocity

As we do not impose a particle density at the edges of the discharge, a thermal velocity must be added to the flux on each side. A thermal velocity term $v_t/4$ is added to the fluxes at the walls. The thermal flux is given by:

$$\Gamma = n \frac{v_t}{4}$$

For electrons the thermal velocity is:

$$v_{t,e} = \sqrt{\frac{8 k T_e}{\pi m_e}}$$

with $kT_e = 2/3 \bar{\varepsilon}$.

For other heavy particles of mass m , we use the room temperature $T = 300\text{ K}$

$$v_t = \sqrt{\frac{8 kT}{\pi m}}$$

These boundary conditions are also applied to the mean electron energy which is treated as a particle of thermal velocity:

$$v_{t,\bar{\varepsilon}} = 5/3 v_{t,e}$$

Hence the energy flux due to thermal motion is:

$$\Gamma_{\varepsilon} = \frac{5}{3} v_t n_{\varepsilon}$$

The coefficient $5/3$ accounts for the fact that fast electrons carry more energy than slow ones.

Secondary emission

A particle p hitting the cathode releases γ secondary electron(s). The secondary emission coefficient γ is generally between 0 and 1. Its value depends on the particle, its energy, the electrode material and temperature. The expression of the electron flux due to secondary emission is:

$$\Gamma_{\gamma} = \sum_p \gamma_p |\Gamma_p|$$

and the total electron flux at the wall is

$$\Gamma_e = -\frac{1}{4} n_e v_t + \Gamma_{\gamma} + a \mu_e E n_e$$

with $a = 1$ if $E \leq 0$ (the drift velocity is directed towards the wall) $a = 0$ if $E \geq 0$ (the drift velocity is directed outwards the wall). This implementation of the secondary emission is not consistent with the experimental value of γ at the cathode. In experiments, γ is calculated as the ratio between the flux of secondary electrons and the particle flux to the electrodes. One solution would be to impose a thermal velocity of zero at the cathode. Given the variation of the plasma potential responding to the RF applied voltage, it is fairly delicate to detect which wall represents the instantaneous cathode. An alternative solution is exposed by [Hagelaar et al. \(2000\)](#). In the present model this inconsistency is not as critical as in DC discharges model. The parameter γ does not have a great influence on the simulation results.

Finally we emphasize that there is no secondary emission term for the electron mean energy. This is equivalent to the allocation of a 0 eV mean energy for every secondary electron.

4.2.4 System of equations

To summarize, all the governing equations of the model are gathered in the table [4.1](#) where s is the index for charged particles.

Electrons	Density	$\frac{\partial}{\partial t} n_e + \nabla \cdot \mathbf{\Gamma}_e = S_e(\bar{\varepsilon})$
	Momentum	$\mathbf{\Gamma}_e = -n_e \mu_e(\bar{\varepsilon}) \mathbf{E} - D_e(\bar{\varepsilon}) \nabla n_e$
	Energy	$\frac{\partial}{\partial t} n_{\bar{\varepsilon}} + \nabla \cdot \mathbf{\Gamma}_{\bar{\varepsilon}} = -e \mathbf{\Gamma}_e \cdot \mathbf{E} - P(\bar{\varepsilon})$ with $n_{\bar{\varepsilon}} = \bar{\varepsilon} n_e$ and $\mathbf{\Gamma}_{\bar{\varepsilon}} = -\frac{5}{3} n_{\bar{\varepsilon}} \mu_e \mathbf{E} - \frac{5}{3} D_e \nabla n_e$
Neutral atoms and ions	Density	$\frac{\partial}{\partial t} n_p + \nabla \cdot \mathbf{\Gamma}_p = S_p(\bar{\varepsilon})$
	Momentum	$\mathbf{\Gamma}_p = n_p \mu_p \mathbf{E} - D_p \nabla n_p$
Charged particles	Poisson's equation	$\nabla \cdot \mathbf{E} = \frac{1}{\epsilon_0} \sum_s q_s n_s$

Table 4.1: Governing equations for the model

4.3 Numerical solutions

Standard discretization methods well known for fluid models are used to solve this system of equations in space and time for particle densities. The numerical model is one dimensional along the axis perpendicular to the electrodes' surface. Let us call \hat{x} this axis and use i as the space index. This axis is divided in N intervals. The first node has the index 1 thus the last node has the index $N+1$. All the scalar variables are defined on the nodes and all the vector variables are defined through surfaces between the nodes. Therefore the scalar variables are defined from 1 to $N+1$ and the vector variables from 1 to N . The control volume is the volume around the nodes between two successive surfaces. In this volume all the scalar variables are constant. As shown on figure 4.1, the mesh is linear ($\forall 1 \leq i \leq N, x_{i+1} - x_i = d$). However it is coded in such a way that the use of a non-linear mesh is possible if required.

Initial particle densities are chosen for the first step of the simulation. At every iteration of the simulation all the equations of table 4.1 are solved over the entire mesh. The results of this spatial solving are then used for the next time step.

4.3.1 Solving the continuity equation and the particle flux

The transport of particles in this electric field is described by the continuity equation 4.2 with the expression of the flux given in equation 4.6. Each type of particle has a

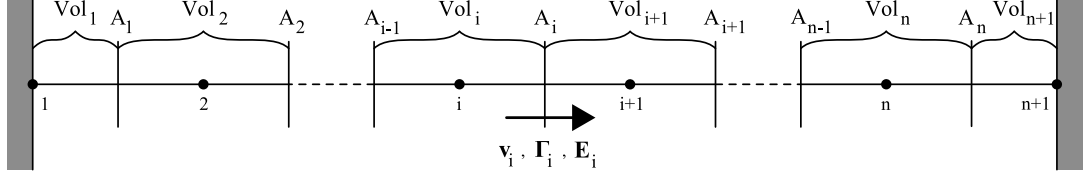


Figure 4.1: Mesh 1D

specific continuity equation and the energy equation for electrons also has the form of a continuity equation. Thereby the numerical solving will operate in a similar manner, and somehow the energy is treated like a particle of density $n_\varepsilon = \bar{\varepsilon}n_e$.

Given the low ionization degree of the gas discharge, the transport of uncharged and unexcited gas particles is neglected. The surrounding gas is considered to be an undisturbed infinite source of argon atoms.

For any type of particle, the continuity equation is:

$$\frac{\partial n}{\partial t} + \nabla \cdot \mathbf{\Gamma} = S$$

$$\mathbf{\Gamma} = n\mathbf{v}_d - D\nabla n$$

where S is the creation term (positive if particles are created, negative if particle are lost) and $\mathbf{v}_d = \pm\mu\mathbf{E}$ is the drift velocity of charged particles.

Integrating in the control volume Vol_i surrounded by the closed surface $Surf_i$

$$\iiint_{Vol_i} \left(\frac{\partial n}{\partial t} + \nabla \cdot \mathbf{\Gamma} \right) d\tau = \iiint_{Vol_i} S d\tau$$

Applying the Green-Ostrogradski Theorem leads to:

$$\iiint_{Vol_i} \frac{\partial n}{\partial t} d\tau + \oint_{Surf_i} \mathbf{\Gamma} \cdot \mathbf{n} ds = \iiint_{Vol_i} S d\tau$$

where \mathbf{n} is the normal vector to the local element of surface with $\|\mathbf{n}\| = 1$.

This equation is discretized as follows:

$$Vol_i \frac{\partial n_i}{\partial t} + A_i \Gamma_i - A_{i-1} \Gamma_{i-1} = Vol_i S_i \quad (4.13)$$

where A_i is the surface between two successive nodes.

Flux discretization

The particle flux is given in equation 4.6.

$$\mathbf{\Gamma} = n\mathbf{v}_d - D\nabla n$$

\mathbf{v}_d is discretized through the surface S_i as follows:

$$\Gamma_i = v_i (\alpha n_i + \beta n_{i+1}) - \frac{D_i + D_{i+1}}{2} \left(\frac{n_{i+1} - n_i}{x_{i+1} - x_i} \right)$$

When $\{\alpha = 0, \beta = 1\}$ the discretization is called the *upwind scheme* and when $\{\alpha = 1/2, \beta = 1/2\}$ it is the *central difference scheme*. The central difference scheme is stable only if the time step is chosen so that $\Delta t \leq \frac{\Delta x}{v}$

It is the purpose of the exponential scheme described by [Scharfetter and Gummel \(1969\)](#) to find the coefficients a_i and b_i depending on v_i , D_i , D_{i+1} , $(x_{i+1} - x_i)$ to get a flux $\Gamma_i = a_i n_i + b_i n_{i+1}$ that results in:

- Unconditional stability
- Exact solution for constant flux

The exponential scheme coefficients are found by treating equation 4.6 as a differential equation in n with the flux Γ and the drift \mathbf{v}_d assumed constant between mesh points. Hence this scheme is exact for a constant flux. The coefficients a_i and b_i are given in appendix B.

With a numerical time step Δt , equation 4.13 is discretized at step k :

$$Vol_i \frac{n_i^k - n_i^{k-1}}{\Delta t} + A_i \Gamma_i^k - A_{i-1} \Gamma_{i-1}^k = Vol_i S_i^k \quad (4.14)$$

The term n_i^{k-1} is known from the previous iteration, so it is added to RHS of the equation. Let us call $R_i = Vol_i \left(S_i^k + \frac{n_i^{k-1}}{\Delta t} \right)$. Equation 4.14 becomes:

$$Vol_i \frac{n_i^k}{\Delta t} + A_i \Gamma_i^k - A_{i-1} \Gamma_{i-1}^k = R_i \quad (4.15)$$

With the exponential scheme coefficients a_i and b_i , the continuity equation 4.15 becomes:

$$Vol_i \frac{n_i}{\Delta t} + A_i (a_i n_{i+1} + b_i n_i) - A_{i-1} (a_{i-1} n_i + b_{i-1} n_{i-1}) = R_i \quad (4.16)$$

Which can be written

$$c_i^W n_{i-1} + c_i^C n_i + c_i^E n_{i+1} = R_i$$

with:

West coefficient $c_i^W = -A_{i-1} b_{i-1}$
 Centre coefficient $c_i^C = A_i b_i - A_{i-1} a_{i-1} + \frac{Vol_i}{\Delta t}$
 East coefficient $c_i^E = A_i a_i$

The system of equations to be solved at step k is:

$$\begin{pmatrix} c_1^C & c_1^E & 0 & & & \\ c_2^W & c_2^C & c_2^E & 0 & & \\ 0 & . & . & . & 0 & \\ & 0 & . & . & . & 0 \\ & & 0 & c_N^W & c_N^C & c_N^E \\ & & & 0 & c_{N+1}^W & c_{N+1}^C \end{pmatrix} \begin{pmatrix} n_1 \\ n_2 \\ . \\ . \\ n_N \\ n_{N+1} \end{pmatrix} = \begin{pmatrix} R_1 \\ R_2 \\ . \\ . \\ R_N \\ R_{N+1} \end{pmatrix}$$

The density is not imposed on the electrode nodes and thermal velocities are added to Γ_1 and Γ_n as described in section 4.2.3. The temporal boundary conditions are initial densities. The system is solved from 1 to $N + 1$ with the matrix inversion performed using TRIDAG from (William et al., 1992). The necessary and sufficient condition for the solution to exist is that for all the terms of the matrix the following inequality is respected:

$$|c^C| \geq |c^E| + |c_i^W|$$

4.3.2 Solving Poisson's equation

Before coupling Poisson's equation with the transport equations, let us assume that we know the charge $\rho(x)$ and we want to determine the resulting potential $V(x)$. It is possible, especially in 1D, to solve equation 4.12 numerically with the finite difference method. However we prefer to consider the flux through surfaces:

$$\nabla \cdot \mathbf{E} = \frac{\rho}{\epsilon_0}$$

Integrating over the control volume Vol_i

$$\iiint_{Vol_i} \nabla \cdot \mathbf{E} \, d\tau = \iiint_{Vol_i} \frac{\rho}{\epsilon_0} \, d\tau$$

Applying Green-Ostrogradski theorem :

$$\oiint_{Surf_i} \mathbf{E} \cdot \mathbf{n} \, ds = \iiint_{Vol_i} \frac{\rho}{\epsilon_0} \, d\tau \quad (4.17)$$

Where $Surf_i$ is the closed surface around the volume Vol_i . Equation 4.17 is discretized as follows: (ρ is constant ($= \rho_i$) in the control volume Vol_i)

$$E_i A_i - E_{i-1} A_{i-1} = Vol_i \frac{\rho_i}{\epsilon_0}$$

The electric field is $E_i = -\frac{V_{i+1}-V_i}{x_{i+1}-x_i}$ so that:

$$-\frac{V_{i+1}-V_i}{x_{i+1}-x_i} A_i + \frac{V_i-V_{i-1}}{x_i-x_{i-1}} A_{i-1} = Vol_i \frac{\rho_i}{\epsilon_0}$$

which leads to :

$$V_{i-1} \frac{-A_{i-1}}{x_i-x_{i-1}} + V_i \left(\frac{-A_i}{x_{i+1}-x_i} + \frac{A_{i-1}}{x_i-x_{i-1}} \right) + V_{i+1} \frac{-A_i}{x_{i+1}-x_i} = Vol_i \frac{\rho_i}{\epsilon_0}$$

This can be written under the following form:

$$c_i^W V_{i-1} + c_i^C V_i + c_i^E V_{i+1} = Vol_i \frac{\rho_i}{\epsilon_0}$$

with:

$$\text{West coefficient } c_i^W = \frac{-A_{i-1}}{x_i-x_{i-1}}$$

$$\text{East coefficient } c_i^E = \frac{-A_i}{x_{i+1}-x_i} \quad (= c_{i+1}^W)$$

$$\text{Centre coefficient } c_i^C = \frac{-A_i}{x_{i+1}-x_i} + \frac{A_{i-1}}{x_i-x_{i-1}} \quad (= c_i^W - c_i^E)$$

Poisson's equation is equivalent to solving the following system of equations:

$$\begin{pmatrix} c_1^C & c_1^E & 0 & & & \\ c_2^W & c_2^C & c_2^E & 0 & & \\ 0 & . & . & . & 0 & \\ & 0 & . & . & . & 0 \\ & & 0 & c_N^W & c_N^C & c_N^E \\ & & & 0 & c_{N+1}^W & c_{N+1}^C \end{pmatrix} \begin{pmatrix} V_1 \\ V_2 \\ . \\ . \\ V_N \\ V_{N+1} \end{pmatrix} = \begin{pmatrix} \rho_1 \\ \rho_2 \\ . \\ . \\ \rho_N \\ \rho_{N+1} \end{pmatrix}$$

V_1 and V_{N+1} are boundary conditions imposed by the external electrical circuit described in 4.4. The system is solved only from the index 2 to the index N . This matrix inversion is also performed using TRIDAG.

4.3.3 Poisson's equation coupled with the continuity equation

Maxwell time

The time step value Δt is critical when the transport of charged particles is coupled with the variation of the electric field due to those space charges. An explicit coupling gives satisfying results only if Δt is lower than the Maxwell time given by the relation:

$$\forall i, \Delta t \leq \frac{\epsilon_0}{\sum_s |q_s| \mu_{s,i} n_{s,i}} \simeq \frac{\epsilon_0}{e \mu_{e,i} n_{e,i}}$$

It is the maximum time step possible when coupling explicitly the electric field with the transport of electrons. It represents the characteristic time needed by electrons to follow the variations of the electric field when they have collisions with the neutrals².

Coupling Poisson's equation with the continuity equation consists in calculating the transport of particles in a total electric field resulting from their own electric field and the applied electric field. Let us call s the index for charged particles. The potential obeys the following system of equations:

$$\begin{cases} \nabla \cdot (\epsilon_0 \nabla V) = \sum_s q_s n_s & (a) \\ \frac{\partial n_s}{\partial t} + \nabla \cdot (\pm \mu_s n_s \nabla V - D_s \nabla n_s) = S_s & (b) \end{cases} \quad (4.18)$$

The sign \pm in front of the convection term is $+$ for positively charged particles and $-$ for negatively charged particles.

At time t^k , with an explicit coupling the potential is calculated from the densities of step k with 4.18 (a):

$$\nabla \cdot (\epsilon_0 \nabla V^k) = \sum_s q_s n_s^k \quad (4.19)$$

Then, at time $t^{k+1} = t^k + \Delta t$ the transport equation 4.18 (b) is solved in order to describe how the charged particles react to this electric field:

$$\frac{1}{\Delta t} (n_s^{k+1} - n_s^k) + \nabla \cdot (\pm \mu_s n_s^{k+1} \nabla V^{k+1} - D_s \nabla n_s^{k+1}) = S_s^{k+1} \quad (4.20)$$

Then, equation 4.18 (a) is solved again at time t^{k+1} with the new densities and so on.

This explicit coupling imposes to set Δt lower than the Maxwell time (section 4.3.3) which can be an important constraint. The respect of this time step is the most time consuming process in the simulation. The use of a larger time step is possible with the semi-implicit method.

Instead of using n_s^k in equation 4.19 we use n_s^{k+1} which already accounts for the transport to come at next step. This is somehow an “anticipation” of the transport of

² In the absence of collisions, the typical time is the inverse of the plasma frequency.

particles. It allows us to reduce the time step by a large factor. $n_s^{\sim k+1}$ is calculated as follows:

$$\frac{1}{\Delta t}(n_s^{\sim k+1} - n_s^k) + \nabla \cdot (\pm \mu_s n_s^k \nabla V^{k+1} - D_s \nabla n_s^k) = 0$$

This can be rearranged:

$$n_s^{\sim k+1} = n_s^k - \Delta t \nabla \cdot (\pm \mu_s n_s^k \nabla V^{k+1} - D_s \nabla n_s^k)$$

Injecting $n^{\sim k+1}$ into equation 4.19 yields:

$$\begin{aligned} \nabla \cdot (\epsilon_0 \nabla V^{k+1}) &= \sum_s q_s n_s^k - \Delta t \sum_s q_s \nabla \cdot (\pm \mu_s n_s^k \nabla V^{k+1} - D_s \nabla n_s^k) \\ \nabla \cdot \left\{ \left(\epsilon_0 + \Delta t \sum_s |q_s| \mu_s n_s^k \right) \nabla V^{k+1} \right\} &= \sum_s q_s n_s^k + \Delta t \sum_s q_s \nabla \cdot (D_s \nabla n_s^k) \end{aligned} \quad (4.21)$$

Using the local Maxwell time at the position i

$$t_m = \frac{\epsilon_0}{\sum_s |q_s| \mu_s n_s^k}$$

and introducing the two variables:

$$\rho^* = \Delta t \sum_s q_s \nabla \cdot (D_s \nabla n_s^k)$$

and

$$\epsilon^* = \epsilon_0 \left(1 + \frac{\Delta t}{t_m} \right)$$

The semi-implicit system to calculate the electric field and the transport becomes:

$$\begin{cases} \nabla \cdot (\epsilon^* \nabla V^{k+1}) = \sum_s q_s n_s^k + \rho^* & (a) \\ \frac{\partial n_s}{\partial t} + \nabla \cdot (\pm \mu_s n_s \nabla V - D_s \nabla n_s) = S_s & (b) \end{cases} \quad (4.22)$$

Equation 4.22 (a) still has a form similar to the original Poisson's equation only with an extra source of charges and an extra term in the permittivity. It is solved as described in section 4.3.2 with the use of Green-Ostrogradsky's theorem. For equation 4.22 (b) the flux discretization is performed with the exponential scheme as described in section 4.3.1.

4.3.4 Solving the electron energy equation

Heating term

On the RHS of equation 4.11 the heating term $H = -e\mathbf{\Gamma}_e \cdot \mathbf{E}$ has to be evaluated as follows:

$$H_i = \frac{-e}{2} (E_i \Gamma_i + E_{i-1} \Gamma_{i-1})$$

Using $1/2 (E_{i-1} + E_i) \times 1/2 (\Gamma_i + \Gamma_{i-1})$ would introduce the cross terms $E_i \Gamma_{i-1}$ and $E_{i-1} \Gamma_i$, which leads to instabilities.

Electron energy loss in collisions

Given the density of gas particles relative to all other species, the loss of electron energy occurs predominantly during collisions with those particles. For those electron impact reactions with the gas (R1, R2 and R8 in table 4.2) the energy loss coefficient $k_r(\bar{\varepsilon})$, depending on the electron mean energy, is calculated by *BOLSIG+*. The loss rate of reaction r involving electrons and gas particles of density n_g is:

$$R_r(\bar{\varepsilon}) = k_r(\bar{\varepsilon}) n_e n_g$$

Reactions between electrons and Ar^* or Ar_2^+ (R3 and R6 in 4.2 respectively) can be taken into account when the corresponding cross-sections are used in *BOLSIG+*. However, Ar^* and Ar_2^+ densities stay low compared to the gas density and the electron loss of energy in those reactions can be neglected.

The energy threshold required for the reaction r to occur is called ε_r . The electron mass is so small relative to other particles that their velocity is generally conserved after an elastic collision ; only the direction is changed. However, for higher electron energy there can be a loss of energy for the electron after an elastic collision. This energy is transferred to the neutral atoms³. In *BOLSIG+* the elastic collisions are included in the loss term with $\varepsilon_r = 1$ and with an effective rate coefficient.

The total energy loss term of equation 4.11 is:

$$P(\bar{\varepsilon}) = \sum_r \varepsilon_r R_r(\bar{\varepsilon}) = n_e n_g \sum_r \varepsilon_r k_r(\bar{\varepsilon}) = n_e n_g K(\bar{\varepsilon}) \quad (4.23)$$

with $K(\bar{\varepsilon}) = \sum_r \varepsilon_r k_r(\bar{\varepsilon})$

As this loss of energy $P(\bar{\varepsilon})$ depends on the energy itself, it is treated implicitly to prevent the instabilities. Let us call $P^k = P(\bar{\varepsilon}^k)$.

In order to find the “anticipated” value $P^{\sim k+1}$ knowing the table that relates P to $\bar{\varepsilon}$, $P(\bar{\varepsilon})$ is linearised with respect to the energy as describe in Hagelaar (2000):

$$P^{\sim k+1} = P^k + \frac{\partial P}{\partial \bar{\varepsilon}} (\bar{\varepsilon}^{k+1} - \bar{\varepsilon}^k) \quad (4.24)$$

³ The energy gained by heavy particles in elastic collisions is ignored.

Hence, the energy equation 4.11 is temporally discretized as the continuity equation for particles 4.2 paying particular attention to the source term:

$$\begin{aligned} \frac{n_\varepsilon^{k+1} - n_\varepsilon^k}{\Delta t} + \nabla \cdot \mathbf{\Gamma}_\varepsilon^k &= H^k - P^{\sim k+1} \\ \frac{n_\varepsilon^{k+1} - n_\varepsilon^k}{\Delta t} + \nabla \cdot \mathbf{\Gamma}_\varepsilon^k &= H^k - P^k - \frac{\partial P}{\partial \bar{\varepsilon}} (\bar{\varepsilon}^{k+1} - \bar{\varepsilon}^k) \end{aligned} \quad (4.25)$$

The variation of mean energy is linearised with $\bar{\varepsilon}^k = n_\varepsilon^k / n_e^k$

$$\begin{aligned} \bar{\varepsilon}^{k+1} - \bar{\varepsilon}^k &= \left. \frac{\partial \bar{\varepsilon}}{\partial n_\varepsilon} \right|^k (n_\varepsilon^{k+1} - n_\varepsilon^k) + \left. \frac{\partial \bar{\varepsilon}}{\partial n_e} \right|^k (n_e^{k+1} - n_e^k) \\ \bar{\varepsilon}^{k+1} - \bar{\varepsilon}^k &= \frac{1}{n_e^k} (n_\varepsilon^{k+1} - n_\varepsilon^k) - \frac{n_\varepsilon^k}{(n_e^k)^2} (n_e^{k+1} - n_e^k) \\ \bar{\varepsilon}^{k+1} - \bar{\varepsilon}^k &= \frac{1}{n_e^k} (n_\varepsilon^{k+1} - n_e^{k+1} \bar{\varepsilon}^k) \end{aligned} \quad (4.26)$$

n_e^{k+1} is known since we solve the transport of electrons before the transport of their mean energy.

Combining equation 4.26 with equation 4.25 yields:

$$\frac{n_\varepsilon^{k+1} - n_\varepsilon^k}{\Delta t} + \nabla \cdot \mathbf{\Gamma}_\varepsilon^k = H^k - P^k - \frac{\partial P}{\partial \bar{\varepsilon}} \frac{1}{n_e^k} (n_\varepsilon^{k+1} - n_e^{k+1} \bar{\varepsilon}^k)$$

Using the expression of the loss term found in equation 4.23 leads to:

$$\frac{n_\varepsilon^{k+1} - n_\varepsilon^k}{\Delta t} + \nabla \cdot \mathbf{\Gamma}_\varepsilon^k = H^k - K(\bar{\varepsilon}) n_g \frac{n_e^k}{n_e} - \frac{\partial K}{\partial \bar{\varepsilon}} n_g (n_\varepsilon^{k+1} - n_e^{k+1} \bar{\varepsilon}^k)$$

Separating terms of time step k and $k+1$ yields:

$$n_\varepsilon^{k+1} \left(\frac{1}{\Delta t} + \frac{\partial K}{\partial \bar{\varepsilon}} n_g \right) + \nabla \cdot \mathbf{\Gamma}_\varepsilon^k = H^k - K(\bar{\varepsilon}) n_g \frac{n_e^k}{n_e} - \frac{\partial K}{\partial \bar{\varepsilon}} n_g n_e^{k+1} \bar{\varepsilon}^k + \frac{n_\varepsilon^k}{\Delta t}$$

The derivative term $\frac{\partial K}{\partial \bar{\varepsilon}}$ is simply obtained from the tabulation of K as a function of $\bar{\varepsilon}$ given in *BOLSIG+*. This continuity equation for energy is solved as the continuity equation for other particles (section 4.3.1). The energy flux is discretized with the exponential scheme.

4.4 Applied Voltage, external circuit

The voltage applied on the left electrode V_1 is a boundary condition for Poisson's equation. We apply a Radio Frequency sinusoidal voltage such as $V_1^k = A \sin(f k \Delta t + \varphi)$. The right electrode is grounded so $V_{N+1} = 0$.

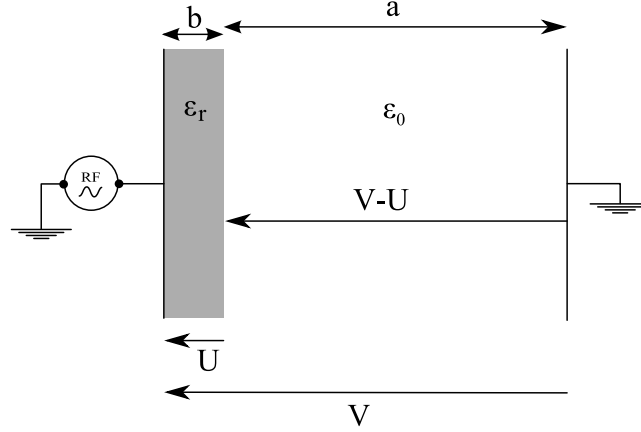


Figure 4.2: Dielectric layer in the external circuit

4.4.1 Dielectric layer

For the dielectric to be taken into account in the model, the conduction current and displacement current densities are calculated. Let U be the voltage across the dielectric layer, and V is the applied voltage, then the boundary condition for the potential in Poisson's equation is no longer V but $V - U$ as shown in figure 4.2.

Let C_s be the capacitance per surface unit of the solid dielectric and C_g the capacitance per surface unit of the gas gap. At $t = 0$ when an external voltage is applied but no electron multiplication occurs:

$$C_s U^0 = C_g (V^0 - U^0)$$

where $C_s = \epsilon_0 \epsilon_r / b$ and $C_g = \epsilon_0 / a$ and ϵ_r is the relative permittivity of the dielectric material. Hence the initial relation between the voltage across the dielectric layer and the applied voltage is:

$$U^0 \epsilon_0 \left(\frac{\epsilon_r}{b} + \frac{1}{a} \right) = V^0 \frac{\epsilon_0}{a}$$

which can be rearranged as follows:

$$U^0 = \frac{V^0}{1 + \epsilon_r \frac{a}{b}}$$

When charged particles start to multiply in the gas gap (when the gas is becoming a conductor) some of them will be deposited on the dielectric surface. This will increase the voltage across the dielectric layer and reduce the voltage across the gas gap.

From Kirchhoff law (conservation of charge), the displacement current in the dielectric layer (no conduction current in the dielectric) is equal to the total current in the

gas gap. It is given by:

$$J = C_s \frac{\partial U}{\partial t} \quad (4.27)$$

The total current in the gas gap at a given time is constant in space and is therefore equal to its own average. It contains a displacement current J_d and a conduction current J_c due to the fluxes of charged particles:

$$J = \langle J_d(x) + J_c(x) \rangle = \frac{1}{a} \int_0^a (J_d(x) + J_c(x)) dx$$

$$J = C_g \frac{\partial}{\partial t} (V - U) + \frac{1}{a} \int_0^a \sum_s q_s \Gamma_s dx \quad (4.28)$$

Combining equations 4.27 and 4.28 yields:

$$\frac{\epsilon_0 \epsilon_r}{b} \frac{\partial U}{\partial t} = \frac{\epsilon_0}{a} \frac{\partial}{\partial t} (V - U) + \frac{1}{a} \int_0^a \sum_s q_s \Gamma_s dx$$

$$\frac{\partial U}{\partial t} \epsilon_0 \left(\frac{\epsilon_r}{b} + \frac{1}{a} \right) = \frac{\epsilon_0}{a} \frac{\partial V}{\partial t} + \frac{1}{a} \int_0^a \sum_s q_s \Gamma_s dx$$

$$\frac{\partial U}{\partial t} = \frac{1}{\epsilon_r \frac{a}{b} + 1} \frac{\partial V}{\partial t} + \frac{1/\epsilon_0}{\epsilon_r \frac{a}{b} + 1} \int_0^a \sum_s q_s \Gamma_s dx$$

This equation is solved numerically as follows:

$$U^k = U^{k-1} + \frac{1}{\epsilon_r \frac{a}{b} + 1} (V^k - V^{k-1}) + \frac{\Delta t / \epsilon_0}{\epsilon_r \frac{a}{b} + 1} \int_0^a \sum_s q_s \Gamma_s dx$$

4.4.2 Serial resistor

Experimentally, the voltage drops immediately after the breakdown has occurred because the RF power supply is not an ideal voltage source (chapter 2). The generator can not deliver a constant voltage when the current increases. To simulate this external circuit behaviour, a serial resistor⁴ R is added between the discharge gap and the RF power supply as shown on figure 4.3. This also contributes to the stability of the model. For a large product pressure·distance the breakdown voltage is high and if it stays constant after the breakdown, the model rapidly diverges.

The voltage across the resistor is calculated from the total current density J in the gap which is the sum of the displacement current and the conduction current $J = J_d + J_c$.

⁴ This resistor can be used with or without the dielectric layer.

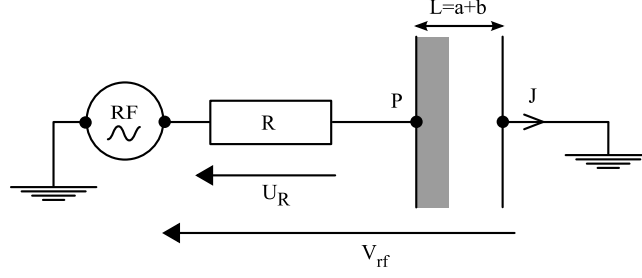


Figure 4.3: Resistor in the external circuit

The equivalent permittivity of the gas gap with the dielectric of thickness b is:

$$\epsilon_{eq} = \frac{a + b}{b/\epsilon_r\epsilon_0 + a/\epsilon_0}$$

Let us call P the potential applied on the left electrode and $L = a + b$ the distance between the electrodes. The displacement current in the gap is:

$$J_d = \frac{\epsilon_{eq}}{L} \frac{\partial P}{\partial t} \quad (4.29)$$

R has the dimension $\Omega.m^2$ and the current density J is in A/m^2 so that the product $R.J$ is in Volts. Using equation 4.29 with Ohm's law yields:

$$U_R = R(J_c + J_d) = R J_c + \frac{\epsilon_{eq} R}{L} \frac{\partial P}{\partial t}$$

Which is discretized as follows:

$$U_R^k = R J_c^k + \frac{\epsilon_{eq} R}{L \Delta t} (P^{k+1} - P^k)$$

Hence, the numerical system is:

$$\begin{cases} U_R^k = V_{rf}^k - P^k & (a) \\ P^{k+1} = P^k + (U_R^k - R J_c^k) \frac{L \Delta t}{\epsilon_{eq} R} & (b) \end{cases} \quad (4.30)$$

Before the breakdown occurs, the total current is mostly the displacement current due to the oscillating RF voltage. A direct coupling leads to numerical instabilities. A classical semi implicit coupling is required. In equation 4.30 (a) P^k is replaced by its “anticipated” value $P^{\sim k+1}$ which already takes into account the variations of P due to the displacement current in the gap.

$$P^{\sim k+1} = P^k + U_R^k \frac{L \Delta t}{\epsilon_{eq} R}$$

Injecting P^{k+1} in equation 4.30 (a) yields:

$$U_R^k = V_{rf}^k - P^k - U_R^k \frac{L \Delta t}{\epsilon_{eq} R}$$

And the implicit system is:

$$\begin{cases} U_R^k = (V_{rf}^k - P^k) / (1 + \frac{L \Delta t}{\epsilon_{eq} R}) \\ P^{k+1} = P^k + (U_R^k - R J_c^k) \frac{L \Delta t}{\epsilon_{eq} R} \end{cases}$$

4.5 Argon kinetics

The behaviour of the atmospheric discharge is mainly determined by reactions involving electrons. The model is applied to pure argon with the reaction scheme of table 4.2. It accounts for the main ionization (direct and stepwise), excitation and conversion processes. The recombination reaction by attachment of an electron on an ion $e + Ar^+ \rightarrow Ar$ is very unlikely to happen as it creates only one atomic particle that should balance both the momentum and the kinetic energy. Therefore it is purposely omitted in this scheme. The dissociative recombination $R6$ is much more probable.

Excited atoms of the $4s$ system are treated as a single compound state Ar^* . It groups the resonant and metastable states of argon. The decay frequencies of the transitions from the $4s$ resonant states is relatively high ($5.1 \times 10^8 \text{ s}^{-1}$ and $1.19 \times 10^8 \text{ s}^{-1}$ according to [NIST](#)). On the other hand, the metastable state which can not satisfy the quantum rules for electric dipole radiation has a much longer lifetime⁵. However, since the energy of metastable and resonant states are very close together there is a large probability for a metastable to turn into a resonant and for a resonant to turn into metastable by electron collisions. Therefore we assume that they are in Boltzmann equilibrium with the electron temperature and we assign to the compound state an average decay frequency accounting for radiation trapping as described in [Ferreira et al. 1985](#). The diffusion coefficient for Ar^* is found [Grigoriev et al. 1997](#), the mobility of Ar^+ and Ar_2^+ ions are found in [Ellis et al. 1976](#).

⁵ Metastable states have no possible radiative decay so they can be transformed only by collisions.

	Reaction	Rate coefficient	Reference
R1	$e + Ar \rightarrow 2e + Ar^+$	<i>BOLSIG+</i>	Hagelaar 2005
R2	$e + Ar \rightarrow e + Ar^*$	<i>BOLSIG+</i>	Hagelaar 2005
R3	$e + Ar^* \rightarrow 2e + Ar^+$	<i>BOLSIG+</i>	Hagelaar 2005
R4	$2Ar^* \rightarrow e + Ar^+ + Ar$	$1.2 \times 10^{-9} (300K/T)^{1/2} cm^3 s^{-1}$	Karoulina 1992
R5	$Ar^+ + 2Ar \rightarrow Ar_2^+ + Ar$	$2.5 \times 10^{-31} (300K/T)^{3/2} cm^6 s^{-1}$	Lam 2000
R6	$e + Ar_2^+ \rightarrow Ar^* + Ar$	$7 \times 10^{-7} (300K/T_e)^{1/2} cm^3 s^{-1}$	Min 2000
R7	$Ar^* \rightarrow Ar + h\nu$	$5 \times 10^5 s^{-1}$	Ferreira 1985
R8	$e + Ar \rightarrow e + Ar$	<i>BOLSIG+</i>	Hagelaar 2005

Table 4.2: Rate coefficients of reactions

Chapter 5

Simulation results

5.1 RF breakdown

In this chapter we present and analyse the results of simulations based on the numerical model described in chapter 4. The experimental measurements described in chapter 2 and chapter 3 corroborate the model. The calculated current densities, particle densities and temperature are in satisfying agreement with measurements performed on the glow mode. The model is written in Fortran and runs on a 2 GHz PC processor. For a typical time step of $10^{-10}s$ a period of 100 μs is simulated in an acceptable time (less than one hour). This is certainly one of the main advantages of the fluid approach over Particle In Cells (PIC) models.

Before starting a full self-consistent plasma simulation, some preliminary verifications are necessary. The flux discretization obtained with the exponential scheme discussed in section 4.3.1 introduces numerical diffusion. For a given type of particle, this numerical artefact depends on the drift velocity and on the size of the mesh. With a typical linear mesh made of more than one hundred cells for a 2 mm gap at atmospheric pressure, this numerical artefact is not significant. Increasing the mesh size over 200 cells does not change the simulation results. In order to keep the numerical diffusion negligible the number of cells is set to 200.

The minimum size of the mesh is also imposed by the dimensions of the sheath. There must be a sufficient number of cells in this region of the plasma where large density gradients and strong electric field variations take place. Both non-linear and linear meshes have been tested. The non-linear mesh does not improve the results significantly in terms of time efficiency or low numerical diffusion. All the following results were obtained with a linear mesh made of 200 cells unless specified otherwise.

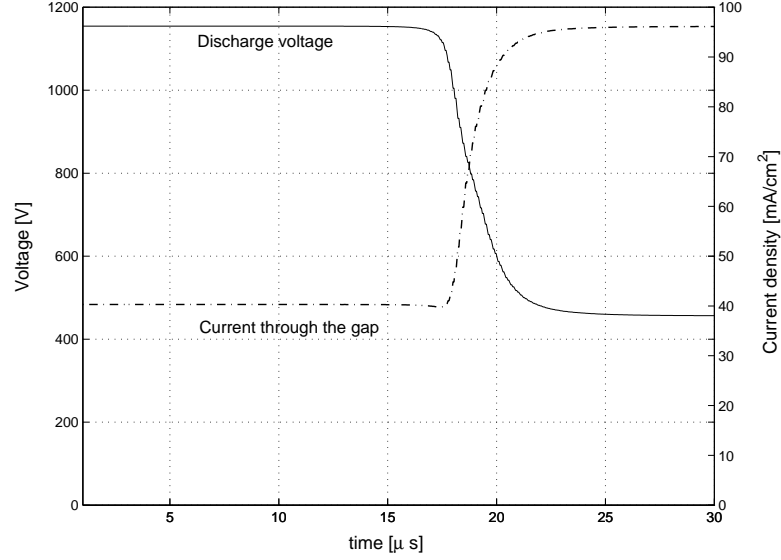


Figure 5.1: Evolution of the peak current density through the discharge and peak voltage applied to the left electrode

5.1.1 Breakdown voltage - Sustain voltage

The minimum RF voltage from the power supply required to create a plasma is approximately 1200 V for a 2 mm gap and once the discharge is set it can be sustained with a much lower voltage of the order of one hundred of volts.

Due to the external resistor and dielectric components described in section 4.4, the potential applied to the left electrode is smaller than the RF voltage delivered by the power supply. Until the breakdown occurs, the current is mostly the displacement current due to the oscillations of the RF electric field as shown in figure 5.14. It remains relatively low compared to the conduction current after the breakdown. After the breakdown, a large conduction current passes through the gap and is added to the displacement current. This increase of the total discharge current results in a rise of the voltage across the dielectric layer and across the resistor. Hence the voltage across the plasma is reduced by a factor of nearly two. The evolution of the voltage applied to the left electrode and of the total current density is shown in figure 5.1. The breakdown clearly occurs after 25 μs . For an applied voltage of 1200 V, the initial displacement current is 42 mA/cm² (peak value) and after the breakdown the total current stays constant at 96 mA/cm².

The voltage applied to the left electrode creates a uniform electric field across the gap until the space charge created by charged particles of the plasma is high enough to modify the distribution of the electric field. The space resolved variation of the plasma potential is shown in figure 5.2. The potential on the right electrode is constant at 0 V.

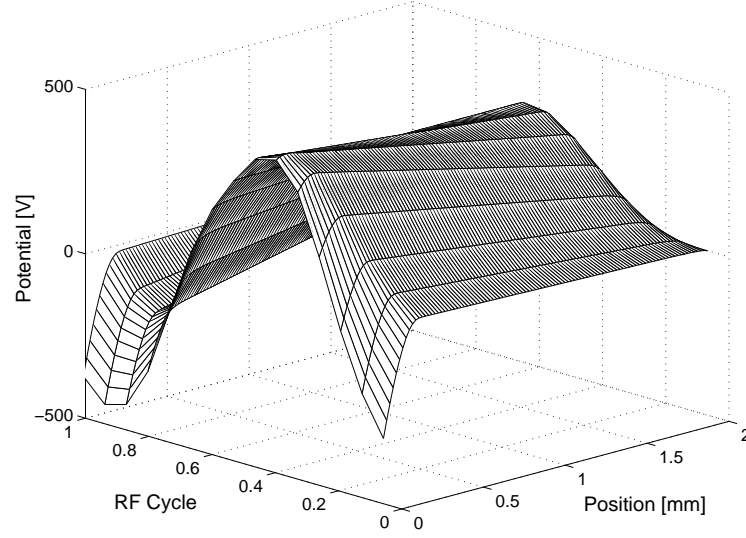


Figure 5.2: Potential in the gap after the breakdown

The potential distribution in the gap is typical of an RF discharge running at lower pressure as described in [Raizer et al. \(1995\)](#).

5.1.2 Ion trapping

In atmospheric pressure capacitive discharges running in the kHz range, the secondary emission is the dominant mechanism of electron creation. When the secondary emission of electrons at the cathode is too low, the breakdown can not occur. In the present RF discharge a plasma can be created even without secondary emission. The direct and stepwise ionizations are sufficient to ignite and sustain the discharge because the electrons are efficiently confined by the field oscillations.

In classical atmospheric DBDs running at some tens of kHz , the slow ions can follow the variations of the electric field. When the threshold voltage is reached during a cycle of the periodic applied signal, the breakdown occurs. This happens only if the rising time of the applied voltage is slow enough for the ions to travel from one side of the gap to the other and create secondary electrons at the cathode. When the polarity is reversed another breakdown occurs with secondary emissions from the other electrode. This kind of plasma excitation is similar to a DC pulse discharge for which the plasma is successively turned ON and OFF.

In contrast, with the fast variations of the RF electric field in the present experiment, the plasma is not turned OFF between successive RF cycles as seen in figures [5.5](#), [5.6](#), [5.7](#), [5.8](#) and [5.9](#). There is a flux of atomic ions and molecular ions towards the walls but

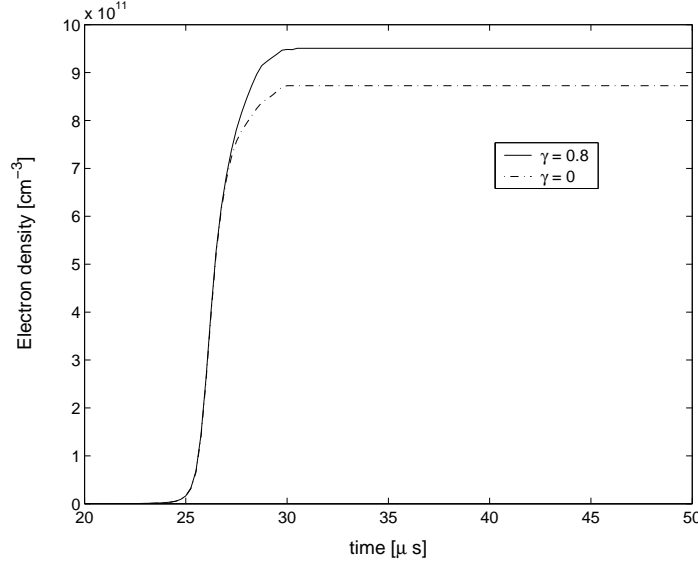


Figure 5.3: Breakdown for two values of the secondary emission coefficient

their distributions are steady in the gap.

The secondary emission of electrons does not have a great influence on the number of RF cycles required to reach the breakdown. In figure 5.3 two breakdown curves are shown for two values of the secondary emission coefficient γ (a common value is set for all heavy particles). The final plasma densities are of the same order even with large variations of the secondary emission coefficient. For all the heavy particles γ is set to 0.1 which is near the upper limit of values usually found in literature.

5.2 Particle density

5.2.1 Initial density

When the initial particle densities chosen in the model are lower than the threshold value to create a plasma from the initial space charge, no effect of the initial densities on the stationary state of the plasma is observed. Increasing the initial densities only shortens the time needed to create the plasma but does not affect the final stationary state. The electron density depends moderately on the applied voltage as detailed in section 5.6. All the simulation results are obtained for an applied voltage of 1400 V and a 2 mm wide gap unless specified otherwise.

In figure 5.4, two breakdown curves show the rise of the electron density. The first curve is obtained for an initial particle density of 10^6 cm^{-3} and the second is obtained for a lower initial density of 10^4 cm^{-3} . In both cases the final densities are identical. In order to reduce the simulation time, it is desirable to start with elevated initial densities.

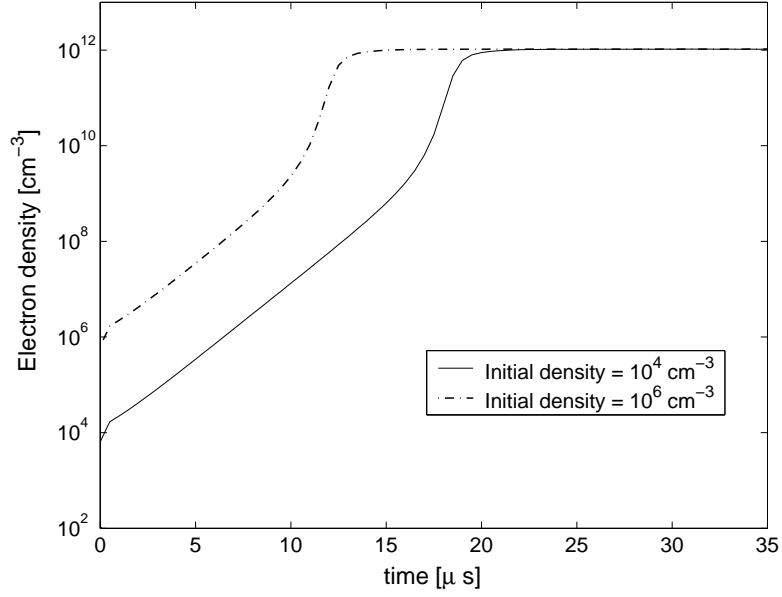


Figure 5.4: Breakdown for different values of the initial densities

However, the space charge created by the initial densities has to be low enough to avoid a breakdown that would only be due to the initial densities. The chosen initial densities are around 10^4 cm^{-3} with a parabolic distribution over the gap. This is sufficiently low to avoid any unrealistic breakdown in our conditions.

5.2.2 Spatial distribution

The density of electrons, ions and metastable atoms averaged over one RF cycle are represented in figure 5.5. Oscillating sheaths (approximately 0.3 mm wide) are produced by swinging electrons which leave a space charge layer near the electrodes at each RF cycle. Apart from these two regions, the plasma is neutral over most of the discharge gap.

The potential drop in the sheath region is represented in figure 5.2. The electric field is almost constant in the bulk of the plasma and it oscillates with a much greater amplitude in each sheath. In the bulk of the plasma the quasi-neutrality is respected and mainly assured by the balance between the electron density and the molecular ion Ar_2^+ density both approximately 10^{12} cm^{-3} . The space-time averaged electron density is about $8 \times 10^{11} \text{ cm}^{-3}$ which is in reasonable agreement with experimental data of section 3.2.2 where a first approximation of $5 \times 10^{11} \text{ cm}^{-3}$ was obtained.

The metastable atoms Ar^* density is around 10^{13} cm^{-3} with maxima near the sheath regions where electrons are more energetic. The atomic ion Ar^+ density is two orders of magnitude lower than the electron density, around $5 \times 10^9 \text{ cm}^{-3}$. This is mainly due to the large contribution of the reaction $\text{Ar}^+ + 2\text{Ar} \rightarrow \text{Ar}_2^+ + \text{Ar}$ which occurs at an impor-

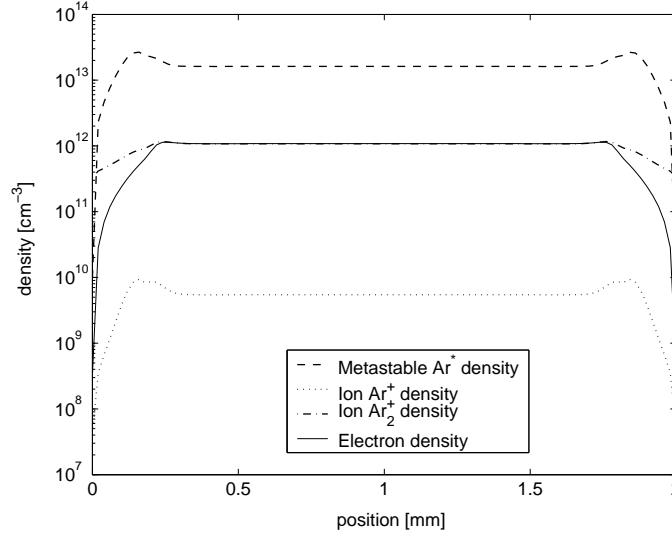


Figure 5.5: Densities averaged over one RF period

tant rate thus creating a lot of molecular ions and reducing the atomic ion population. In the sheaths, the Ar^+ density is slightly higher because of the stepwise ionization which creates ions from the numerous metastable atoms present in this region. The relative contribution of all reactions to the loss and creation of particles is detailed in section 5.5.

The spatio-temporal profile of the electron density is shown in figure 5.6. Electrons oscillate from one side of the gap to the other as the RF electric field oscillates. These results agree with the experimental measurements of previous sections and with results from other groups. In their experimental results, [Park et al. \(2001\)](#) reported an electron density of $3 \times 10^{11} \text{ cm}^{-3}$ for an RF capacitive discharge running at atmospheric pressure and fed with argon. It also agrees with other simulation results of [Oda et al. \(2006\)](#) also using a fluid model applied to a CCP argon source.

The distribution of heavy molecular ions is not affected by RF oscillations. As shown in figure 5.7, their density remains steady regardless of the RF electric field variations.

The spatio-temporal profile of Ar^* is shown in figure 5.8. Their elevated density (10^{13} cm^{-3}) concurs with previous results for atmospheric pressure argon discharges. [Penache et al. \(2002\)](#) and [Penache \(2002\)](#) found a similar value for atmospheric argon micro discharges. Similar metastable densities have also been obtained in simulations by [Shi and Kong \(2004\)](#) for helium. At lower pressure, the metastable atoms density is also high relative to the charged particles densities as reported in [Lymberopoulos \(1993\)](#) and in [Lymberopoulos and Economou \(1993\)](#) who using a 2D fluid model to simulate an argon RF discharge.

The atomic ions Ar^+ evolution is shown in figure 5.9. Unlike the molecular ions,

the atomic ion density is slightly modulated by the RF oscillations. This does not perturb the quasi-neutrality as the Ar^+ density is 200 times lower than the electron density.

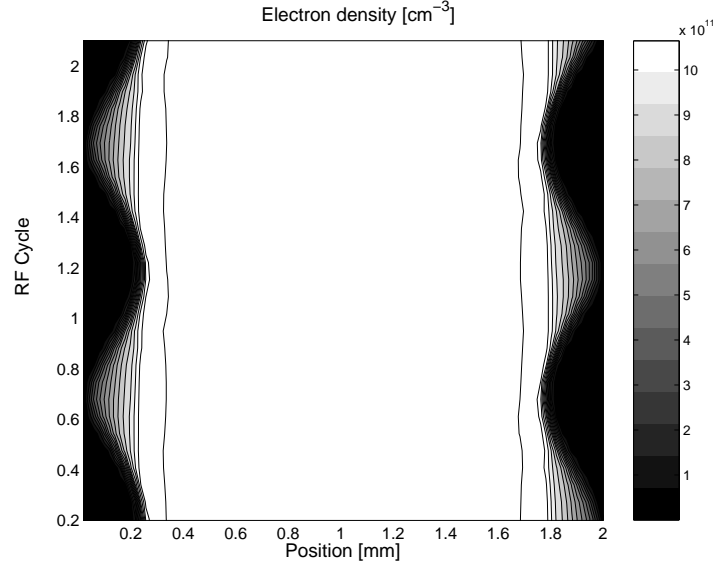


Figure 5.6: Evolution of the electron density

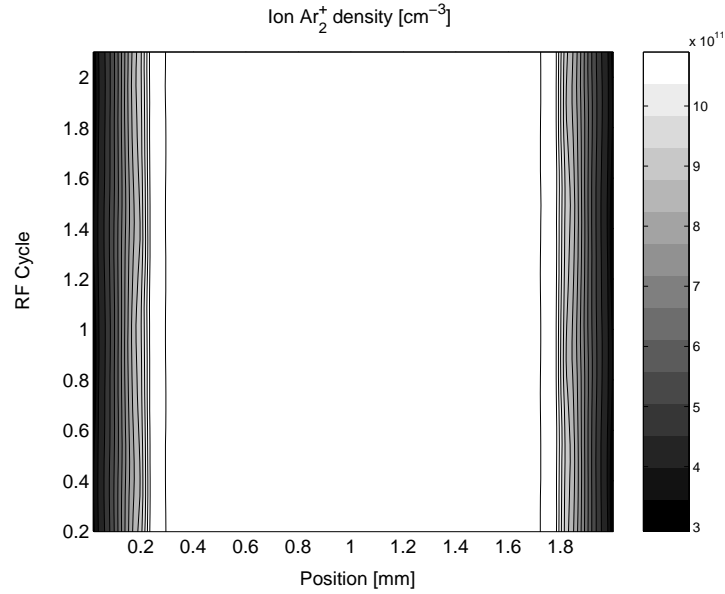


Figure 5.7: Evolution of molecular ions Ar_2^+ density

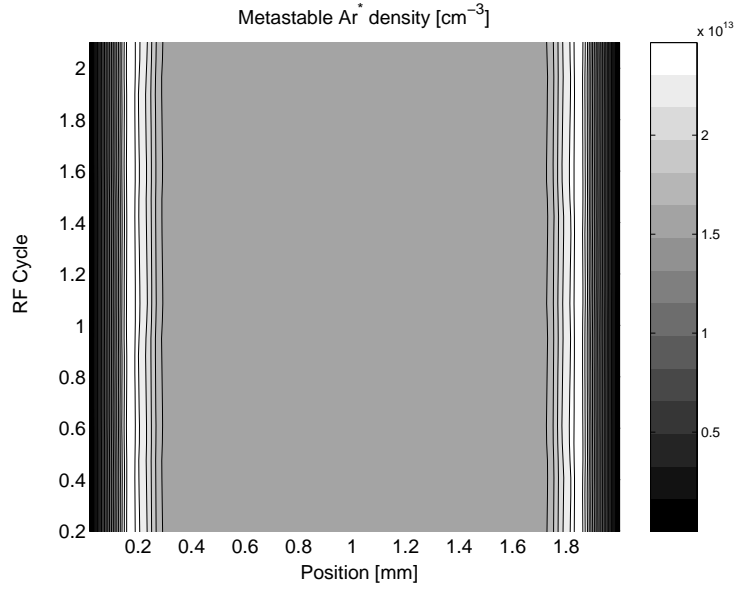


Figure 5.8: Evolution of metastable atoms Ar^* density

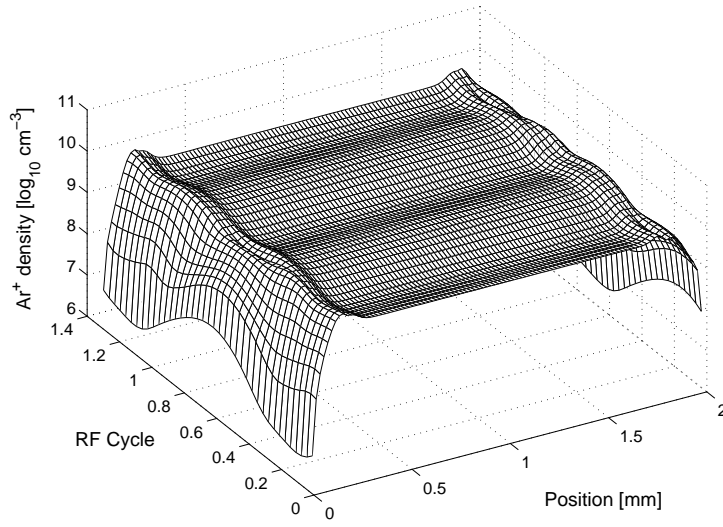


Figure 5.9: Evolution of atomic ions Ar^+ density

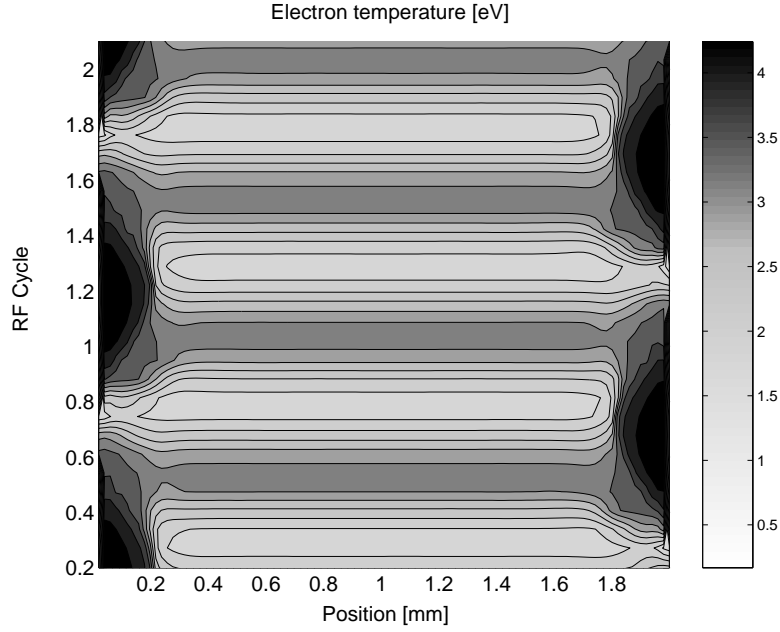


Figure 5.10: Evolution of the electron temperature

5.3 Electron temperature

The electron temperature in eV is obtained from the electron mean energy $kT_e = 2/3 \bar{\epsilon}$. The corresponding spatio-temporal profile is shown in figure 5.10. The electron temperature averaged in space and time is approximately $2.5 eV$. This result is about $1 eV$ higher than the experimental measurement of section 3.3. This difference is probably due to the uncertainties in the measurement as well as in the fluid model. However, the electron temperature found with the present model agrees with other simulation results running in similar conditions of pressure and frequency (Oda et al., 2006).

Electrons are much more energetic in the sheath region where they are accelerated by the potential drop. On each electrode the electron temperature reaches $4 eV$ for approximately half an RF cycle. In the bulk of the plasma which is $1.6 mm$ in length, the temperature is two times lower, around $2 eV$, and oscillates with the plasma potential represented in figure 5.2.

The heating and energy loss averaged over one RF cycle are represented in figure 5.11. The heating term $-e\Gamma_e \cdot \mathbf{E}$ is high in the bulk where the electron flux is important. The maximum observed at the beginning of the sheath is caused by the high value of the electric field in this region. The loss of electron energy occurs mainly in ionization and excitation reactions and by elastic collisions (reactions R1, R2 and R8 respectively in table 4.2). This loss is high in the bulk of the plasma and near the edge of the sheath

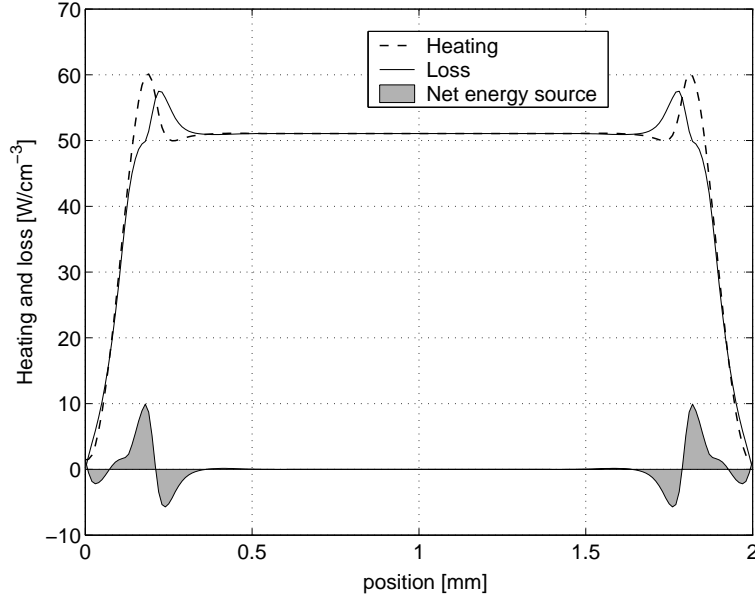


Figure 5.11: Heating and energy loss averaged over one RF period

where the electron mean energy density ($n_\epsilon = \bar{\epsilon} n_e$) is high. The energy production and loss compensate each other in the bulk. When the stationary state is reached the total source of energy (grey area in figure 5.11) integrated over the gap represents the loss of energy to the walls. The grey regions indicates a departure from local field approximation. The negative region in the vicinity of the wall is due to the time averaged representation of the energy source that sums the cathode and anode phase of each electrode. Further away from the electrode the heating dominates the energy loss because electrons gain energy in this region of high electric field. The energy gained in the sheaths is released in the bulk of the plasma as it would be at the cathode of a DC discharge. The time resolved evolution of the energy source is shown in figure 5.12. The loss of energy dominates the heating when the voltage decreases. In the steady state the energy source averaged over one RF cycle is due to the loss of energy to the walls.

5.4 Conduction current and displacement current

The evolution of the current densities (peak value averaged in space) is shown in figure 5.13. The peak value is related to the time average of the absolute value (in figure 5.14) by a ratio of $2/\pi$. After the breakdown the discharge current is mostly the conduction current due to particle fluxes (see figure 5.16). The total current density after the breakdown is around 96 mA/cm^2 (space averaged peak value) with a conduction current density of 85 mA/cm^2 and a displacement current density of 20 mA/cm^2 . Due to the phase shift between the conduction and the displacement current (see figure 5.15), the

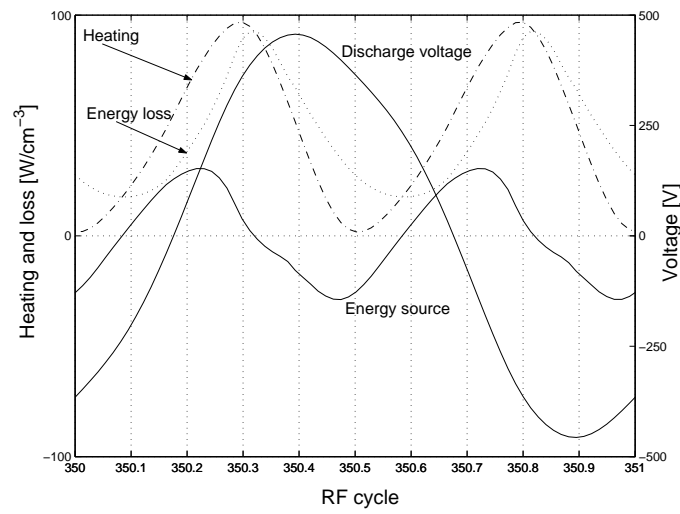


Figure 5.12: Heating and energy loss averaged over the gap

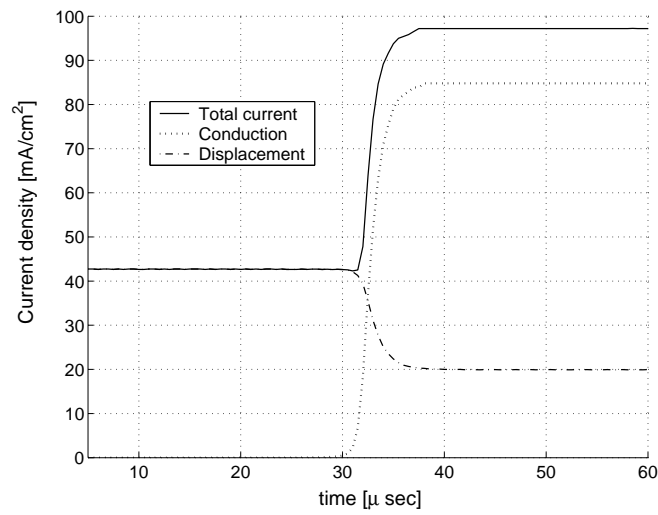


Figure 5.13: Evolution of the current densities averaged over the gap

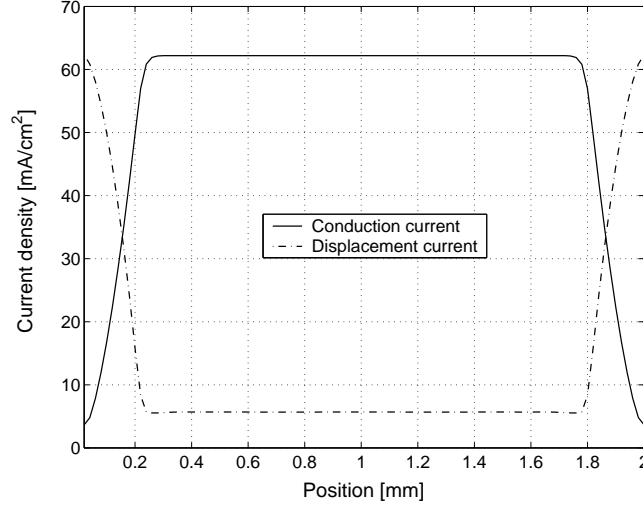


Figure 5.14: Distribution of the current averaged over one RF period

total peak current is not the sum of the conduction and displacement currents.

In figure 5.14 the spatial distribution of the conduction current and the displacement current are represented (average in time of the absolute value). They are both constant in the bulk of the plasma. In this region, which covers most of the discharge gap, the current is mostly due to the particle flux and the conduction current is nearly 7 times higher than the displacement current. Therefore most of the total discharge current is the conduction current (as seen in figure 5.13).

A comparison between the current before and after the breakdown is shown in figure 5.15. For the conduction current and the displacement current, which are not constant in space, the curves represent the peak value averaged over the gap length.

Before the breakdown, figure 5.15 (a), the displacement current dominates. The phase shift between the discharge voltage and the total current is $\pi/2$ as the gas gap simply acts as a capacitive component.

After the breakdown, figure 5.15 (b), the contribution of the displacement current is much smaller. However, in the sheath its contribution is still high as shown in figure 5.14. The value of total current 7.5 A (with the electrode area = 78.5 cm^2) for a discharge voltage of 430 V fits with experimental data. The phase angle of 0.35π between the current leading the voltage also agrees with experimental results of section 3.1. Further investigation is carried out with the model ; for instance the spatial distribution of displacement current or the contribution of each charged particle to the conduction current is not directly measurable. As seen in figure 5.16, most of the conduction current is due to the electron flux in the bulk. The flux of molecular ions only plays a minor role and the atomic ions flux is completely negligible in the conduction current.

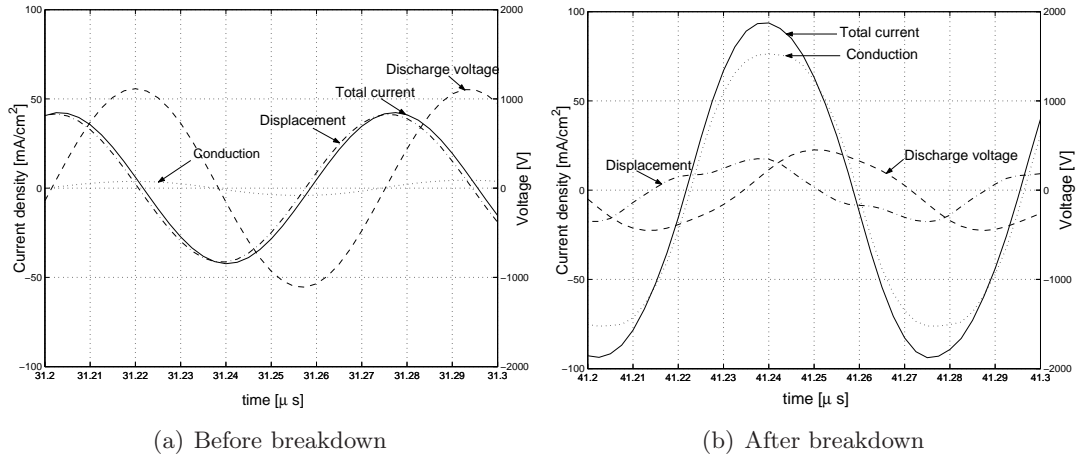


Figure 5.15: Evolution of the current densities averaged over the gap

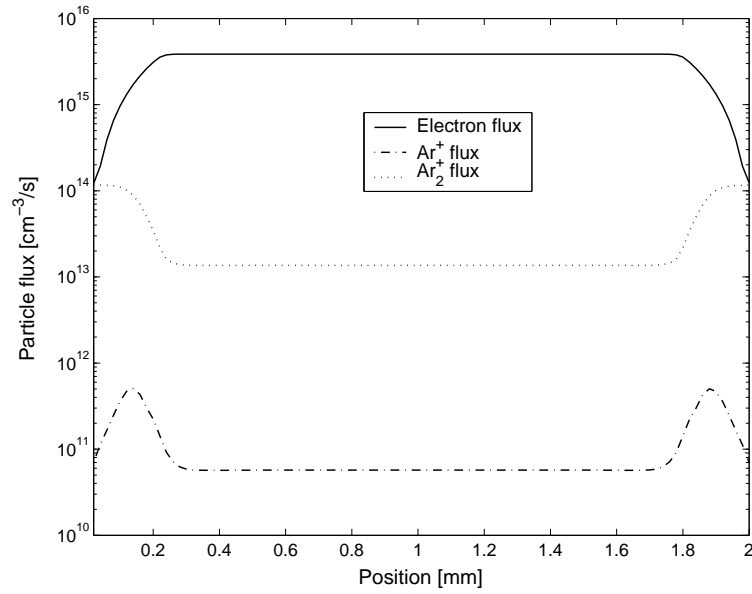


Figure 5.16: Charged particle flux averaged over one RF period

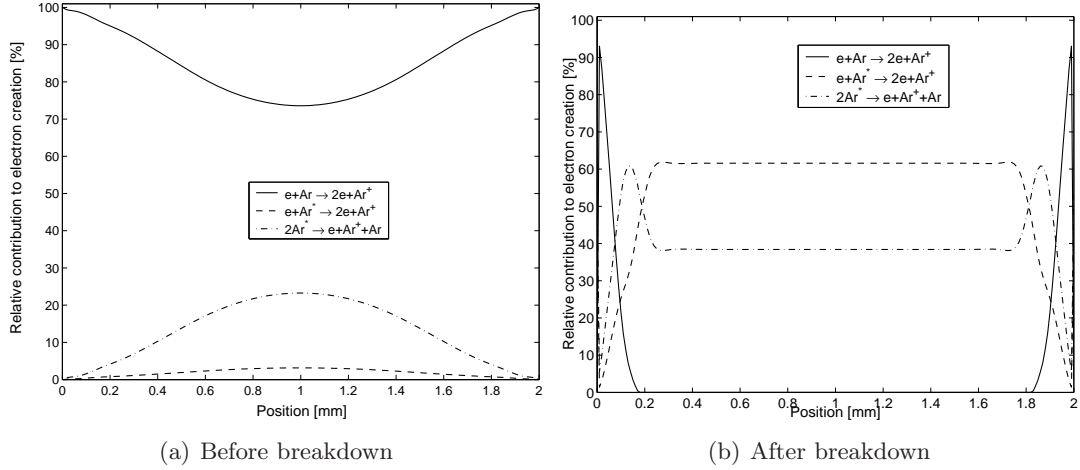


Figure 5.17: Relative contribution to electron creation averaged over one RF period

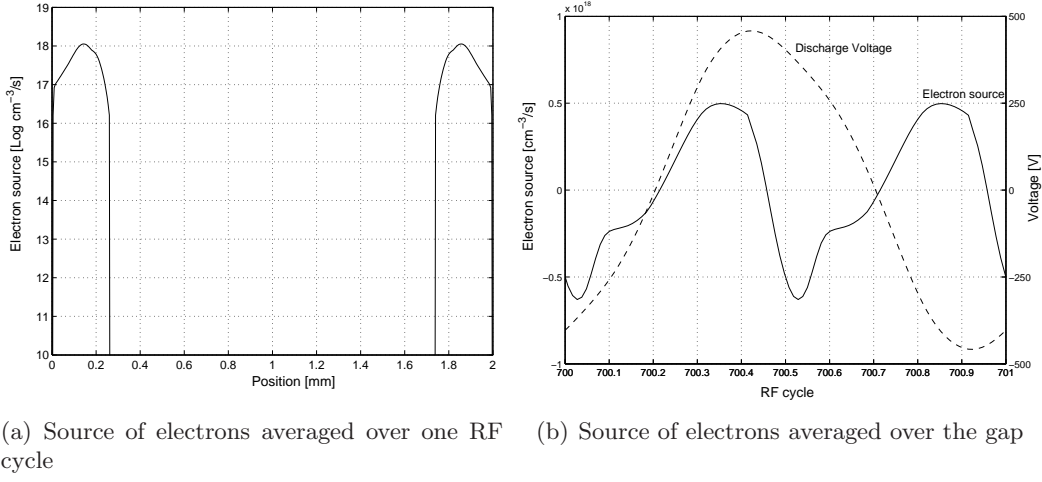
5.5 Contribution of reactions

The analysis of the electron source provides information on the processes that sustain the plasma in the steady state. For each reaction, the relative spatial contribution to electron creation is shown before breakdown in figure 5.17 (a) and after breakdown (b).

Before the breakdown the multiplication of electrons occurs mainly by direct ionization. Before the plasma potential is built up, the oscillating electric field drags all the electrons backwards and forwards in the gap so that ionization is efficient over most of the distance that separates the electrodes. The creation of electrons from metastable atoms is important only in the bulk of the plasma but does not exceed 30% of the total electron creation. The oscillation of electrons in the gap creates metastable atoms that subsequently contribute to electron production via chemical ionization ($2Ar^* \rightarrow e + Ar^+ + Ar$). Less significantly, these metastable atoms also contribute to the creation of electrons by stepwise ionization ($e + Ar^* \rightarrow 2e + Ar^+$). At the surface of the electrodes, in the absence of sheaths repelling the electrons, the secondary emission is negligible compared to the flux towards the walls. The loss by dissociative recombination ($Ar_2^+ + e \rightarrow Ar^* + Ar$) is also negligible so that electrons are only lost at the walls.

After the breakdown the electric field in the middle of the gap is much smaller so other reactions are involved in the electron production as seen in figure 5.17 (b). The loss at the walls exceeds the secondary emission and plays an important role ($\simeq 17.6\%$) in the total electron loss.

In the sheath the direct ionization dominates in the vicinity of the electrodes. Further from the electrode surface the chemical ionization takes over and represents 60% of the electron creation. This is due to the considerable density of metastable atoms created

**Figure 5.18:** Total source of electrons

by excitation in this region (see figure 5.5). The stepwise ionization also contributes to the creation of electrons at the limit between the bulk and the sheaths. Some electrons are lost by dissociative recombination but overall, in the sheath region, the production largely dominates the loss except at the surface of the walls.

In the bulk, electrons are lost by dissociative recombination. The chemical and stepwise ionization which represent respectively 60% and 40% of the electron creation in the bulk compensate exactly this loss, and there is no net production or destruction of electrons in this region when the stationary state is reached as seen on figure 5.18 (a). This is also true for the electron source over the entire gap so the production of electrons in the sheaths is exactly compensated by the flux to the walls in the steady state.

The total electron source term for electrons when the stationary state is reached is

	Reaction	Electron	Ar^+	Ar_2^+	Ar^*
R1	$e + Ar \rightarrow 2e + Ar^+$	1.24	1.78		
R2	$e + Ar \rightarrow e + Ar^*$				92.48
R3	$e + Ar^* \rightarrow 2e + Ar^+$	55.18	57.06		-5.04
R4	$2Ar^* \rightarrow e + Ar^+ + Ar$	40.38	41.16		-7.28
R5	$Ar^+ + 2Ar \rightarrow Ar_2^+ + Ar$		-99.98	100	
R6	$e + Ar_2^+ \rightarrow Ar^* + Ar$	-82.40		-84.86	7.52
R7	$Ar^* \rightarrow Ar + h\nu$				-87.64
	Loss at the walls	-17.60	-0.02	-15.14	-0.04
	Secondary emission	3.20			

Table 5.1: Relative contributions to creation and destruction of particles [%]

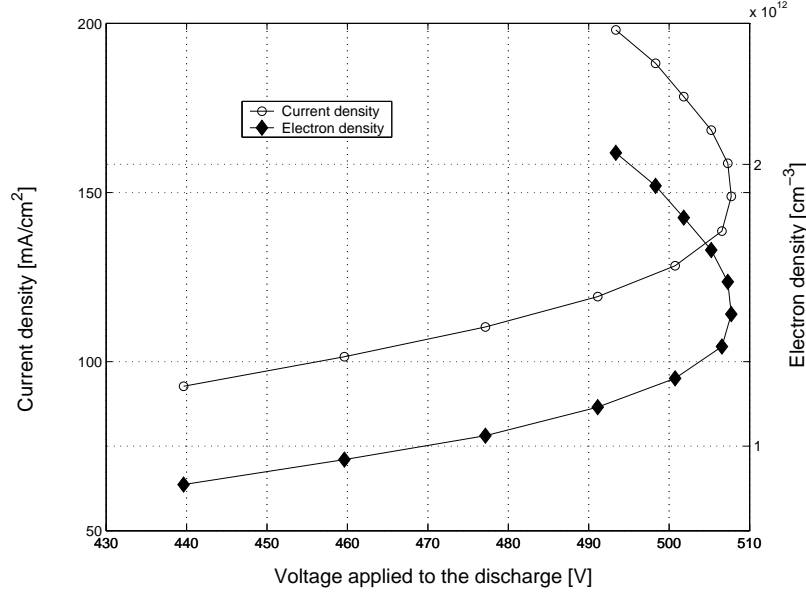


Figure 5.19: I-V characteristic and electron density

shown in figure 5.18 (a) and (b). The source term is zero in the bulk, positive in the sheaths and negative at the walls. The large production of electrons in the sheaths is compensated by the loss to the walls which is responsible for most of the conduction current as seen in figure 5.16. Figure 5.18 (b) shows that electrons are created when the discharge voltage rises and lost as soon as it decreases. The space integral of the source term in figure 5.18 (a) and the time integral in 5.18 (b) are both zero.

For other reactions and other particles the contributions are listed in table 5.1. The values are space-time averaged. Negative numbers represent loss of particles. For each particle the sum of negative numbers is 100% and as well for positive numbers.

5.6 Effects of the applied voltage

The influence of the discharge current on the plasma parameters is studied for values up to 180 mA/cm^2 . The I-V characteristic of figure 5.19 shows that the discharge can operate in two different regimes. The peak value of the voltage applied on the left electrode is represented on the x-axis. This characteristic is obtained by increasing the RF voltage applied to the entire discharge circuit composed of the serial resistor and serial dielectric layer described in section 4.4.

In the first part of the I-V characteristic, for values of the current density lower than 120 mA/cm^2 , the current increases linearly with a rising voltage as in classical RF discharges (Kunhardt, 2000; Park et al., 2000). The conductivity of the plasma is

positive and fairly constant. This behaviour is typical of a normal Radio Frequency α mode (Raizer et al., 1995).

When the current density becomes larger than 120 mA/cm^2 the conductivity of the discharge increases drastically. The maximum voltage of 507 V is reached in this transition region. For values of the current density above 150 mA/cm^2 the conductivity of the plasma is negative, the discharge voltage decreases with increasing current. This behaviour corresponds to the abnormal γ mode of the discharge. There are no simulation results for current densities above 180 mA/cm^2 as the validity of the fluid model is debatable in those conditions.

For certain values of the discharge voltage the two different plasma regimes are possible. For instance, at 500 V the plasma can exist with an electron density of $1.2 \times 10^{12} \text{ cm}^{-3}$ and a current density of 128 mA/cm^2 or with a higher electron density of $1.85 \times 10^{12} \text{ cm}^{-3}$ and current density of 180 mA/cm^2 .

The electron density on figure 5.19 follows a curve similar to the current density. It is proportional to the voltage for values below $1.2 \times 10^{12} \text{ cm}^{-3}$ and rapidly increases for higher values in the transition region. In the abnormal region of negative conductivity the electron density increases as the voltage decreases.

The transition from the α mode to the γ mode has been reported by Levitskii (1957) and analysed with fluid models by Belenguer (1990) for low pressure conditions and for higher pressure in helium by Shi and Kong (2004). It is due to the breakdown of the sheath region similar to a DC breakdown. As the ion density rises in the sheaths, the sheath voltage due to the excess of positive space charge rises as well and eventually reaches the breakdown threshold. When the particles which contribute to the electron production are in sufficiently high density, the plasma can be sustained with a lower voltage, thus the discharge voltage decreases with rising particle density.

The mechanisms of electron production are different for each mode as shown in figure 5.20 (a) for the α mode and (b) for the γ mode. In the α mode electrons are created by the oscillating electric field in the sheaths (approximately 0.2 mm wide) and the production is almost constant over a whole RF cycle. In the γ mode the creation is much more important (by one order of magnitude) and occurs mainly at the instantaneous cathode as in a classical DC discharge. The shrink of the sheaths ($\simeq 0.1 \text{ mm}$) results in a pressure-distance product of 7.6 Torr.cm and a sheath voltage of 150 V (electric field of 61 Td) which is sufficient to ignite a breakdown. As in classical DC breakdown, the secondary emission coefficient γ plays an important role in the RF sheath breakdown and is actually the reason for the abnormal mode naming. In the γ mode the electron creation rate at the walls is $2.1 \times 10^{19} \text{ cm}^{-3}/\text{s}$ whereas in the α mode it is only $3 \times 10^{18} \text{ cm}^{-3}/\text{s}$.

The spatial distribution of the time averaged plasma potential and electron density are represented for different values of the current density in figure 5.21 (a) and (b) respectively. The plasma potential in the middle of the gap is around 150 V for a current density of 100 mA/cm^2 and it increases linearly with the discharge voltage for current densities below 140 mA/cm^2 . For higher values of the current density, the sheath region shrinks and the averaged plasma potential decreases (because the discharge voltage

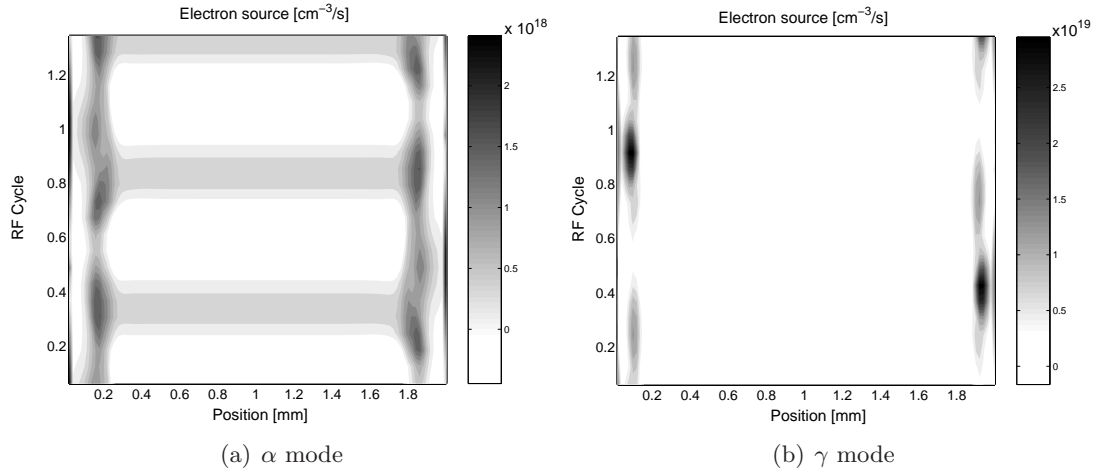


Figure 5.20: Electron source in the alpha mode (a) for a current density of 120 mA/cm^2 and in the γ mode (b) for a current density of 180 mA/cm^2

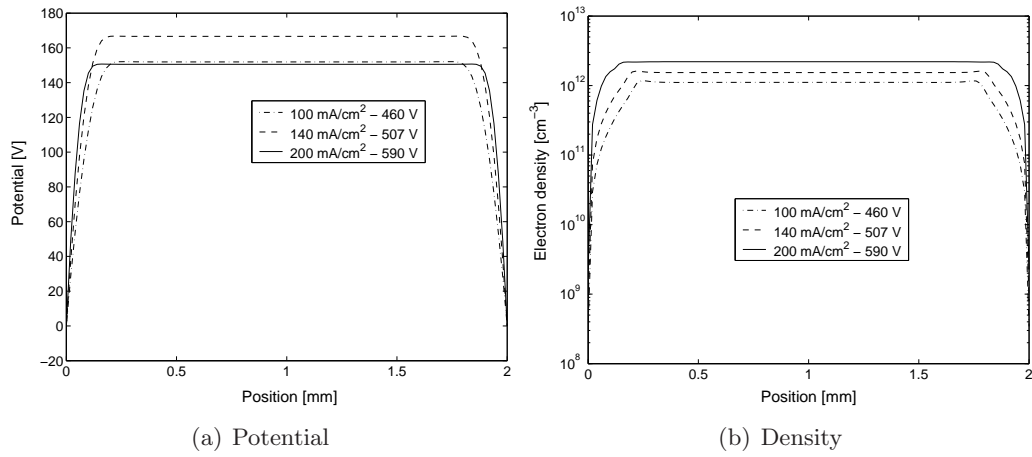


Figure 5.21: Density and potential profiles for different regions of the I-V characteristic

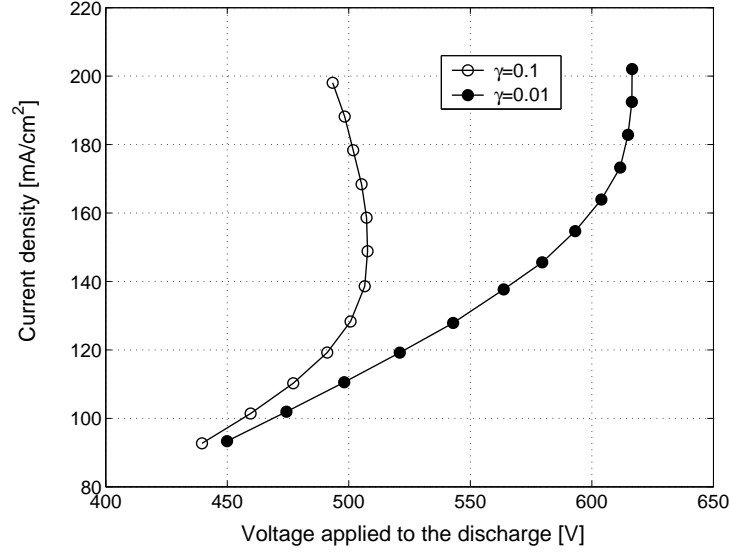


Figure 5.22: I-V characteristic for different value of the secondary emission coefficient

decreases). The shrink of the sheath results in an increase of the electric field in this region. In figure 5.21 (b) the electron density profiles also exhibit the sheath contraction when the current and the electron density rise.

The influence of the secondary emission coefficient on the I-V characteristic is shown in figure 5.22. Its value strongly affects the transition between the two modes. With a low secondary emission ($\gamma = 0.01$), the α mode can be sustained for higher current densities. At 150 mA/cm^2 the discharge is still in an α mode when the secondary emission coefficient is 0.01 but for a higher secondary emission coefficient of 0.1 the transition to the γ mode already starts. With a greater secondary emission coefficient, the transition $\alpha \rightarrow \gamma$ with sheath contractions occurs for lower values of the current density.

For the same current density of 200 mA/cm^2 the electron density profiles obtained with $\gamma = 0.1$ and $\gamma = 0.01$ are represented in figure 5.23. On each profile the electron density in the bulk of the plasma is approximately $2 \times 10^{12} \text{ cm}^{-3}$ but the sheaths size is smaller with a larger secondary emission coefficient.

The glow mode observed experimentally and presented in the section 2.2 is the normal α mode of the discharge. The measured current densities for the glow mode is around 100 mA/cm^2 with an electron density of $5 \times 10^{11} \text{ cm}^{-3}$ which corresponds to the simulation results of the α mode. The total current measured experimentally for the filamentary mode is similar to the glow mode current (identical peak value, curve shape and phase shift with the voltage) but filaments cover a much smaller area of the

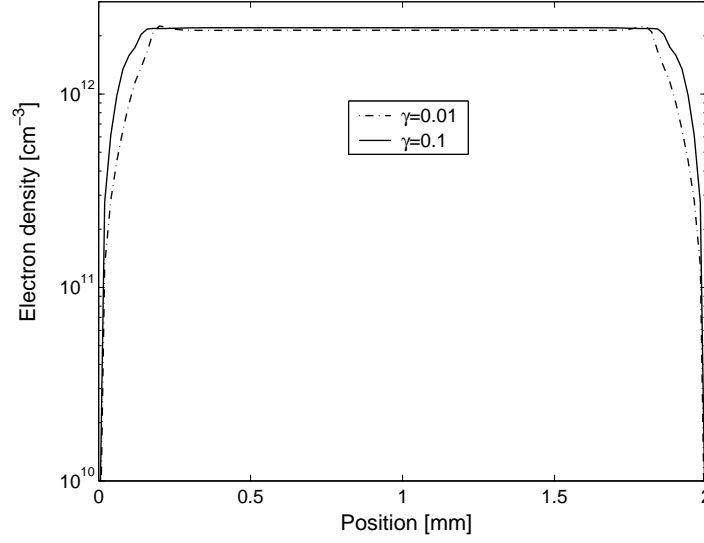


Figure 5.23: Electron density in the γ mode for two values of the secondary emission coefficient. Current density = 200 mA/cm^2

electrode surface (see section 3.2.1). Hence, the current density in filaments is estimated to be around 20 A/cm^2 and the electron density is measured from Stark broadening to be approximately 10^{15} cm^{-3} . These values are not found with the fluid model which aim is not to simulate the filamentary mode. However, this transition from the α mode to the γ mode observed in simulations is possibly responsible for the ignition of the filamentary discharge.

5.6.1 Conclusion

The I-V characteristic of the γ mode with negative conductivity corresponds to an unstable state of the circuit composed by the generator and the discharge. From the γ mode, the total electric circuit of the experimental set-up has a tendency to evolve to another stable state which can be found in the filamentary mode. Even though the fluid model does not account for the complex thermal effects occurring in the gas, the γ mode observed in simulation for high currents is certainly strongly involved in the glow \rightarrow filament transition witnessed experimentally.

Chapter 6

Conclusion

The properties of an atmospheric pressure capacitively coupled RF discharge in argon are investigated both experimentally and with a unidimensional fluid model. Only a limited number of quantities are directly measurable experimentally whereas most of the plasma parameters are accessible with the model. Hence numerical simulations provide an extended comprehension of the discharge properties. However, the numerical model is based on simplistic assumptions which need to be corroborated by experimental measurements. Thus the two approaches are complementary and together they participate to the understanding of the discharge physics.

The diagnostic of atmospheric pressure plasma is usually challenging given the small dimensions of the system and the high value of the electric current. Optical access through the transparent bottom electrode greatly facilitates the spectroscopic diagnostic and the observation of the discharge. The interpretation of optical measurements relies on the assumptions of a partial local Saha equilibrium and on optical thinness for several argon lines. These two hypotheses have been justified and the electron temperature and density were measured in various plasma conditions.

The discharge can operate in two different modes, a stable homogeneous glow or a multitude of filaments forming various patterns on the electrode surface. It was found possible to select the plasma mode by pulsing the RF voltage applied to the powered electrode. By choosing the appropriate pulse width and period controlling the RF generator each mode can be isolated for as long as desired. This is very valuable for the separate analysis of each mode and for the applications to surface treatment. It also suggests that the dielectric temperature and the gas temperature play an important role in the glow to filament transition.

Adding hydrogen in the discharge allows the Stark broadening of a hydrogen line to be measured in order to estimate the electron density. The Electron temperature is deduced from the ratios between neutral and ionized argon lines. In the glow mode the electron density is measured to be approximately $5 \times 10^{11} \text{ cm}^{-3}$ with an electron

temperature around 1.5 eV. The electron density in the filamentary mode is found to be much higher, approximately 10^{15} cm^{-3} with an electron temperature of 1.7 eV.

The unidimensional fluid model with an energy equation for the electrons was written to gain insight into the glow discharge phenomena. It is based on the classical resolution of the fluid equations semi-implicitly coupled to Poisson's equation. Adaptations accounting for the external circuit were included as boundary conditions. The simulation of the spatio-temporal evolution of the plasma and of the argon kinetics allow a better interpretation and apprehension of the discharge physics.

The simulation results are supported by the experimental measurements made on the glow mode. The electron density, the current and the potential are in satisfying agreement with measurements. In addition, the model shows the importance of metastable atoms in the electron production and indicates that the population of molecular ions largely dominates atomic ions population. The I-V characteristic obtained with the model also suggests that the creation of filaments could be triggered by an α to γ mode transition often encountered in RF discharges.

The originality of this experimental set-up is undoubtedly due to the top shower-head electrode through which gas is provided to the discharge. It feeds the electrode gap with a radial centrifuge gas flow without the need of a closed vessel around the discharge. This is very practical for "on-line" surface processes since the plasma can keep running while different samples are treated successively. Only the controlled pulsed glow mode is suitable at atmospheric pressure in argon as localized hot filaments could damage the polymer samples in the continuous RF discharge.

Efficient and fast surface treatment of polyethylene terephthalate films is achieved with the glow mode plasma. Contact angle measurements and SEM microscopy show that the wettability increase obtained with a glow mode is important and lasting. This type of plasma source is very interesting for the textile industry or for polymer functionalisation purposes. These promising results can be put into perspective if we consider the large range of parameters which can be tuned in order to optimize the treatment. The mechanisms behind this improvement are still not well understood but further insight could certainly be gained from X-ray photoelectron spectroscopy or atomic force microscopy. The use of different gas mixtures combined with different polymers should be tested to improve the surface treatment efficiency.

In the future the influence of the gas composition on the glow to filament transition should be studied for continuous RF and pulsed RF discharges. The versatility of the model allows CCP discharges with complex gas mixtures to be simulated so that it can be used in conjunction with various gases experiments. The formation and the conditions of existence of plasma "fingers" should also be further investigated in different gases.

The first evolution to be implemented into the fluid model is the description of thermal phenomena with pulsed and continuous RF signals. This would certainly improve the consistency between simulations and experimental measurements and more systematic comparison would be possible. Finally, the model could be extended in two dimensions in order to further investigate the formation of filaments in the radial axis.

Appendix A

Boltzmann equation

Let us demonstrate the Boltzmann equation for one type of particles moving in a uni-dimensional space. First it is established for a constant number of the particles. If we consider the phase space of a one dimension system as shown on figure [A.1](#), the conservation of particle between t and $t + dt$ leads to:

$$f(x', v', t') dx' dv' = f(x, v, t) dx dv$$

Where f is distribution function of the particle density.

$$x' = x + v dt \tag{A.1}$$

The variation of v during dt is the acceleration of the particles due to the external force applied on them. Here we only consider the force created by an electric field which does not depend on the particle velocity.¹ If we note q the charge and m the particle mass, then $a = qE/m$ and:

$$v' = v + a dt = v + \frac{qE}{m} dt \tag{A.2}$$

The relation between $dx' dv'$ and $dx dv$ is given by $|J|$: the determinant of the Jacobian matrix corresponding to this translation in phase space.

$$dx' dv' = |J| dx dv$$

$$J = \begin{pmatrix} \frac{\partial x'}{\partial x} & \frac{\partial x'}{\partial v} \\ \frac{\partial v'}{\partial x} & \frac{\partial v'}{\partial v} \end{pmatrix}$$

v and x are independent variables so $\frac{\partial v}{\partial x} = 0$ and from [A.1](#):

$$\frac{\partial x'}{\partial x} = \frac{\partial x}{\partial x} + \frac{\partial v}{\partial x} dt = 1$$

¹ The case of a magnetic force is discussed in [Bittencourt 1986](#).

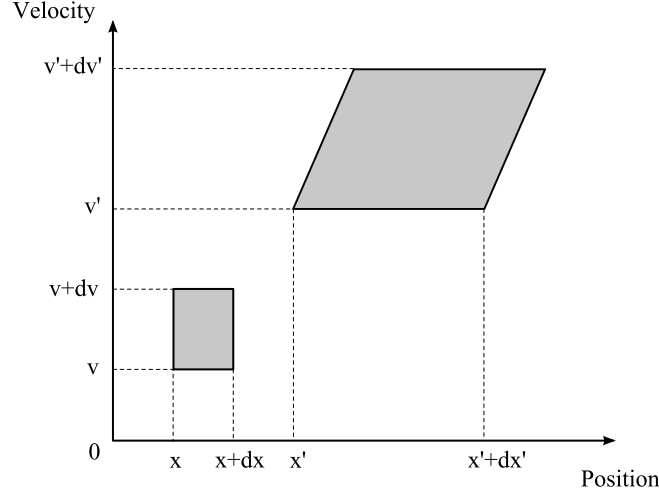


Figure A.1: Phase space

From A.1 and $\frac{\partial x}{\partial v} = 0$:

$$\frac{\partial x'}{\partial v} = dt$$

From A.2 and $\frac{\partial v}{\partial x} = 0$:

$$\frac{\partial v'}{\partial x} = \frac{q}{m} \frac{\partial E}{\partial x} dt$$

From A.2 and the fact that the acceleration is independent of the velocity:

$$\frac{\partial v'}{\partial v} = 1$$

Finally

$$|J| = \begin{vmatrix} 1 & dt \\ \frac{q}{m} \frac{\partial E}{\partial x} dt & 1 \end{vmatrix} = 1 - \frac{q}{m} \frac{\partial E}{\partial x} dt^2$$

Assuming that dt is sufficiently short we can neglect dt^2 and then $|J| = 1$ which leads to:

$$f(x, v, t) = f(x + v \, dt, v + a \, dt, t + dt) \quad (\text{A.3})$$

Using the classical first order development $g(u + du) \simeq g(u) + du \frac{\partial g}{\partial u}(u)$ we can write:

$$f(x + v \, dt, v + a \, dt, t + dt) \simeq f(x, v, t) + dt \left(v \frac{\partial f}{\partial x} + a(x, t) \frac{\partial f}{\partial v} + \frac{\partial f}{\partial t} \right) \quad (\text{A.4})$$

Then from equations A.3 and A.4 we obtain the Vlasov equation:

$$\frac{\partial f}{\partial t}(x, v, t) + v \frac{\partial f}{\partial x}(x, v, t) + a(x, t) \frac{\partial f}{\partial v}(x, v, t) = 0 \quad (\text{A.5})$$

If punctual and instantaneous collisions are taken into account the right hand side term of Vlasov equation A.5 is replaced by:

$$\left\{ \frac{\delta f}{\delta t} \right\}_{col}$$

This term expresses the total source of particles resulting from gain and loss in collisions. The complete Boltzmann equation for particles of a gas in an external electric field is:

$$\frac{\partial f}{\partial t} + v \frac{\partial f}{\partial x} + \frac{qE}{m} \frac{\partial f}{\partial v} = \left\{ \frac{\delta f}{\delta t} \right\}_{col} \quad (\text{A.6})$$

Appendix B

Exponential Scheme

The coefficients of the exponential scheme are found by considering the expression of the flux as a first order differential equation to be solved for the density n . The flux Γ and the drift velocity v_d are taken as being constant over the entire cell of width Δx .

$$\Gamma = v_d n - D \frac{\partial n}{\partial x} \quad (\text{B.1})$$

Let us call:

$$z = \frac{v_d \Delta x}{D}$$

Equation B.1 can be written:

$$\frac{\partial n}{\partial x} - \frac{z}{\Delta x} n = -\frac{\Gamma}{D} \quad (\text{B.2})$$

The solution of this classical differential equation is:

$$n = \beta \exp\left(\frac{zx}{\Delta x}\right) + \frac{\Gamma}{v_d}$$

where β is a constant determined by the boundary conditions at the edges of the cell. Using this expression for $n_i = n(x)$ and for $n_{i+1} = n(x + \Delta x)$ gives the formula for the flux (Γ_i constant over the cell):

$$\Gamma_i = \frac{v_d e^z}{1 - e^z} n_i + \frac{v_d}{1 - e^z} n_{i+1}$$

and the exponential scheme coefficients in the expression $\Gamma_i = a_i n_i + b_i n_{i+1}$ of section 4.3.1 are:

$$a_i = \frac{v_d}{1 - \exp\left(\frac{v_d \Delta x}{D}\right)} - v_d$$

$$b_i = \frac{v_d}{1 - \exp\left(\frac{v_d \Delta x}{D}\right)}$$

Bibliography

- Balcon, N., A. Aanesland, and R. Boswell (2007). Pulsed RF discharges, glow and filamentary mode at atmospheric pressure in argon. *Plasma Sources Science and Technology* 16, 217–225. 55
- Becker, K., U. Kogelschatz, K. Schoenbach, and R. Barker (2004, 11). *Non-Equilibrium Air Plasmas at Atmospheric Pressure (Series in Plasma Physics) (Plasma Physics)*. Taylor & Francis. 53, 54
- Belenguer, P. (1990). Transition between different regimes of rf glow discharges. *Physical Review A* 41(8), 4447. 111
- Bittencourt, J. A. (1986, 6). *Fundamentals of Plasma Physics* (1st ed ed.). Pergamon. 73, 119
- Boeuf, J.-P. (1987). Numerical model of RF glow discharges. *Physical Review A* 36(6), 2782. 20
- Boeuf, J.-P. (1995). Two dimensional model of a capacitively coupled rf discharge and comparisons with experiments in the gaseous electronics conference reference reactor. *Physical Review E* 51(2), 1376. 71, 76
- Boeuf, J.-P. (2003). Plasma display panels: physics, recent developments and key issues. *Journal of Physics D: Applied Physics* 36, R53. 18
- Boeuf, J. P., Y. Lagmich, T. Unfer, T. Callegari, and L. C. Pitchford (2007). Electrohydrodynamic force in dielectric barrier discharge plasma actuators. *Journal of Physics D: Applied Physics* 40, 652–662. 17
- Bowick, C. (1997, 3). *RF Circuit Design*. Newnes. 25
- Caillard, A., C. Charles, R. Boswell, and P. Brault (2007). Integrated plasma synthesis of efficient catalytic nanostructures for fuel cell electrodes. *Nanotechnology* 18(305603), 305603. 68
- Carman, R. J., I. S. Falconer, and R. P. Mildren (2005). Dynamics of a homogeneous dielectric barrier discharge in xenon excited by short-voltage pulses. *IEEE Transactions on Plasma Science* 33(2), 3813. 25

- Chirokov, A. (2005). Atmospheric pressure plasma of dielectric barrier discharges. *Pure Applied Chemistry* 77(2), 487. 19
- Dong, L., J. Ran, and Z. Mao (2005). Direct measurement of electron density in microdischarge at atmospheric pressure by stark broadening. *Applied Physics Letters* 86, 161501. 53, 55
- Ellis, H., R. Pai, E. McDaniel, E. Mason, and L. Viehland (1976). *Transport properties of gaseous ions over a wide energy range*, Volume 17. Academic Press, Inc. 92
- Ferreira, C., J. Loureiro, and A. Ricard (1985). Populations in the metastable and the resonance levels of argon and stepwise ionization effects in a low-pressure argon positive column. *Journal of Applied Physics* 57, 82. 92, 93
- Fridman, A. (2005). Non-thermal atmospheric pressure discharges. *Journal of Physics D: Applied Physics* 38, R1–R24. 19
- Fridman, A. A. and L. A. Kennedy (2004, 4). *Plasma Physics and Engineering* (1 ed.). CRC. 33
- Gigososy, M. A. and V. Cardenoso (1996). New plasma diagnosis tables of hydrogen stark broadening including ion dynamics. *Journal of Physics B: Atomic, Molecular and Optical Physics* 29, 4795–4838. 54
- Griem, H. R. (1997). *Principles of plasma spectroscopy* (2005 ed.). Cambridge: Cambridge University Press, monographs on plasma physics. 55, 59, 61
- Grigoriev, I. S., E. Z. Meilikhov, and A. A. Radzig (1997). *Handbook of Physical Quantities* (November 25, 1996 ed.). TF-CRC. 32, 92
- Hagelaar, G. (2000). *Modelling of microdischarges for display technology*. Ph. D. thesis, Technische Universiteit Eindhoven. 71, 76, 87
- Hagelaar, G., F. de Hoog, and G. Kroesen (2000). Boundary conditions in fluid models of gas discharges. *Physical Review E* 62(1), 1452–1454. 79
- Hagelaar, G. J. M. and L. C. Pitchford (2005). Solving the boltzmann equation to obtain electron transport coefficients and rate coefficients for fluid models. *Plasma Sources Science and Technology* 14, 722–733. <http://www.codiciel.fr/plateforme/plasma/bolsig/bolsig.php>. 72, 93
- Hammond, E. P. (2002). A numerical method to simulate radio-frequency plasma discharges. *Journal of Computational Physics* 176, 402. 71
- Hopfe, V. and D. Sheel (2007). Atmospheric-Pressure PECVD Coating and Plasma Chemical Etching for Continuous Processing. *Plasma Science, IEEE Transactions on* 35(2 Part 1), 204–214. 66

- Karoulina, E. V. and Y. A. Lebedev (1992). Computer simulation of microwave and DC plasmas: comparative characterization of plasmas. *Journal of Physics D: Applied Physics* 25, 401–412. 93
- Kogelschatz, U. (2000). Filamentary and diffuse barrier discharges. *Obero Parkstr.* 8, 5212. 20
- Kogelschatz, U. (2003). Dielectric-barrier discharges : Their history, discharge physics, and industrial applications. *Plasma Chemistry and Plasma Processing* 23(1), 0272–4324. 18
- Kunhardt, E. E. (2000). Generation of large-volume, atmospheric-pressure, nonequilibrium plasmas. *IEEE Transactions on Plasma Science* 28(1), 189. 20, 110
- Lam, S. K., C.-E. Zheng, D. Lo, A. Dem'yanov, and A. P. Napartovich (2000). Kinetics of Ar_2^+ in high-pressure pure argon. *Journal of Physics D: Applied Physics* 33, 242–251. 93
- LeToulouzan, J. (1981). Inversion d'axe d'un plasma cylindrique d'hélium réalisation d'un spectrographe stigmatique à détecteur vidicon. *Journal Optics (Paris)* 12(6), 369–376. 57
- Levitskii, S. (1957). An investigation of the breakdown potential of a high-frequency plasma in the frequency and pressure transition regions. *Zh Tekh Fiz* 27, 970. 111
- Lieberman, M. A. and A. J. Lichtenberg (1994). *Principles of plasma discharges and material processing*. New-York: Wiley-Interscience. 56
- Lymberopoulos, D. (1993). Fluid simulations of glow discharges: Effect of metastable atoms in argon. *Journal of Applied Physics* 73(8), 3668. 100
- Lymberopoulos, D. and D. Economou (1993). Fluid simulations of radio frequency glow discharges: Two-dimensional argon discharge including metastables. *Applied Physics Letters* 63, 2478. 100
- Massines, F., N. Gherardi, N. Naudé, and P. Ségur (2005). Glow and Townsend dielectric barrier discharge in various atmosphere. *Plasma Physics and Controlled Fusion* 47(12B), B577–B588. 20, 52
- Massines, F. and G. Gouda (1998). A comparison of polypropylene-surface treatment by filamentary, homogeneous and glow discharges in helium at atmospheric pressure. *Journal of Physics D: Applied Physics* 31, 3411. 66
- Massines, F., R. Messaoudi, and C. Mayoux (1998). Comparison between air filamentary and helium glow dielectric barrier discharges for the polypropylene surface treatment. *Plasmas and Polymers* 3(1), 43. 66

- Massines, F., A. Rabehi, P. Decomps, R. B. Gadri, P. Ségur, and C. Mayoux (1998). Experimental and theoretical study of a glow discharge at atmospheric pressure controlled by dielectric barrier. *Journal of Applied Physics* 83(6), 2950. 17
- Mildren, R. P. and R. J. Carman (2001). Enhanced performance of a dielectric barrier discharge lamp using short-pulsed excitation. *Journal of Physics D: Applied Physics* 34, 3727. 18, 25
- Min, B., S. Lee, and H. Park (2000). New combination of a three-component gas, neon-argon, for a high efficiency plasma display panel. *The Journal of Vacuum Science and Technology A* 18(2), 349. 93
- Moisan, M. and J. Pelletier (2006). *Physique des plasmas collisionnels - Application aux décharges haute fréquence*. EDP science. 76
- Moon, S. Y. (2006). *Study on Discharge Modes and Characteristics of Large-Area Plasma Produced at Atmospheric Pressure*. Ph. D. thesis, KAIST. 53
- Moon, S. Y., W. Choe, and B. K. Kang (2003). A uniform glow discharge plasma source at atmospheric pressure. *Applied Physics Letters* 84(2), 188. 17, 20, 66
- Moravej, M. (2006). Properties of an atmospheric pressure radio-frequency argon and nitrogen plasma. *Plasma Sources Science and Technology* 15, 204–210. 20
- Moreau, E. (2007). Airflow control by non-thermal plasma actuators. *Journal of Physics D: Applied Physics* 40, 605–636. 17
- Muller, I. (1999). Self-organized filaments in dielectric barrier glow discharges. *IEEE Transactions on Plasma Science* 27(1), 20. 20
- Oda, A., T. Hasegawa, T. Kimura, and Y. Oshikane (2005). One-dimensional fluid modelling of radio frequency and atmospheric-pressure glow discharges in he/o₂ gas mixture. In *XXVIIth ICPIG, Eindhoven, the Netherlands, 18-22 July, 2005*. 20
- Oda, A., T. Kimura, and Y. Oshikane (2006). Numerical analysis of fundamental discharge properties in radio-frequency and atmospheric-pressure glow discharges in argon. In *Asia-Pacific Conference on Plasma Science and Technology*. 58, 100, 103
- Park, J. (2001). Gas breakdown in an atmospheric pressure radio-frequency capacitive plasma source. *Journal of Applied Physics* 89(1), 15. 35
- Park, J., I. Henins, H. W. Herrmann, G. S. Selwyn, and R. F. Hicks (2001). Discharge phenomena of an atmospheric pressure radio-frequency capacitive plasma source. *Journal of Applied Physics* 89(1), 20. 56, 100
- Park, J., I. Henins, H. W. Herrmann, G. S. Selwyn, J. Y. Jeong, R. F. Hicks, D. Shim, and C. S. Chang (2000). An atmospheric pressure plasma source. *Applied Physics Letters* 76(3), 288. 20, 110

- Penache, C., M. Miclea, A. Bruning Demian, O. Hohn, S. Schüssler, T. Jahnke, K. Niemax, and H. Schmidt-Böcking (2002). Characterization of a high-pressure microdischarge using diode laser atomic absorption spectroscopy. *Plasma Sources Science and Technology* 11(4), 476–483. 100
- Penache, M. (2002). *Study of High Pressure Glow Discharges Generated by Micro Structured Electrode (MSE) Arrays*. Ph. D. thesis, s. n. 100
- Raizer, Y. P. (2001, 2). *Gas Discharge Physics* (1st ed. 1991. Corr. 2nd printing ed.). Springer. 18, 77
- Raizer, Y. P., M. N. Shneider, and N. A. Yatsenko (1995, 2). *Radio-Frequency Capacitive Discharges*. CRC. 52, 97, 111
- Ralchenko, Y., F.-C. Jou, D. Kelleher, A. Kramida, A. Musgrove, J. Reader, W. Wiese, and K. Olsen (2007). Nist atomic spectra database (version 3.1.2). *National Institute of Standards and Technology, Gaithersburg, MD*. <http://physics.nist.gov/asd3>. 63
- Roth, J. R., J. Rahel, X. Dai, and D. M. Sherman (2005). The physics and phenomenology of one atmosphere uniform glow discharge plasma (OAUGDP) reactors for surface treatment applications. *Journal of Physics D: Applied Physics* 38, 555–567. 17, 66
- Samuëll, C. (2006). Spatiotemporal pattern formation in the glow mode of an argon dielectric barrier discharge plasma at atmospheric pressure. Technical report, Australian National University, Research School of Physical Sciences and Engineering. 37, 39
- Scharfetter, D. and H. Gummel (1969). Large-signal analysis of a silicon Read diode oscillator. *Electron Devices, IEEE Transactions on* 16(1), 64–77. 82
- Schütze, A. (1998). The atmospheric-pressure plasma jet: A review and comparison to other plasma sources. *IEEE Transactions on Plasma Science* 26(6), 1685. 18, 19
- Shenton, M. and G. Stevens (2001). Surface modification of polymer surfaces: atmospheric plasma versus vacuum plasma treatments. *Journal of Physics D: Applied Physics* 34(18), 2761–2768. 66
- Shi, J., X. Deng, R. Hall, J. Punnett, and M. Kong (2003). Three modes in a radio frequency atmospheric pressure glow discharge. *Journal of Applied Physics* 94, 6303. 52
- Shi, J. and M. Kong (2004). Mechanisms of the α and γ modes in radio-frequency atmospheric glow discharges. *Journal of Applied Physics* 97, 023306. 100, 111
- Shi, J., D. Liu, and M. Kong (2006). Plasma stability control using dielectric barriers in radio-frequency atmospheric pressure glow discharges. *Applied Physics Letters* 89, 081502. 51

- Síra, M., D. Trunec, P. Stahel, V. Bursíková, Z. Navrátil, and J. Bursík (2005). Surface modification of polyethylene and polypropylene in atmospheric pressure glow discharge. *Journal of Physics D: Applied Physics* 38(4), 621–627. 66
- Smith, H. B., C. Charles, and R. W. Boswell (2003). Breakdown behavior in radio-frequency argon discharges. *Physics of Plasmas* 10(3), 875. 20
- Sutherland, O. (2005). *A study of high brightness plasma ion sources*. Ph. D. thesis, Australian National University. 60
- van der Mullen, J., D. Benoy, F. Fey, B. van der Sijde, and J. Vlček (1994). Saha equation for two-temperature plasmas: Theories, experimental evidence, and interpretation. *Physical Review E* 50(5), 3925–3934. 61
- William, H. et al. (1992). *Numerical recipes in C: the art of scientific computing*. Cambridge University Press. 83